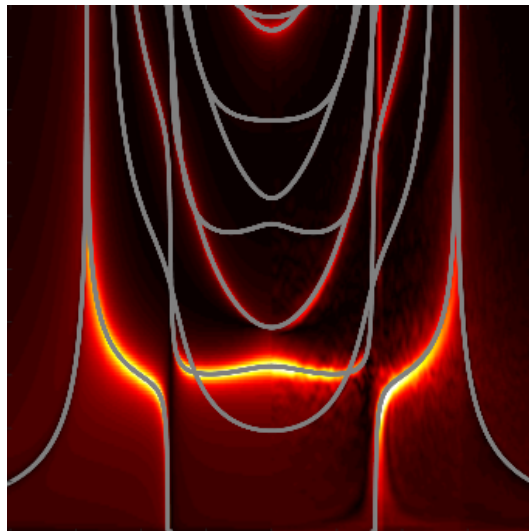


Modelling the Directional Response of Fabry-Pérot Ultrasound Sensors

Danny Raj Ramasawmy



A dissertation submitted in partial fulfillment
of the requirements for the degree of
Doctor of Philosophy
of
University College London.

Department of Medical Physics and Bioengineering
University College London

March 23, 2020

I, Danny Raj Ramasawmy, confirm that the work presented in this thesis is my own. Where information has been derived from other sources, I confirm that this has been indicated in the work.

Abstract

Fabry-Pérot ultrasound sensors offer an alternative to traditional piezoelectric sensors for clinical and metrological applications, for example, measuring high-intensity focused-ultrasound (HIFU) fields. In this thesis, a model of the frequency-dependent directional response was developed based on the partial-wave method, treating the sensor as a multi-layered elastic structure.

An open-source MATLAB toolbox called `ElasticMatrix` was developed to model acoustic and elastic-wave propagation in multi-layered structures with anisotropic material properties. The toolbox uses an object-oriented framework, giving it a simple scripting interface and allowing it to be expanded easily. The toolbox is capable of calculating and plotting reflection and transmission coefficients, slowness profiles, dispersion curves and displacement and stress fields. An additional MATLAB class is included to model the frequency-dependent directional response of Fabry-Pérot ultrasound sensors.

The model was validated, tested and compared with directional response measurements made on two glass-etalon sensors: an air-backed cover-slip sensor with well-known acoustic properties, and an all-hard-dielectric sensor. Features of the directional response were investigated and attributed to the critical angles of the substrate backing, and Lamb- and Rayleigh-modes propagating in the sensor.

The directional response of two sensors with Parylene C (a commonly used soft-polymer) were also investigated: a sensor with a Parylene C spacer, and a glass-etalon sensor with a thick Parylene C coating. X-ray diffraction and transmission electron microscope measurements indicated Parylene has a crystal structure and impedance measurements indicated that Parylene is acoustically anisotropic.

Using the measured impedance values, the modelled and measured directivity had improved agreement compared with isotropic values based on the phase-speeds of guided modes.

The developed modelling tools allow detailed analysis of the physical mechanisms affecting the frequency-dependent directional response of planar Fabry-Pérot sensors. This knowledge can be used to inform future sensor design, to aid with material selection, and for deconvolution of the sensor response from acoustic measurements.

Impact statement

The first key output of this thesis is the development of an open-source MATLAB toolbox called `ElasticMatrix`. This toolbox uses the partial-wave method for modelling elastic-wave propagation for multilayered media. These types of methods have had a significant impact on different areas of acoustics, such as non-destructive evaluation and geophysics. These methods are still relevant today, however, there is no open-source or easily accessible implementation. `ElasticMatrix` fills this gap and is implemented with an object-oriented framework. This makes the toolbox easy to use, develop and expand. It is hoped the research-community will actively contribute to this software and develop it for their own requirements.

Secondly, the work in this thesis has investigated the suitability of these methods for modelling the directional response of Fabry-Pérot ultrasound sensors. The experimental and modelled results had good agreement for sensors of well known material properties and demonstrated the directional response could be significantly affected by elastic waves within the sensor. This has uses for designing and testing different Fabry-Pérot sensors. This may be used to reduce artefacts on image reconstruction when imaging with the sensor, and optimize the design for different use cases. The work has also revealed potential problems with Parylene C as a spacer material for Fabry-Pérot sensors. In particular, it exhibits anisotropic acoustic properties and has problems with self-adhesion and delamination. This is not only useful information for Fabry-Pérot sensors, also for Micro-Electro-Mechanical Systems (MEMS) devices and many other industries that routinely use Parylene.

The work in this thesis has been communicated through conference publica-

tions, journal publications, presentations, poster sessions, and online through the biomedical ultrasound group website. The software developed in this thesis is freely available on github and MATLAB file exchange.

Contents

1	Introduction	17
1.1	Motivation	17
1.2	Spatial Averaging Directional Response Models	19
1.3	Common Hydrophones for Biomedical Ultrasound Applications	22
1.3.1	Piezoelectric Hydrophones	22
1.3.2	Capacitive Micromachined Ultrasonic Transducers	28
1.3.3	Optical Hydrophones	30
1.4	Summary	36
1.5	Thesis Objectives and Structure	36
2	The Fabry-Pérot Sensor	39
2.1	Introduction	39
2.2	Fabrication	40
2.3	Interferometer Transfer Function	41
2.4	Acoustic Phase Sensitivity	43
2.5	Variation of Refractive Index with Pressure	45
2.6	Modelling the Directional Response	49
2.7	Previous Models of the Fabry-Pérot Sensor	50
3	Elastic Waves in Layered Media	52
3.1	Introduction	52
3.2	The Elastic Wave Equation	53
3.2.1	Derivation of the Elastic Wave Equation	53

- 3.2.2 Solutions to the Wave Equation 58
- 3.2.3 Christoffel Equation 58
- 3.3 Partial-Wave and Global Matrix Method 62
 - 3.3.1 Overview 62
 - 3.3.2 Boundary Conditions and Partial-Wave Amplitudes 62
 - 3.3.3 Shear-Horizontal Waves 67
 - 3.3.4 Potential Method 67
 - 3.3.5 Attenuation 68
- 3.4 Dispersion and Modal Solutions 69
 - 3.4.1 Introduction 69
 - 3.4.2 Modal Solutions 71
- 3.5 Summary 72

4 ElasticMatrix: A MATLAB Toolbox for Anisotropic Elastic-Wave

- Propagation in Multilayered Media 73**
- 4.1 Introduction 73
- 4.2 Implementation 75
 - 4.2.1 Field Matrices and Global Matrix 75
 - 4.2.2 Dispersion Curve Algorithm 76
 - 4.2.3 Time Domain Analysis 82
- 4.3 Software Description 83
 - 4.3.1 Overview 83
 - 4.3.2 Documentation 85
 - 4.3.3 Medium 86
 - 4.3.4 Slowness Profiles 87
 - 4.3.5 ElasticMatrix 87
 - 4.3.6 Reflection and Transmission Coefficients 89
 - 4.3.7 Dispersion Curves 90
 - 4.3.8 Displacement and Stress Fields 91
 - 4.3.9 FabryPerotSensor 92
 - 4.3.10 Run-time 94

4.3.11	Summary	94
4.4	Validation	97
4.4.1	Introduction	97
4.4.2	Boundary Conditions	97
4.4.3	Comparison with Potential Method	99
4.4.4	Displacement in Water	99
4.4.5	Fluid-Fluid Interface	100
4.4.6	Fluid-Solid Interface	101
4.4.7	Solid-Solid Interface	103
4.4.8	Three-Layers Normal Incidence	105
4.4.9	Dispersion Curves	106
4.4.10	Mode shapes of Guided Waves	108
4.4.11	Comparison with Previous Models	110
4.5	Summary	112
5	Analysis of the Directivity of Glass Etalon Sensors	113
5.1	Introduction	113
5.2	Transduction Mechanism Review	114
5.3	Measuring the Directional Response	116
5.3.1	Overview	116
5.3.2	Process of Alignment	117
5.3.3	Data Processing	118
5.4	Model Results	119
5.4.1	Validation Air-Backed Glass Cover-slip	119
5.4.2	Hard-Dielectric Sensor	120
5.5	Feature Analysis	125
5.5.1	Overview	125
5.5.2	Critical Angles	125
5.5.3	Guided Wave Features	127
5.5.4	Other Features	131
5.6	Influence of Strain-Optic Coefficients	132

5.6.1	Strain-Optic Coefficients	132
5.6.2	Discussion	135
5.7	Summary	137
6	Soft-Polymer Sensors	138
6.1	Introduction	138
6.2	Evidence for Crystal Structure	141
6.2.1	Deposition of Parylene	141
6.2.2	X-ray Diffraction and Electron Microscopy Measurements .	143
6.3	Determining Material Parameters	147
6.3.1	Physical and Optical Measurement of Thickness	147
6.3.2	Acoustic Impedance Measurement	149
6.4	Directivity with Measured Parameters	151
6.4.1	Parylene Coated Cover-Slip	151
6.4.2	Soft-Polymer Sensor	152
6.4.3	Discussion	153
6.5	Summary	156
7	General Conclusions	157
	Appendices	161
A	Derivation of Beam Profiles	161
A.1	‘Top-hat’ Beam Profile	161
A.2	Gaussian Beam	162
B	Publications, software and awards	164
B.1	Publications	164
B.1.1	Journal	164
B.1.2	Conference	164
B.2	Software	165
B.3	Awards	165

Contents

11

Bibliography

166

List of Figures

1.1	Directional response of a soft-polymer sensor.	19
1.2	Directional response models for a circular piston.	21
1.3	Profiles of the directional response models for a circular piston.	22
1.4	Images of hydrophones.	24
1.5	Frequency response for membrane and needle hydrophones.	26
1.6	Directional response of a needle hydrophone.	26
1.7	Directional response of a membrane hydrophone.	28
1.8	Diamgram of a cMUT.	30
1.9	Frequency response of a cMUT.	30
1.10	Directional response of a cMUT versus PZT element.	31
1.11	Directional response of an Eisenmenger fibre-optic hydrophone.	33
1.12	Frequency response of plano-concave microresonators.	34
1.13	Directional response of a planar Fabry-Pérot ultrasound sensor.	35
1.14	Directional response of a Fabry-Pérot fibre sensor.	35
1.15	Directional response of a plano-concave Fabry-Pérot sensor.	36
2.1	Diagram of a Fabry-Pérot sensor.	40
2.2	Interferometry transfer function of a Fabry-Pérot sensor.	43
2.3	Coordinate system for the sensor.	45
2.4	Diagram of the optical indicatrix.	48
2.5	Directional response of a soft-polymer sensor.	51
3.1	Diagram for partial-wave model.	55
3.2	Labelling for interfaces and field matrices.	64

3.3	Illustrative example of anti-symmetric and symmetric mode shapes.	71
4.1	Example of sweep for dispersion curve starting points.	77
4.2	Sweeping for dispersion curve starting points.	79
4.3	Fine search for points on the dispersion curve.	80
4.4	Interpolation scheme for finding the next point.	81
4.5	Effect of leaky media.	82
4.6	UML class diagram for <code>ElasticMatrix</code>	85
4.7	HTML documentation for <code>ElasticMatrix</code>	86
4.8	Slowness profiles example.	88
4.9	Reflection coefficient example.	90
4.10	Dispersion curve example.	91
4.11	Schoch displacement example.	93
4.12	Guided mode example of time domain analysis.	93
4.13	Fabry-Pérot directivity example.	95
4.14	Run time for <code>ElasticMatrix</code>	95
4.15	Field parameters in an arbitrary multilayer structure.	98
4.16	Displacement scaling of the model in water.	100
4.17	Reflection and transmission between two Fluid half-spaces.	101
4.18	Reflection and transmission between two half-spaces.	104
4.19	Reflection and transmission between two half-spaces.	104
4.20	Reflection and transmission between two solid half-spaces.	106
4.21	Pressure reflection and transmission coefficients for three layers. . .	107
4.22	Dispersion curve comparison.	108
4.23	Dispersion curve comparison.	109
4.24	Displacement fields for guided modes.	110
4.25	Fabry-Pérot frequency response comparison.	111
4.26	Fabry-Pérot directional response comparison.	112
5.1	Diagram of glass etalon sensors.	114
5.2	Experimental setup for measuring directivity.	117

5.3	Photoacoustic pulse used in the directivity experiment.	117
5.4	Alignment of the directional response experiment.	118
5.5	Measured and modelled directional response.	121
5.6	Profiles of the directional response.	122
5.7	Modelled and measured directional response.	123
5.8	Profiles of the directional response.	124
5.9	Critical angle features.	127
5.10	Dispersion curves and modelled and measured directional response.	128
5.11	Displacement of Lamb modes in cover-slip sensor.	129
5.12	Rayleigh wave displacement in all-hard dielectric sensor.	130
5.13	Minima in the directional response.	132
5.14	Profiles of the directional response.	134
5.15	Profiles of the directional response.	135
5.16	The integral of strain components over the spacer thickness.	135
6.1	Diagram of polymer sensor and glass cover-slip sensor.	138
6.2	Directional response of a soft-polymer sensor.	140
6.3	Profiles of the directional response of a soft-polymer sensor.	141
6.4	Directional response of a Parylene coated cover-slip sensor.	142
6.5	Profiles of a Parylene coated cover-slip sensor.	143
6.6	X-ray diffraction results.	144
6.7	Parylene crystals.	145
6.8	Transmission electron microscope images of Parylene.	145
6.9	Finding the free-spectral range from the ITF.	147
6.10	Profilometer measurement of a Parylene spacer.	149
6.11	Impedance measurement of Parylene C.	150
6.12	Directional response of a Parylene coated cover-slip sensor.	153
6.13	Profiles of a Parylene coated cover-slip sensor.	153
6.14	Directional response of a Parylene coated cover-slip sensor.	154
6.15	Directional response of a soft-polymer sensor.	154
6.16	Profiles of the directional response of a soft-polymer sensor.	155

6.17 Directional response of a soft-polymer sensor. 155

List of Tables

- 1.1 Table of noise-equivalent pressure values. 27

- 5.1 Table of material properties. 116
- 5.2 Table of strain-optic coefficients. 116
- 5.3 Effective dielectric mirror parameters 123

- 6.1 Table of Parylene C properties. 139
- 6.2 Table of Parylene C thickness measurements. 148
- 6.3 Table of Parylene C impedance measurements. 151

Chapter 1

Introduction

1.1 Motivation

The versatility of ultrasound has made it essential in many different clinical and industrial applications, including: medical imaging, non-destructive evaluation (NDE), microscopy and metrology [1, 2]. The detection of ultrasound for these applications uses a variety of different technologies. To give a few examples, a piezoelectric phased array transducer is often used in medical imaging and NDE, a Fabry-Pérot sensor or capacitive micromachined ultrasound transducer (cMUT) array may be used to detect signals in photoacoustic imaging, and Michelson interferometry may be used to measure acoustic fields in metrology.

For an accurate measurement of the acoustic field there are a number of sensor characteristics which must be considered. For example, the noise equivalent pressure (NEP), the frequency-response and bandwidth, the linearity with respect to pressure or stress, the perturbation effect of the sensor in the measurement field, and the stability over short and long time scales.

Another important characteristic is the frequency-dependent directional response. This is the amplitude and phase sensitivity of the sensor from planar acoustic waves as a function of incidence angle and frequency [3]. The directionality (and other characteristics) of the sensor are application dependent. In some instances it is desirable for the ultrasound detector to have an omnidirectional response. For example, when making measurements of a highly focused acoustic field, and in photoa-

oustic tomography and synthetic aperture pulse-echo imaging [4, 5]. Conversely, there are other instances where having a highly directional response is desirable, for example, to minimize the detection of edge waves or waves reflected off scanning tank walls when measuring sound speed and absorption [6, 3]. In all of these cases, choosing a sensor with an unsuitable directional response may cause artefacts in the measurement, reduce the signal-to-noise ratio, or fail to detect features in the measured field.

In general, there are two mechanisms which contribute to the frequency-dependent directional response. The first, which is common to all sensors, is the influence of spatial averaging. The significance of this effect is determined by the size of the detection area (active element) compared with the wavelength of the ultrasonic wave. For a fixed frequency, a smaller sensor area tends toward an omnidirectional response and a larger area has a more directional response. The second mechanism contributing to the directional response occurs when the incident ultrasound wave reaches the detector. Here, the ultrasound wave may be scattered and have complex interactions with the sensor which depend on the geometry, construction materials, and transduction mechanism. These interactions vary depending on both the angle and frequency of the incident ultrasound wave.

Developing and understanding accurate models of the directional response for different sensors is important for a number of reasons. Firstly, models can be used as a tool for analysis and design to improve the directional characteristics of the sensor [7]. Additionally, a model may be used to deconvolve the directional response from measurements in medical and imaging applications. This can improve the accuracy of the measurements and reduce imaging artefacts [5, 8, 9]. Finally, understanding the sensitivity and directional response of the sensor allows users to choose the most appropriate detector for their intended application.

The focus of this thesis is on modelling the directional response of planar Fabry-Pérot ultrasound sensors. The directional response of a planar soft-polymer sensor has previously been modelled by Cox [7] and was initially found to have good agreement with measurements. However, the measured data was dominated

by the effects of spatial averaging which precluded features occurring from guided modes. Subsequent measurements of similarly constructed sensors, with small effective elements, had poor agreement between the measured and modelled data, an example is given in Figure 1.1. Additionally, the model by Cox was restricted to three isotropic layers and neglected the strain-optic effect.

An initial motivation of this thesis was to understand why this model had poor agreement and to fully explain the complex features of the directional response for planar Fabry-Pérot sensors. This is discussed further at the end of this chapter in Section 1.5. The remainder of this chapter outlines the characteristics of common hydrophones used for detecting ultrasound. Here, there is a particular focus on hydrophones for biomedical applications and the directional response of these sensors.

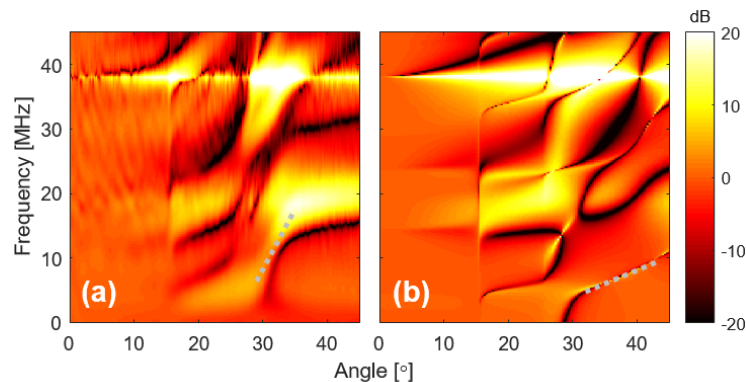


Figure 1.1: (a) Measured directional response of a soft-polymer sensor. (b) Modelled directional response of a soft-polymer sensor using an equivalent model to Cox [7].

1.2 Spatial Averaging Directional Response Models

In this section, three simple models of the directional response are introduced. The directional response is often thought of as the transmitted diffraction pattern caused by an equivalent source which corresponds to the sensitive element of the hydrophone [3]. The principle of reciprocity is used to equate the transmit and receive diffraction patterns [3]. The hydrophones can be modelled by averaging the pressure on the surface of the hydrophone over the area of the sensitive element. This leads to the first model, which assumes a circular planar piston in a rigid pla-

nar baffle, where the directional response D for a single frequency plane wave is given by [10, 3]

$$D(k, \theta) = \frac{2J_1(ka \sin \theta)}{ka \sin \theta}. \quad (1.1)$$

Here, J_1 is a Bessel function of the first kind, θ is the angle of incidence, k is the bulk wavenumber of the acoustic wave, and a is the radius of the active element of the hydrophone. The value of a can deviate from the nominal active element size and is often fitted by comparing measurements of the directional response with the model. The fitted value of a is called the effective element radius. The effective element area is important to consider when choosing an appropriate hydrophone for measurements or if using a model to deconvolve measurement data.

A modification of the first model is a circular piston in a soft baffle, where the directivity is given by [11]

$$D(k, \theta) = \frac{2J_1(ka \sin \theta)}{ka \sin \theta} \cos \theta. \quad (1.2)$$

Finally, the third model assumes an unbaffled circular piston, where the directivity is given by [12]

$$D(k, \theta) = \frac{2J_1(ka \sin \theta)}{ka \sin \theta} \left(\frac{1 + \cos \theta}{2} \right). \quad (1.3)$$

The directional responses of these models are omnidirectional at low ka values and become increasingly directional as ka increases. In general, the directional response is complex, Figure 1.2 and Figure 1.3 show the magnitude of the normalised directional response. The phase is not plotted, however, there is a π -phase change at every zero crossing in the directional response. All the models give similar results for high ka values ($ka > 4$) but vary at ka values less than this. This can be understood by considering the wavelength of the acoustic wave in comparison to the detection area. If the value of ka is large, then there are multiple wavelengths averaged over the detection area and the influence of the rigid/soft/unbaffled boundary conditions becomes less significant. Whereas, at low ka values there may be only a few or fractions of a wavelength averaged over the detection area. Here, the boundary conditions will have a greater effect on the measurement.

The circular piston in a rigid baffle model is the standard for estimating the hydrophone effective element size from measurements, however, there are many cases where this model does not fit measurement data [3, 13, 14, 15]. The discrepancies may come from the fact that these models incorrectly model the true physical mechanisms and boundary conditions of the sensor [16]. For this reason other models have been proposed. For example, Krucker proposed a model for fibre-optic hydrophones which takes into account diffraction effects from the fibre-tip [17]. For membrane hydrophones, Bacon proposed a model which accounts for the coupled effect of elastic waves on piezoelectric coefficients from Lamb waves propagating in the membrane [18]. These models have not been plotted here, but go some way to explain the discrepancies between the three simple models plotted below and the true directional response of different hydrophones. It is worth noting that the models have similar responses at small angles of incidence ($\pm 15^\circ$). This gives reasonable results when estimating the effective element radius with the standard diffraction model for the central portion of the measured directional.

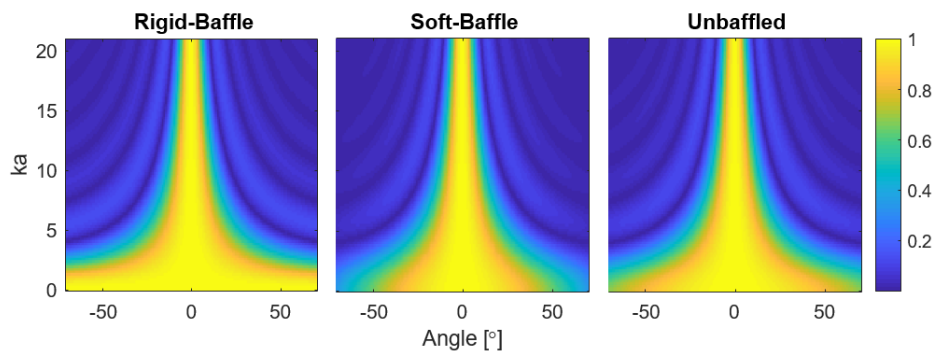


Figure 1.2: Normalised frequency-dependent directional response for the circular piston in a rigid baffle (RB), the circular piston in a soft-baffle (SB) and the unbaffled piston (UB) models.

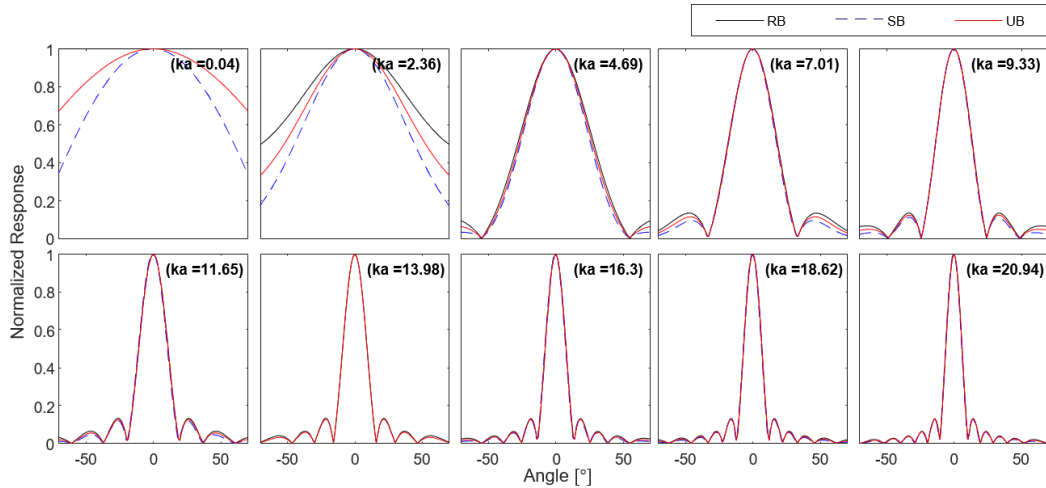


Figure 1.3: Profiles of the directional response for the circular piston in a rigid baffle (RB), the circular piston in a soft-baffle (SB) and the unbaffled piston (UB) models. These profiles are taken from Figure 1.2 at different values of ka . At values greater than $ka > 4$ the profiles have significant overlap.

1.3 Common Hydrophones for Biomedical Ultrasound Applications

1.3.1 Piezoelectric Hydrophones

1.3.1.1 The Piezoelectric Effect

Piezoelectric hydrophones use piezoelectric elements to detect ultrasound (see Figure 1.4). Piezoelectric materials produce a voltage when under a mechanical stress and the magnitude of the voltage and stress are proportional. Additionally, the reciprocal is true, when a voltage is applied to the piezoelectric material a mechanical strain is induced. These properties allow piezoelectric materials to be exploited to both transmit and receive a signal in an ultrasound transducer.

A piezoelectric ultrasound receiver may be a single element or an array of multiple elements depending on the intended use and application. The two most common piezoelectric materials used are the ceramic Lead Zirconate Titanate (PZT) and the polymer Polyvinylidene Difluoride (PVDF). Materials, such as PZT are poly-crystalline and are made from multiple crystals oriented randomly. Each individual crystal may exhibit piezoelectric properties, however, PZT does not exhibit strong piezoelectric properties in this form [19]. A process called poling allows the

crystal's dipole moment to be better aligned so the ceramic presents with piezoelectric properties. There are a few steps in the poling process. Firstly, the material is heated beyond its Curie temperature, ($> 200^{\circ}\text{C}$ for PZT, $> 60^{\circ}\text{C}$ for PVDF). A strong electric field is applied which aligns the dipoles of the crystals. At this point, piezo-polymers, such as PVDF, require significant stretching to create a net dipole moment. The material is then cooled, while the electric field still remains. After the material has cooled and the electric field is removed, the material has a net alignment of its dipoles [19]. In some instances it is also possible to control the poling process at room temperature [20, 21]. Controlling the different steps of the poling process allows a variety of different piezoelectric materials to be made with different shapes and different polarisation directions.

There are several parameters that describe the electro-mechanical behaviour of piezoelectric materials. Three of the most useful are:

- The piezoelectric strain coefficient (d in m/V), which describes the displacement induced in the material per unit voltage. This describes how efficiently an applied voltage is converted into a displacement or pressure [19].
- The piezoelectric voltage coefficient (g in Vm/N), which describes the electric field induced per unit of applied stress. This describes how efficiently an applied stress or pressure is converted to voltage.
- The electro-mechanical coupling factor (k), which indicates how efficiently the mechanical and electrical energy are converted from one another [19].

In general, PZT transducers have a high piezoelectric strain constant and coupling coefficient ($d \approx 590, k \approx 0.5$), making them excellent transmitters of ultrasound [19]. However, the piezoelectric voltage constant is low ($g \approx 20$), which makes them poor receivers. One of the main limitations of using PZT in biomedical imaging is that it has a much higher acoustic impedance than water. Therefore a matching-layer material must be used. The matching-layer has an impedance value between the ceramic and water and improves the performance of the transducer. The impedance mismatch causes PZT transducers to have resonant behaviour

which reduces the transmit and receive bandwidth to be localised around the centre frequency.

PVDF has an acoustic impedance closer to that of water. This makes it more applicable than PZT as a sensing element in hydrophones for exposimetry. As they are well matched, PVDF does not exhibit highly resonant behaviour and has a wider frequency bandwidth. Additionally, the piezoelectric voltage constant for PVDF is high ($g \approx 230$), which makes it an excellent material for detecting ultrasound. However, the piezoelectric strain and coupling coefficient are low ($d \approx 25, k \approx 0.15$), which make it a poor transmitter. Hence, PVDF is mainly used for the detection of ultrasound [19].



Figure 1.4: (a) A selection of different needle hydrophones (Precision Acoustics, Dorset, UK). (b) Membrane hydrophone (Precision Acoustics, Dorset, UK). (c) Capsule hydrophone (Onda Corporation, CA, US).

1.3.1.2 Needle Hydrophones

Needle hydrophones generally have a small PVDF sensing element ($40 \mu\text{m}$ to 1 mm) at the end of a thin walled metal tube. The compact nature of these hydrophones make them suitable for measuring acoustic fields where other hydrophones, for example membrane hydrophones, cannot fit [3]. Additionally, their small profile reduces the perturbation effect on the acoustic field being measured.

Needle hydrophones typical exhibit rapid fluctuations in sensitivity at low frequencies. An example of the amplitude and phase frequency-response of two needle

hydrophones can be seen in Figure 1.5. Diffracted waves around the tip of the needle hydrophone propagate across the active element which create an interference pattern on the surface. The interference pattern depends on a number of factors, including the needle tip geometry, the wavelength, and the incident angle of the acoustic wave [19, 22]. Additionally, there are guided wave modes which are excited on the surface of the needle. These factors cause the fluctuations seen at low frequencies for needle hydrophones. These effects can be somewhat mitigated by modifying the shape of the tip [23].

The directional response of the hydrophone is affected by the element size, where a smaller element has a flatter directional response, but also a reduced sensitivity. The reduction in sensitivity with decreasing element size can be seen in the collected values for NEP that are included in Table 1.1. Wear investigated the directional response of four needle transducers of varying element diameter from 200-1000 μm [3]. The results from one of the transducers can be seen in Figure 1.6 which shows the directional response of the measured and modelled data at different values of ka . The measured data has a similar response to the models described in Section 1.2. In general, at high values of ka the effective active element size was the same as nominal element size. However, the models either over- or under-estimated the element size at low values of ka [3].

1.3.1.3 Membrane Hydrophones

Membrane hydrophones consist of a thin sheet of PVDF stretched on a circular frame, where a small region in the centre acts as the active element which is typically between 0.2 to 1 mm. Generally, the frame is wide enough to not interfere with the beam or field being measured, however, the large planar surfaces can cause reflections which affect measurements [3]. The thin membrane (0.9 to 25 μm) is smaller than the acoustic wavelength in water (75 μm at 20 MHz). Therefore, the perturbation effect of the hydrophone on the acoustic field is reduced. When comparing a needle and membrane hydrophone of a similar active element size, the needle hydrophone is generally more sensitive [19]. This arises from the design of the two hydrophones. Membrane hydrophones are designed to be acoustically

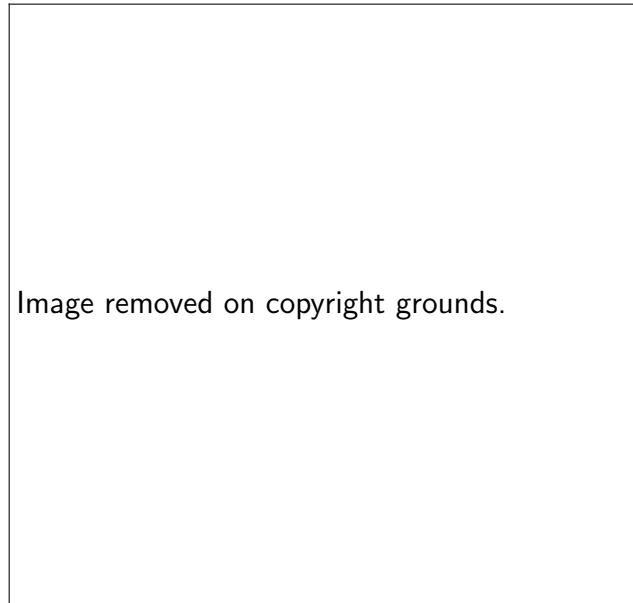


Figure 1.5: Frequency response for membrane (M) and needle (N) hydrophones of different element sizes. This figure has been reproduced from Martin and Treeby [24].



Figure 1.6: Directional response versus different models of directivity for a needle hydrophone (DIBE-0600, force Technology Institute, Brondby, DK). This figure has been reproduced from Wear [3].

transparent whereas needle hydrophones have a rigid termination at the back. This means as an acoustic wave passes through a needle hydrophone there is a reflection at the back of the piezoelectric element, and the acoustic wave is effectively measured twice [19]. This can be seen in the NEP values seen in Table 1.1. There are backed membrane hydrophones which do not suffer from this disadvantage, how-

Table 1.1: Table of noise-equivalent pressure values.

Hydrophone	Active Element Diameter	NEP [Pa]	NEP [mPa $\sqrt{\text{Hz}}$]	Ref
Needle	1.0 mm	7 ¹	0.7	[19]
Needle	0.5 mm	200 ¹	20	[19]
Needle	0.2 mm	1.09k ¹	109	[19]
Needle	0.075 mm	6k ¹	600	[19]
Membrane	0.4 mm	1.7k ¹	170	[19]
Membrane	0.2 mm	4k ¹	400	[19]
Membrane	0.5 mm	5k ²	800	[16]
Membrane	0.2 mm	3k ²	600	[16]
Membrane	0.075 mm	55k ²	11000	[16]
cMUT	0.25 mm	-	0.9	[25, 26]
cMUT	0.07 mm	-	3	[26]
Eisenmenger FOH	100 μm	500k ³	111000	[27, 19]
FP Polymer film	64 μm	210 ³	49	[28]
FP Multilayer FOH	5 μm	30k ³	6708	[29, 19]
FP Multilayer polymer	60 μm	180 ³	40	[30]
Planoconcave sensor	12.5 μm	2.6 ⁴ to 9.8 ⁴	1.6 to 3.3	[31]

¹Rms noise level over a 100 MHz measurement bandwidth. ²Peak NEP measured over a 25 MHz bandwidth. ³Rms values over a 20 MHz bandwidth. ⁴Rms NEP values of 2.6 Pa for a 2.8 MHz Bandwidth and 9.8 Pa for a 8.9 MHz bandwidth.

ever, these were primarily constructed to decrease the occurrence of jitter and not to improve the NEP .

The amplitude and phase frequency response of membrane hydrophones is smooth, varying ± 3 dB over a range of 0 – 45 MHz [32, 20, 9]. At high frequencies there may be a thickness resonance which depends on the membrane thickness. An example of the frequency-response for two membrane hydrophones can be seen in Figure 1.5. Over this frequency range, the membrane hydrophones have a smoother amplitude and phase frequency response when compared with needle hydrophones. Because of these characteristics, membrane hydrophones are currently the gold standard for transducer characterisation in water-tanks [19]. However, there are other common techniques for hydrophone calibration [33, 22, 34, 20]. Over small angular ranges ($\pm 35^\circ$) the directional response of membrane hydrophones agrees with the models described in Section 1.2 (see Figure 1.7). However, at large angles $> 35^\circ$ and low frequencies there are large side lobes. These occur from the presence

of guided (Lamb) modes excited in the membrane hydrophone [18]. The directional response can be seen in Figure 1.7.

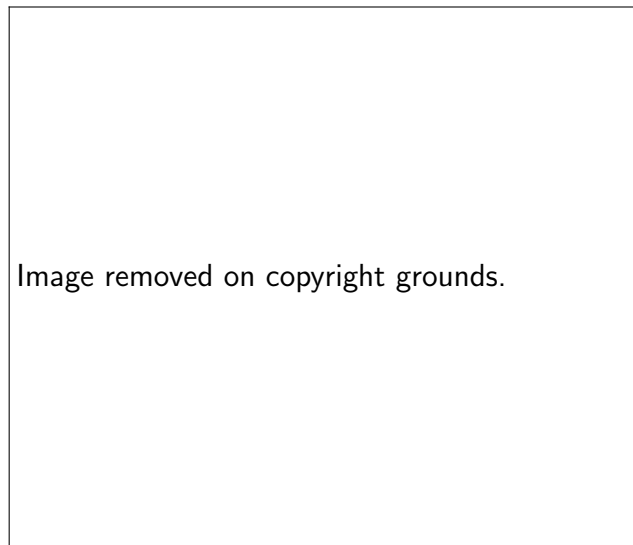


Figure 1.7: Directional response versus different models of directivity for DIBE-0600 membrane hydrophone. Figure reproduced from Wear [14].

1.3.2 Capacitive Micromachined Ultrasonic Transducers

An emerging alternative technology to piezoelectric transducers are capacitive micromachined ultrasonic transducers (cMUTs). With reference to Figure 1.8, an air or vacuum cavity is formed between two heavily doped silicon electrodes and a metalised membrane. When cMUTs are used for transmission, a DC and AC voltage are applied. The DC voltage alters the height between the top and bottom electrode as they are attracted to one another, and the AC voltage modulates the membrane to produce an ultrasound wave [35]. When the cMUT is used to receive ultrasound, only a DC voltage is applied. The incident ultrasound wave modulates the distance between electrodes, hence its capacitance, and this is converted to an oscillating voltage and amplified [35, 36]. The center frequency of the membrane can be controlled by varying the DC voltage and distance between the electrodes [37]. There is a small impedance mismatch between the vibrating membrane and the coupling fluid which helps avoid the need for matching layers [38, 39, 19]. This allows for a broader bandwidth and good transduction efficiency [40].

The concept for these transducers has been present since early piezoelectric

devices but at that time the existing technology was not able to manufacture what was needed [41]. This is due to the cMUT requiring strong electric field strengths of millions of volts per centimetre, so that electrostatic forces on the order of kilograms per square centimetre can be generated [36]. It is mainly from the advances in micro-fabrication techniques in the early 2000's which have allowed this technology to develop. One main advantage of a cMUT over traditional piezoelectric elements is that large custom 2D arrays can be easily produced using photolithography (the same technique used for producing silicon based integrated circuits). Recently, emerging products such as the Butterfly iQ [42] are demonstrating cMUTs can emulate different types of transducer arrays and deliver clinically suitable images at a fraction of the cost of clinical ultrasound machines.

When used for detection, the cMUT has two main modes of operation. The first is the "conventional" mode where a DC voltage is applied and the membrane does not touch any part of the substrate. This mode of operation has a reduced sensitivity (-10 dB) compared to piezoelectric elements [43]. The second mode of operation, called "collapse" mode, is when the centre of the membrane is made to touch the substrate. When the pressure wave is incident, the membrane has a greater volume displacement, giving it a higher sensitivity than the conventional mode [37].

A disadvantage of cMUTs common to both modes of operation is that the bandwidth and frequency response of the cMUT are affected by the higher order vibrational modes of the membrane [44]. An example of the frequency response can be seen in Figure 1.9. Additionally, these vibrations may propagate into neighbouring elements, causing significant acoustic cross-talk [45, 46].

In one study, the measured directional response for a cMUT element was compared with a PZT element of the same size ($200 \mu\text{m}$ pitch, central frequency 5 MHz). The measured directivity of the cMUT element was shown to be smoothly varying and have a wider angular range than the equivalently size piezoelectric element [40, 47, 48]. However, the PZT was 7.8 dB more sensitive than the cMUT element at normal incidence. The directivity measurements are shown in Figure 1.10. There are few directivity measurements of cMUT elements, so it is not pos-

sible to say if these results are representative of all types. The elements measured (shown in Figure 1.10) are relatively large hence the directional response appears to be dominated by the effect of spatial averaging. The effect of membrane vibrational modes may become apparent for smaller cMUT elements, as is shown in the frequency-response in Figure 1.9.

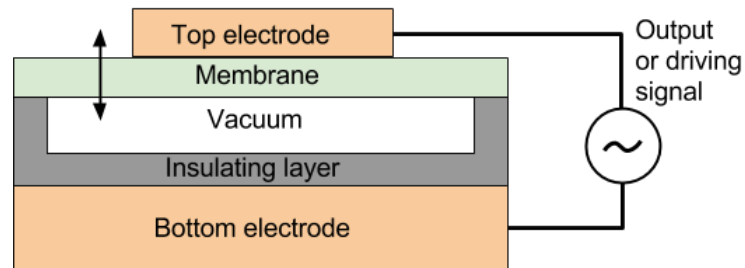


Figure 1.8: Diagram of a cMUT.

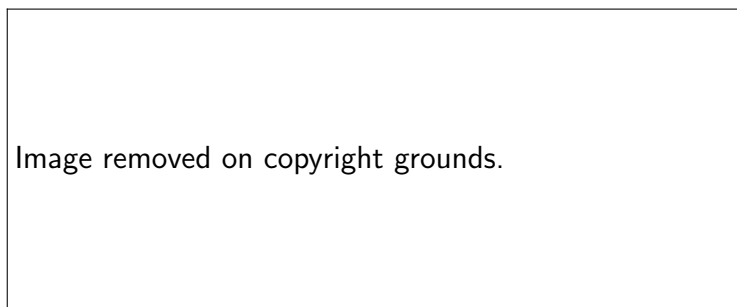


Figure 1.9: Frequency response of a cMUT. There are many features caused by higher-order vibrational modes on the membrane. This figure has been partially reproduced from Hall [44].

1.3.3 Optical Hydrophones

1.3.3.1 Introduction to Optical Hydrophones

The optical detection of ultrasound provides a range of alternatives to piezoelectric hydrophones and cMUTs. Optical methods rely on changes of intensity, phase or polarisation of light to detect ultrasound [19]. The optical hydrophones described in the following sections generally fall within one of two categories: intrinsic or extrinsic hydrophones. The transduction mechanism of intrinsic sensors, for example the Eisenmenger hydrophone, is based on the interaction of light and sound within the fibre itself. Conversely, extrinsic sensors, rely on an external detection element

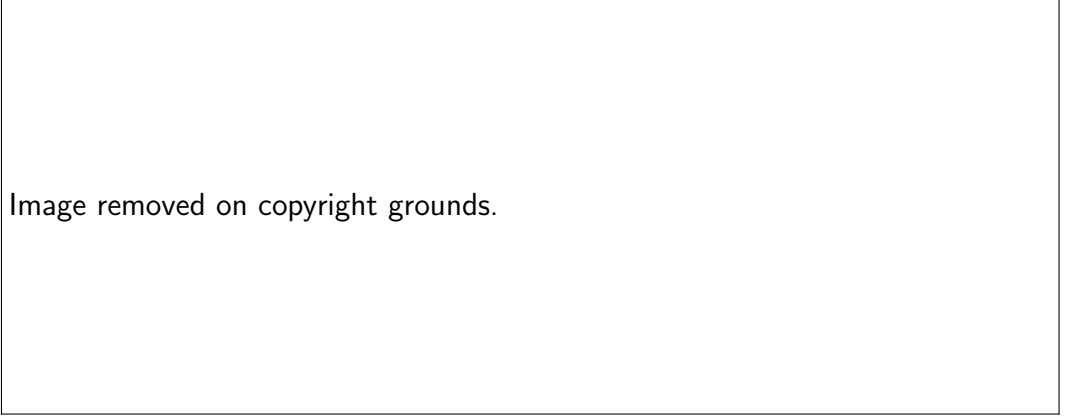


Image removed on copyright grounds.

Figure 1.10: Directivity of a PZT element, and an equivalently sized cMUT. Note the cMUT has a broadband directional response at low frequencies. This figure has been partially reproduced from Rebling [40].

and an optical fibre or a transparent substrate is used to transmit light to and from the sensor [49, 50, 4]. The Fabry-Pérot interferometer is an extrinsic sensor and can be manufactured as fibre-optic sensor, a plano-concave sensor, or as a planar sensor. The planar configuration of the sensor is the main focus of the thesis and is described in greater detail in Chapter 2.1.

Optical hydrophones can provide a number of benefits over piezoelectric hydrophones and a few examples are given here. Firstly, the effective element sizes of FOHs can be considered to be the diameter of the fibre-core. However, it has been shown that the whole fiber tip acts mechanically with the sound wave and contributes to the effective element size [51]. Generally, these sensors have smaller element sizes than piezoelectric devices. The small effective element size means these sensors are less likely to suffer from spatial averaging effects. Additionally, unlike piezoelectric elements, the sensitivity of optical hydrophones does not necessarily decrease with element size as more power can be coupled into the interrogation laser [19]. Hence, optical-hydrophones can have effective element sizes as small as a few microns and be more sensitive than a piezoelectric element of an equivalent size at small element sizes (< 1 mm) [19].

Additionally, there are a number of other benefits that arise from using optical hydrophones. The nature of optical measurements mean these sensors are less prone to electromagnetic interference. The FOH cables are flexible and small which

allows them to be used in places of restricted access. The FOHs can be made robust to high-intensity ultrasound fields and can be replaced more readily while maintaining small effective element sizes [13]. Membrane and needle hydrophones can be made robust and maintain low NEPs, however, these modified hydrophones have a relatively large element size [5, 9, 52, 53, 54]. This can be seen in Table 1.1.

1.3.3.2 Eisenmenger Hydrophone

Some optical detection techniques use the acousto-optic effect where the pressure of the acoustic wave causes a time-varying change in density in the medium through which the wave is propagating [27, 55]. The change in density causes a change in refractive index which can be detected by an interrogating laser beam. One such example using this technique is the Eisenmenger hydrophone [27]. Here, light from a laser is coupled into the core of an optical fibre. At the distal end of the fibre there is a mismatch in the refractive indices of the fibre (fused silica) and water, hence some of the laser light is reflected back. The reflected optical power is measured by a photodiode. An incident acoustic wave modulates the refractive indices of the fused silica and water. This causes a change in the optical reflection coefficient and intensity of the reflected optical power [19, 13].

Compared to other fibre-optic hydrophones, the Eisenmenger hydrophone has very low sensitivity and requires a relatively high-powered interrogation laser to detect the small refractive index changes [51]. These sensors are at least an order of magnitude less sensitive than an equivalent piezoelectric hydrophone (Table 1.1) [19]. This makes it unsuitable for measuring the pressure of low intensity fields. However, the simplicity of this sensor is its main advantage. It is extremely robust making it ideal for measuring fields of high acoustic intensity, for example, measuring shock waves in lithotripsy [19, 13]. Some examples of the directional response of an Eisenmenger FOH are shown in Figure 1.11. The response generally follows the models demonstrated in Section 1.2, in particular the model suggested by Krucker [17] which uses the whole fiber as the effective element radius. However, the models underestimate the sensitivity at large angles of incidence at high frequencies. Wear suggests that this is due to the low pressure produced by the high

frequency transducer so the measurement is comparable to the noise level [13].

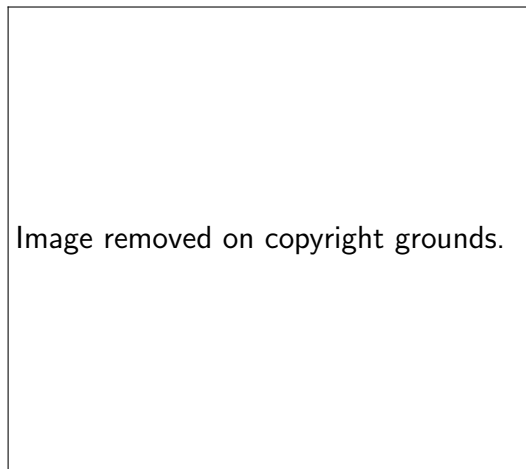


Figure 1.11: Directional response of an Eisenmenger fibre-optic hydrophone. This figure has been partially reproduced from Wear [13].

1.3.3.3 Fabry-Pérot Sensor

The Fabry-Pérot sensor consists of two partially reflective mirrors separated by an optically transparent spacer forming an interferometer. An interrogation laser beam is multiply reflected by the mirrors and the intensity of the reflected optical power is measured. When an ultrasound wave is incident on the sensor, there is a change in the reflected power through the modulation of the spacer thickness and refractive index. The transduction mechanism of a planar Fabry-Pérot sensor is discussed in greater detail in Chapter 2.

There are a number of different configurations of Fabry-Pérot sensors which affect the frequency-response and directional response. To summarise the main configurations: a planar sensor deposited on a large flat substrate, a planar sensor deposited on the distal end of an optical fibre, a plano-concave dome shaped sensor deposited on a large flat substrate or fibre, and a curved sensor deposited on a tapered fibre. For all of these configurations, the mirrors may be a single metallic layer (such as aluminium) or be made from a number of alternating dielectric layers. The thickness of the material spacer varies from a few microns to hundreds of microns.

The frequency response of the sensor is determined by the materials of the

sensor spacer and backing and the thickness of spacer. Generally, the resonant frequency of the spacer determines the bandwidth. A thicker spacer (100s of μm) has a lower bandwidth and a thinner spacer (10s of μm) has a larger bandwidth. This is illustrated in Figure 1.12. However, there is a trade off in sensitivity and spacer thickness, as a thicker spacer is more sensitive than a thinner spacer.



Figure 1.12: Frequency response of plano-concave microresonators at different thicknesses. A thinner spacer has a wider bandwidth but lower sensitivity. This figure has been partially reproduced from Guggenheim [4]

The active element size of the planar Fabry-Pérot sensor can be approximately considered to be the diameter of the interrogation laser beam. For a fiber-optic sensor this is closer to the outer fiber diameter. This varies depending on the profile of the interrogation beam. However, even with small element sizes, the sensitivity is comparable with other hydrophones with element sizes orders of magnitude larger. This can be seen in Table 1.1. This means the directional response of the Fabry-Pérot sensor is noticeably different to other hydrophones as the effects of spatial averaging are negligible and the main features of the directional response are caused by the interaction of the incident wave with the sensor. The directional responses of Fabry-Pérot sensors are unique for each configuration and a few examples are included here: a planar sensor on a large flat substrate (Figure 1.13), a planar and curved FOH (Figure 1.14) and a plano-concave sensor can be seen in (Figure 1.15).

There are a number of other factors which affect the features in the frequency-response. For example, the thickness of the mirrors relative to the spacer, how

well matched the backing and spacer is with water, and geometrical factors such as diffraction effects around the tip of an optical fibre. Similar to needle hydrophones, tip effects of FOHs can be ameliorated through tapering [56].

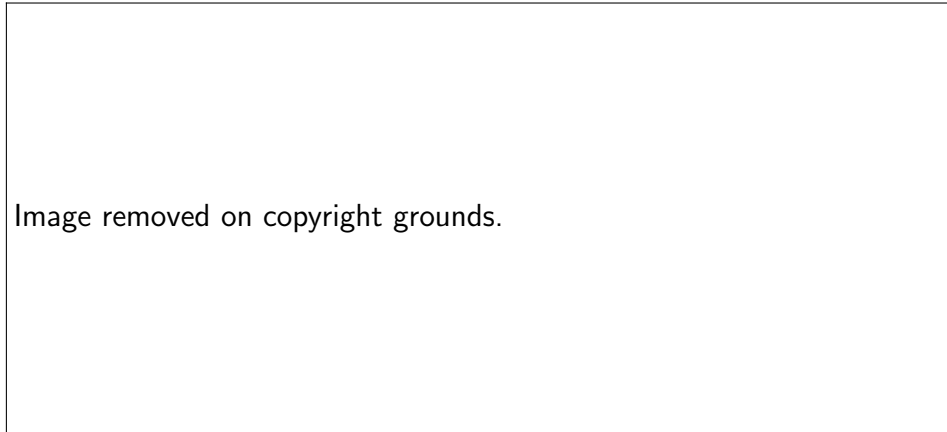


Figure 1.13: (a) Frequency-dependent directional response of a planar Fabry-Pérot sensor with soft-dielectric mirrors a Parylene C spacer and ZEONEX substrate. (b) Profiles of the directional response. This figure has been reproduced from Buchmann [57].

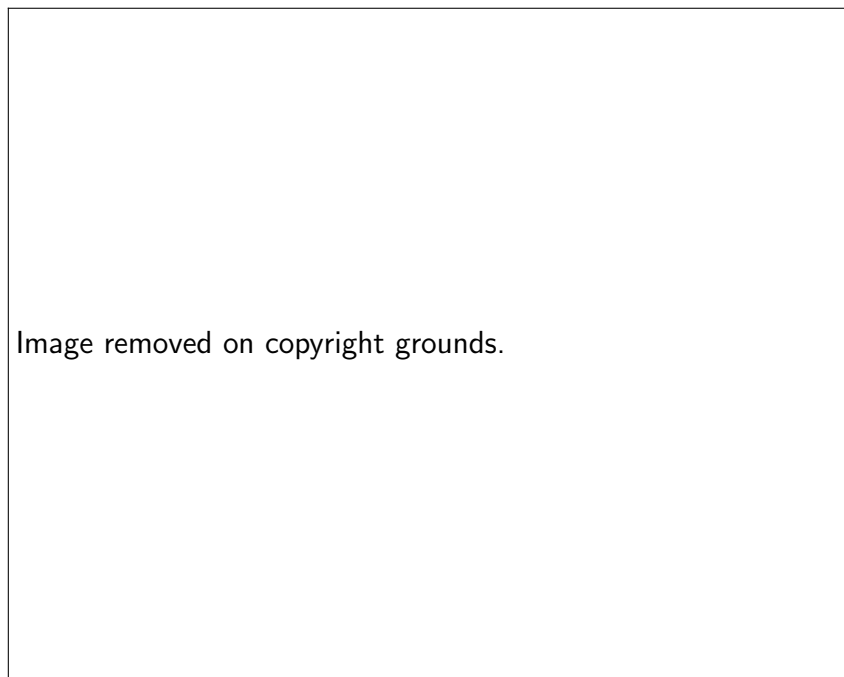


Figure 1.14: (Left) Frequency-dependent directional response of a planar Fabry-Pérot ultrasound sensor deposited on a flat optical fibre. (Right) Frequency-dependent directional response of a curved (Fabry-Pérot sensor deposited on a tapered fibre. Profiles of the directivity measurements are plotted below. This figure has been reproduced from Zhang [58].

Image removed on copyright grounds.

Figure 1.15: (Left) Frequency-dependent directional response of a plano-concave Fabry-Pérot sensor. (Right) Profiles of the directional response. The modelled directional response for a 2 mm circular disk of equivalent sensitivity to the plano-concave sensor is plotted in both figures. The response of the plano-concave sensor is more omni-directional than the 2 mm disk. Figure partially reproduced from Guggenheim [4].

1.4 Summary

This chapter introduced different hydrophones and discussed their transduction mechanisms and directional response. A key takeaway is that a simple spatial averaging model of the directional response based on a circular piston in a rigid baffle is not suitable for describing the response of hydrophones with small element sizes. However, the simple diffraction approach may be useful for small angles of incidence and when used in combination with frequency dependent effective radii. For some sensors, especially the Fabry-Pérot sensor, the directional response differs greatly from these simple models and requires a more rigorous modelling approach.

1.5 Thesis Objectives and Structure

This thesis is focused on modelling the frequency-dependent directional response of planar Fabry-Pérot ultrasound sensors. These sensors can detect ultrasound over a broadband frequency range (tens of MHz) and maintain high sensitivity with small element sizes (tens of microns) [28]. These sensors are frequently used in photoacoustic imaging, as a reference sensor for hydrophone calibration, and can also be used for general ultrasound field characterisation [59, 49, 60, 7, 28, 61, 50, 62, 19]. For a planar sensor interrogated by a sufficiently small spot size, the directional

response of this sensor is dominated by the complex wave-field within the sensor caused by the interaction of elastic waves with the multilayered structure of the sensor.

An accurate model of the directional response will provide an understanding of the underlying physics present in the sensor, specifically, where acoustic critical angles and guided-wave modes are generated and their effect on the sensors sensitivity. These details are essential in optimising the Fabry-Pérot design to tailor-make sensors with specific applications in mind. For example, sensors with a flat and omnidirectional response could be designed by selecting materials with properties that, when insonated, do not excite any guided waves in the sensor.

A model of the directivity, and in particular of how it relates to the specific wave modes in the sensor, will not only inform future sensor design, but can be used to deconvolve the directional response from array measurements made with the sensor. The use of an analytical model for the deconvolution provides a number of benefits over using the measured directivity including 1) the model does not suffer from noise, 2) the phase can be accurately calculated, 3) a larger range of angles and frequencies can be used in the deconvolution process [8, 5].

The general aims of this thesis are:

- To model the directional response of the planar Fabry-Pérot interferometer using multilayered elastic models.
- To determine the underlying physical phenomena which cause different observable features of the directional response.
- To provide a simple toolbox allowing users to model, predict and optimise the directional response of Fabry-Pérot sensors.

The remainder of the thesis is structured as follows. Chapter 2 introduces the Fabry-Pérot sensor in greater detail and discusses the transduction mechanism. Chapter 3 presents the global matrix and partial wave methods for modelling elastic wave propagation in multilayered media. This is needed to model the multilayered structure of the Fabry-Pérot sensor and to gain an understanding of the underlying

physical mechanisms. The implementation and numerical validation of the partial-wave method is given in Chapter 4. This developed code has been released as an open-source MATLAB toolbox (www.elasticmatrix.org), and the code structure and practical examples are demonstrated in this section. The comparison of the measured and modelled directional response of glass etalon sensors is given in Chapter 5. Further analysis is provided in Chapter 6 for soft-polymer sensors where the spacer is made from Parylene C. The main conclusions and future work are collated in Chapter 7.

Chapter 2

The Fabry-Pérot Sensor

2.1 Introduction

The previous section outlined the main technologies used for detecting ultrasound including piezoelectric hydrophones, capacitive micromachined ultrasonic transducers, and optical hydrophones. This section describes the planar Fabry-Pérot ultrasound sensor in greater detail.

The form of the Fabry-Pérot sensors discussed in this thesis are based on the original interferometric idea developed by Charles Fabry and Alfred Perot in 1899 [63, 64]. Figure 2.1 demonstrates the planar form of the Fabry-Pérot interferometer. As described in Section 1.3.3.3, the same sensing device may also be deposited on the tip of an optical fibre and may have curved mirrors.

The planar Fabry-Pérot sensor consists of two partially reflective mirrors separated by an optically transparent spacer deposited on top of a substrate backing. The partially reflective mirrors may be a single metallic material or an alternating stack of dielectric mirrors. The substrate backing may either be a flat or wedged shaped block (used to reduce parasitic interference from the substrate), or the substrate may be the tip of an optical fibre [7]. An interrogating laser beam at the base of the substrate is multiply reflected between the mirrors and the intensity of the reflected optical power is measured. The reflected intensity is dependent on the optical phase difference between both mirrors. A phase shift occurs from two mechanisms: firstly, an incident ultrasonic wave displaces the mirrors from their initial

positions, and secondly, the mechanical strain of the spacer causes local changes in the refractive index [65, 66]. Additionally, the refractive indices of the mirror layers is modulated as well, as is that of the substrate and the surrounding fluid [60, 50]. This contributes to the transduction through additional phase changes of the interfering optical waves in the interferometer as well as through reflectance changes of the interferometer mirrors. For interference filter designs using spacer thicknesses of only $\lambda/2$ or small multiples of that, the mirror thickness may contribute to the effective spacer thickness in a significant way [19]. The transduction mechanism is expanded in further detail in Section 2.4. The journal article in [67] © IEEE 2019 has been adapted to form parts of this chapter.

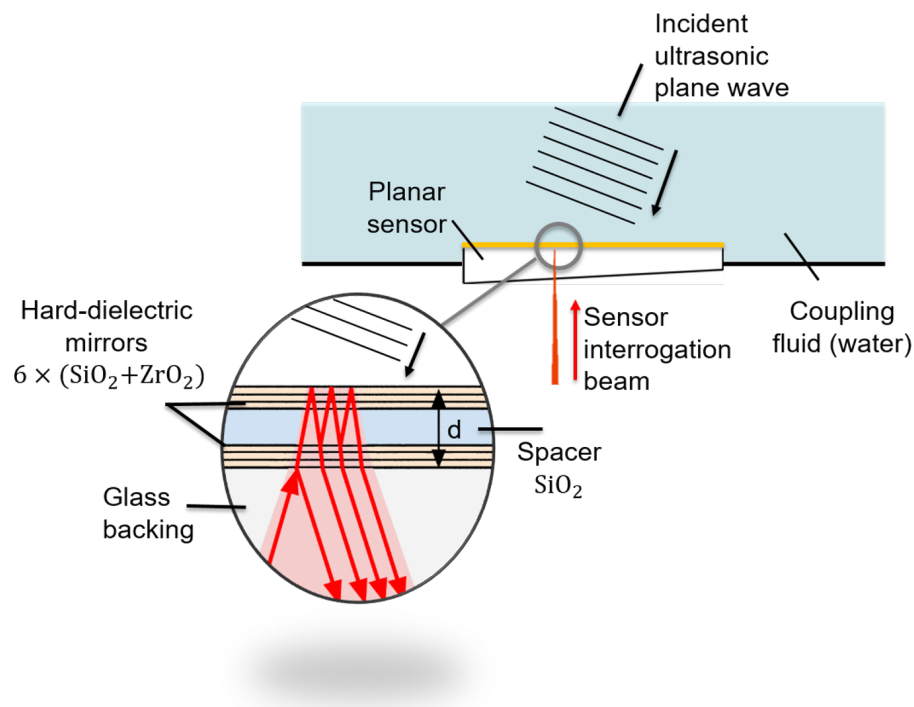


Figure 2.1: Example of a hard-dielectric planar Fabry-Pérot interferometer. The interferometer consists of two mirrors separated by an optically transparent spacer. A laser incident at the base of the interferometer is multiply reflected and the reflected intensity is measured. An acoustic wave modulates the reflected intensity. Figure reprinted from [67] © IEEE 2019.

2.2 Fabrication

The dielectric mirrors, thin film mirrors, and optically transparent spacer are deposited onto the substrate using physical vapor deposition. This process provides

a conformal coating and uniform thickness [66, 68]. When using vapour deposition, the thickness of the material is dependent of the length of time the material spends in the deposition chamber [69]. This method allows the spacer to be made from only a few microns thick to tens of microns allowing for broad detection bandwidths from the tens of MHz to the GHz range [60, 70, 71]. However, there is a trade-off between bandwidth and sensitivity. A thin spacer has a broader detection bandwidth but is less sensitive when compared with a thicker spacer.

The exact materials used when fabricating the sensor varies with the intended application. For example, a sensor built with a glass spacer presents with different characteristics to a polymer spacer. A polymer has a lower Young's modulus than glass hence for the same incident acoustic pressure, the polymer has a greater deformation. The sensitivity of the sensor is dependent on the rate of change of the optical phase difference between the two mirrors, therefore a greater deformation causes a greater phase change and hence a greater sensitivity. For low acoustic pressures, a polymer based sensor is more sensitive than a glass based sensor of equivalent thickness. However, for high acoustic pressures, the measured response of the polymer sensor may be saturated, or worse, the sensor destroyed. In this scenario a glass sensor is more suitable [5].

2.3 Interferometer Transfer Function

The phase interferometry transfer function (ITF) describes the variation of the reflected optical power as a function of the optical phase difference between the two Fabry-Pérot mirrors. Some examples of this function for different mirror reflectivities are given in Figure 2.2 (a), assuming a collimated laser beam at normal incidence, no losses, and no phase changes at the mirrors. It can be seen when the reflectivities of the mirrors are high ($R = 0.9$), the ITF has a sharper fringe and a broad maximum, whereas for low reflectivities ($R = 0.1$), the transition between maximum and minimum is smoothly varying. The fringes occur when the cavity is in resonance and the thickness is equal to an integer multiple of the half-wavelength

$(\lambda_0/2)$ of the interrogating light. This is described by

$$2n_c d_c = N\lambda, \quad (2.1)$$

where the variables n_c and d_c are the refractive index and thickness of the cavity, and N is an integer value [72]. When the sensor is in resonance, the light within the optical cavity constructively interferes with itself and destructively interferes with the reflected light from the first mirror. Hence there is a minimum in the ITF [72]. Conversely, out of resonance the light inside the cavity destructively interferes with itself and the light reflected from the first mirror is mostly unperturbed. Hence, out of resonance there is only a small or no change in the reflected light intensity [72].

When the interferometer is used for detection, the wavelength of the interrogating laser is set to be on the slope of one of the fringes. This is said to be the bias point. An incident acoustic wave causes a change in optical thickness and a change in refractive index, the ITF shifts and there is a change in the reflected intensity. An example can be seen in Figure 2.2 (b). The maximum sensitivity is found when the laser is tuned to the maximum slope of the ITF. The sharper the fringes of the ITF, the more sensitive the sensor is. The change in phase with pressure is called the acoustic phase sensitivity and this is essential for calculating the directivity of the planar Fabry-Pérot sensor.

With planar sensors, a focused interrogation laser beam diverges on each round trip within the optical cavity. This lateral “walk-off” reduces the fringe depth and the maximum achievable sensitivity. Recently, plano-concave sensors were introduced to ameliorate the effect of lateral walk-off. These sensors are constructed from a plano-concave polymer microcavity between two highly reflective mirrors [31]. The microresonators are embedded in a layer of an identical polymer to give an acoustically homogeneous planar structure. Though the structure may not be acoustically homogeneous if the mirrors are thick compared to the plano-concave dome height. The plano-concave sensor matches the divergence of the focused laser beam to the curvature of the top-mirror. This refocuses the laser light in the microcavity, eliminating walk-off. The improved visibility of the fringe means the sensors have

a sharper fringe and have been shown to be more sensitive than planar Fabry-Pérot sensors [31]. Since the microresonators are embedded in a polymer to give an acoustically flat structure, the modelling process outlined in the rest of this thesis could also be applied to these sensors.

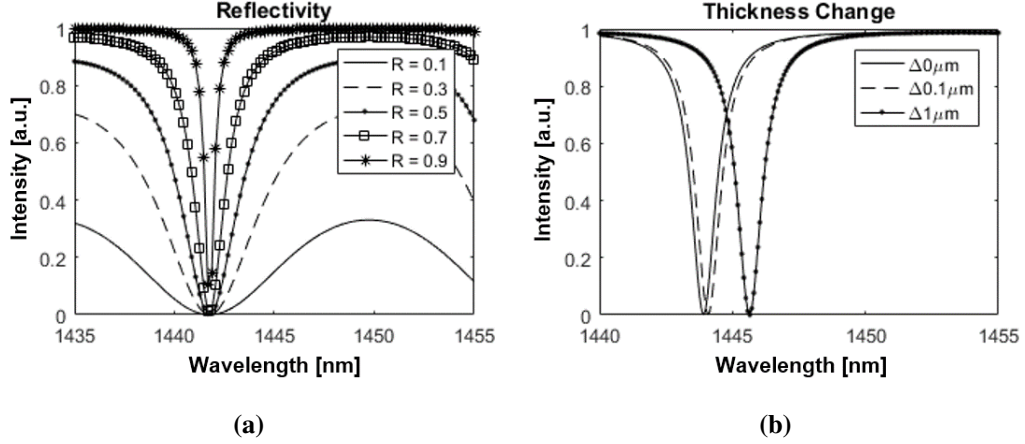


Figure 2.2: (a) Variation of the ITF function with different reflectivities. (b) Shifting effect of the ITF fringe when the cavity length changes.

2.4 Acoustic Phase Sensitivity

If the shift of the ITF from an incident acoustic wave is small then the change in reflected optical power is linearly proportional to the pressure of the acoustic wave. For one round trip within the Fabry-Pérot cavity, the change in optical phase with respect to acoustic pressure is dependent on two mechanisms. The first is the change of refractive index with pressure, and the second is the change in displacement between the two mirrors of the Fabry-Pérot cavity. Note, the contributions from the changes in the refractive indices and reflectivities of the mirrors are neglected here. With reference to Figure 2.3, the total phase change is

$$\phi = \frac{4\pi}{\lambda_0} \int_{u(0)}^{L+u(L)} n(z) dz, \quad (2.2)$$

where $u(z)$ is the displacement of the mirror as a function of position z , where the first mirror is located at $z = 0$ and the second mirror is located at $z = L$. This equation describes how the phase is proportional to the integral of the refractive

index changes across the entire cavity. If there is no acoustic field then $u(0) = u(L) = 0$, and $n(z)$ is constant so the equation simplifies to an expression for the static cavity

$$\phi = \phi_0 = \frac{4\pi n_0 L}{\lambda_0}.$$

The phase change from the presence of an acoustic wave can be expanded as

$$\Delta\phi = \phi - \phi_0 = \frac{4\pi}{\lambda_0} \int_{u(0)}^{L+u(L)} n(z) dz - \frac{4\pi n_0 L}{\lambda_0}, \quad (2.3)$$

$$= \frac{4\pi}{\lambda_0} \int_{u(0)}^{L+u(L)} (n_0 + \Delta n) dz - \frac{4\pi n_0 L}{\lambda_0}, \quad (2.4)$$

$$= \frac{4\pi}{\lambda_0} \int_{u(0)}^{L+u(L)} n_0 dz + \frac{4\pi}{\lambda_0} \int_{u(0)}^{L+u(L)} \Delta n dz - \frac{4\pi n_0 L}{\lambda_0}, \quad (2.5)$$

where $n(z) = n_0 + \Delta n(z)$, which is expanded in Section 2.5. Evaluating the first integral, the equation simplifies

$$\Delta\phi = \frac{4\pi n_0}{\lambda_0} \left(L + u(L) - u(0) \right) + \frac{4\pi}{\lambda_0} \int_{u(0)}^{L+u(L)} \Delta n dz - \frac{4\pi n_0 L}{\lambda_0} \quad (2.6)$$

$$= \frac{4\pi n_0}{\lambda_0} \left(u(L) - u(0) \right) + \frac{4\pi}{\lambda_0} \int_{u(0)}^{L+u(L)} \Delta n dz, \quad (2.7)$$

where the change in displacement of the mirrors is

$$\Delta d = u(L) - u(0). \quad (2.8)$$

Relating the change in ϕ with a unit change in pressure, the acoustic sensitivity can be written as

$$A_s = \frac{4\pi}{\lambda_0} \left(n_0 \Delta d + \int_{z_1}^{z_2} \Delta n \cdot dz \right). \quad (2.9)$$

where $z_2 = L + u(L)$, $z_1 = u(0)$. There are now two terms describing the change in ϕ . The first term, Δd , describes a phase change from a change in distance from the displacement of the mirrors. The second term, Δn , describes the phase changes from the integral of the refractive index changes in the spacer. The refractive index change of the spacer/cavity material is induced by local changes in density caused by the compression and expansion of the pressure wave [73].

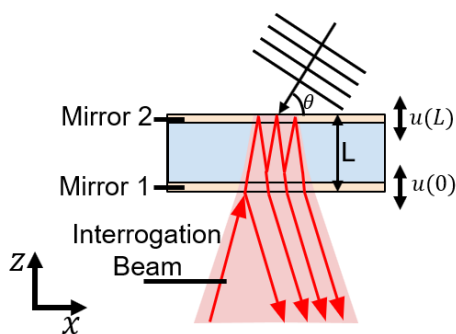


Figure 2.3: Coordinate system for the sensor. The vertical lines 1 and 2 represent the locations of the mirrors which are distance L apart. $u(z)$ is the displacement of the mirrors located at $z = 0$ and $z = L$. The angle of incidence of the plane acoustic wave is given by θ .

2.5 Variation of Refractive Index with Pressure

A refractive index grating is produced when a medium is under a mechanical strain from an acoustic wave. The interaction of light with this refractive index grating is termed an acoustooptic interaction. This subsection follows the derivation from [74] and introduces the strain-optic tensor and its importance in determining the change in refractive index with pressure.

Generally, an un-strained material has three principle refractive indices which can be represented geometrically by an ellipsoid, as shown in Figure 2.4. Here, the length of the semi-axes indicate the refractive index seen by an electric field polarised in that axis. Assuming, initially, the axes of the index-ellipsoid coincide with the acoustic (x, y, z) axes, the ellipsoid is represented with

$$\frac{x^2}{n_x^2} + \frac{y^2}{n_y^2} + \frac{z^2}{n_z^2} = 1, \quad (2.10)$$

where the principal refractive indices are given by n_x, n_y, n_z . If the material is optically isotropic, the principal refractive indices are $n_x = n_y = n_z = n_0$. If the material is biaxial it is described by three different refractive indices, hence $n_x \neq n_y \neq n_z$. Light travelling in the z -direction polarised in the y -axis sees a refractive index of n_y , and if polarised in x , it sees a refractive index of n_x . A mechanical strain can cause an optically isotropic material to become birefringent, i.e., an un-polarised

electromagnetic wave incident at an arbitrary angle has two linear polarisations with different phase speeds. This may not be true if the mechanical strain is isotropic.

Thinking about the ellipsoid visually, the effect of a normal strain is to stretch and compress the ellipsoid and the effect of shear strain is to rotate the ellipse around its centre point. In general, the ellipsoid after an applied compressional and shear strain is given by

$$\frac{x^2}{n_1^2} + \frac{y^2}{n_2^2} + \frac{z^2}{n_3^2} + \frac{2yz}{n_4^2} + \frac{2xz}{n_5^2} + \frac{xy}{n_6^2} = 1, \quad (2.11)$$

where n_i for $i = 1, \dots, 6$ are constants which are formed from a combination of the principle refractive indices, n_x, n_y, n_z . The three axes of this new ellipsoid give the principle refractive indices of the material under mechanical strain.

In the presence of an acoustic wave, there are compressional and shear strains present within the spacer of the Fabry-Pérot interferometer. Under an arbitrary mechanical strain, the changes in $(1/n^2)_i$ of the index ellipsoid are given by

$$\Delta \left(\frac{1}{n^2} \right)_i = \sum_j p_{ij} \epsilon_j. \quad (2.12)$$

Here, p_{ij} is the strain-optic tensor and ϵ_j is the strain where the indices of $j \in \{1, \dots, 6\}$ using Voigt notation ($1 = xx, 2 = yy, 3 = zz, 4 = yz, 5 = xz, 6 = xy$). Considering an ellipsoid which initially has the principle refractive indices aligned with the acoustic axes, if the material is then subject to a combination of compressional and shear strains, the index ellipsoid becomes

$$\begin{aligned} x^2 \left(\frac{1}{n_x^2} + \sum_j p_{1j} \epsilon_j \right) + y^2 \left(\frac{1}{n_y^2} + \sum_j p_{2j} \epsilon_j \right) + \\ z^2 \left(\frac{1}{n_z^2} + \sum_j p_{3j} \epsilon_j \right) + 2yz \left(\sum_j p_{4j} \epsilon_j \right) + \\ 2xz \left(\sum_j p_{5j} \epsilon_j \right) + 2xy \left(\sum_j p_{6j} \epsilon_j \right) = 1. \quad (2.13) \end{aligned}$$

Here, n_x, n_y, n_z are the initial principle refractive indices.

If the interrogation laser of the Fabry-Pérot sensor propagates parallel to the

z -axis and is linearly polarised in the x -axis, the refractive index seen by this electromagnetic wave can be calculated from the intersection between the x -axis and the ellipsoid. The length between the intersection point and the origin is the refractive index for light polarised in x . To calculate the intersection point, z, y are set to zero which leaves n_1 as the only relevant component of Eq. (2.11). This leads to the relation

$$\frac{1}{n_1^2} = \frac{1 + n_x^2 \sum_j p_{1j} \epsilon_j}{n_x^2}, \quad (2.14)$$

$$n_1 = n_x (1 + n_x^2 \sum_j p_{1j} \epsilon_j)^{-\frac{1}{2}}. \quad (2.15)$$

If $|n^2 \sum_j p_{1j} \epsilon_j| < 1$, this can be expanded using the series approximation

$$(1 + x)^a \approx 1 + ax + \frac{a(a-1)}{2!} x^2 + \frac{a(a-1)(a-2)}{3!} x^3. \quad (2.16)$$

Taking the first two terms in the approximation then gives

$$n_1 \approx n_x \left(1 - \frac{1}{2} n_x^2 \sum_j p_{1j} \epsilon_j\right). \quad (2.17)$$

Similarly for a wave polarised in the y -axis, the equation is

$$n_2 \approx n_y \left(1 - \frac{1}{2} n_y^2 \sum_j p_{2j} \epsilon_j\right). \quad (2.18)$$

This result can now be substituted into Eq. (2.9). In general, the acoustic sensitivity is dependent on the polarisation of the interrogating laser

$$A_s = \frac{4\pi}{\lambda_0} \left(n_i \Delta d + \int_{z_1}^{z_2} \Delta n_i \cdot dz \right), \quad (2.19)$$

where Δn_i is

$$\Delta n_1 \approx -\frac{1}{2} n_x^3 \sum_j p_{1j} \epsilon_j, \quad (2.20)$$

if polarised in x and

$$\Delta n_2 \approx -\frac{1}{2}n_y^3 \sum_j p_{2j} \epsilon_j, \quad (2.21)$$

if polarised in y . For an optically isotropic, homogeneous and non-absorbing material, the change in refractive index when the light is polarised in x can be simplified to

$$\Delta n = -\frac{1}{2}n_0^3 \left(p_{11} \frac{\partial u_x}{\partial x} + p_{12} \frac{\partial u_z}{\partial z} \right). \quad (2.22)$$

If the incident laser light is parallel to z and polarized in y , the strain-optic coefficient p_{11} is replaced with p_{12} . Note, this result is only correct for planar sensors where the coordinate system can be chosen arbitrarily so that the strain in y -direction is constant. For fibre sensors there are additional radial terms [50, 75].

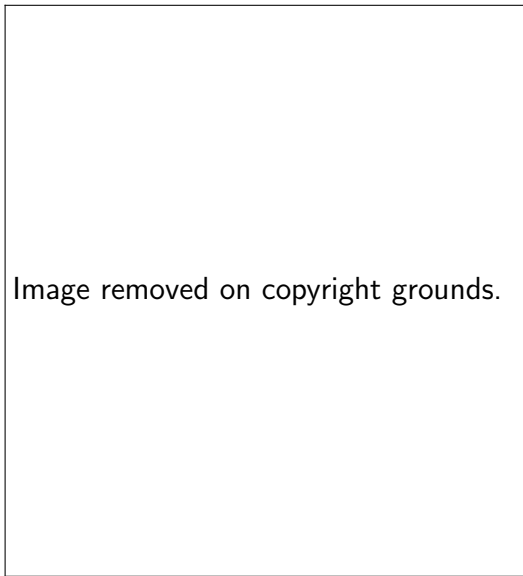


Figure 2.4: Diagram of the optical indicatrix. The principle refractive indices of a material, n_i , in x, y, z are given by the semi-axis lengths of the ellipsoid. For an isotropic material, the principle refractive indices are the same in each axis and the ellipsoid reduces to a sphere. Generally, for an electromagnetic wave travelling along the z -axis and polarised in x , the refractive index seen is n_x , and the phase speed is given by $v = c/n_x$ where c is the speed of light in a vacuum. For an electromagnetic wave travelling in an arbitrary direction with wavenumber \mathbf{k} , a plane is drawn normal to this direction at the origin of the ellipsoid. The semi-axes of the ellipse found from the intersection of the plane and the index ellipsoid give the refractive indices seen by the electromagnetic wave. This image has been reproduced from [74].

2.6 Modelling the Directional Response

One of the main aims of this thesis is to accurately model the frequency-dependent directional response. This can be found by averaging the acoustic sensitivity over the area illuminated by the interrogation laser beam weighted by the profile of the laser beam, $S(x)$ [7]. For an incident wave of unit pressure the directivity can be written

$$D(f, \theta) \propto \int_A \left(n_0 (u_z(z_2) - u_{z_2}(z_1)) + \int_{z_1}^{z_2} \Delta n \cdot dz \right) S(x, y) dA. \quad (2.23)$$

The weighting of the laser profile, S , for a circular Gaussian and top-hat beam profile are stated here, though a full derivation is included in Appendix A.

$$S = \frac{2J_1(\zeta a)}{\zeta a}, \quad (2.24)$$

and for a Gaussian profile, the weighting is

$$S = e^{-\pi\sigma^2\zeta^2/2}. \quad (2.25)$$

Here, ζ is the horizontal wavenumber, a is the beam diameter and σ is the standard deviation of the Gaussian distribution. The Gaussian distribution can be given in terms of the full width at the half maximum (FWHM) using the relation $\text{FWHM} = 2\sqrt{2\ln 2}\sigma$. The Gaussian weighting is an approximation which may only hold true if the cavity lies in the focus of the beam. However, the beam profile effects will mostly be noticeable in the form of spatial averaging features in the directivity. Since the spot diameter is very small, there are no discernible features from spatial averaging in the directional response measurements shown in Chapters 5 and 6. This means features of the directional response are dominated by the complex acoustic wave-field produced within the sensor and the results and conclusions in this thesis are still valid. Rigorous optical and elastic modelling may be needed to fully describe the transduction mechanism of the Fabry-Pérot sensor, especially for

sensors with large spot sizes.

2.7 Previous Models of the Fabry-Pérot Sensor

Beard et al. [59, 49] modelled the transduction mechanism for low finesse Fabry-Pérot interferometers consisting of thin-metallic mirrors and showed good agreement with the measured normal incidence frequency response.

Cox & Beard [7] extended the normal-incidence model of Beard [49] to calculate the frequency-dependent directional response of a soft-polymer sensor. They used a three-layer elastic model (two half spaces sandwiching the Fabry-Pérot cavity) as the mirrors were acoustically negligible. The model showed good agreement with the measurements taken. However, the measurements exhibited a low signal-to-noise ratio above 10 MHz and the features were dominated by the effect of spatial averaging due to the large interrogation beam spot-size (400 μm). This precluded the observation of features that occur at high frequencies and large angles arising from complex wave field interactions. Additionally, Cox [7] did not include the change in refractive index of the spacer materials. Cox noted the contribution from the refractive index change was significantly smaller than the contribution from the displacement change.

Weise [51] modelled the response of an alternating stack of dielectric mirrors forming a thin high-finesse Fabry-Pérot interferometer deposited on the tip of an optical fibre by combining a multilayered optical model from Wilkens [50, 76] with an acoustic finite element simulation. Weise only investigated the normal incidence response of the fiber-optic sensor. After estimating the strain-optic coefficients of mirrors in the model, they showed good agreement with the measured normal incidence frequency response. Additionally, Weise identified the acoustic phenomena which affected the frequency response, showing there were contributions from longitudinal, lateral and Rayleigh waves as well as edge diffraction effects. This had good agreement with the measured frequency response [51].

An example of the measured and modelled directional response of a soft-polymer sensor is given in Figure 2.5. This sensor is constructed similarly to the

sensor measured by Cox, however the spot diameter is $50\ \mu\text{m}$. The model used is equivalent to that used by Cox. There is poor agreement in the measured and modelled directional response. For example, a feature has been highlighted with a grey dashed line. This feature appears in a different place in the measured data. It is not known what causes these features, why they affect the directional response, and the influence that the strain-optic effect has. Understanding this disagreement was a motivation for this thesis. Additionally, the assumption that the mirrors are acoustically and optically negligible is not always reasonable when modelling Fabry-Pérot sensors with mirrors made from many alternating dielectric materials.

The next chapter begins where Cox [7] left off by introducing matrix models to model the interaction of elastic waves within the Fabry-Pérot's multilayered structure. Other introduced concepts, such as dispersion, are useful in understanding the features of the directional response and the underlying physical mechanisms.

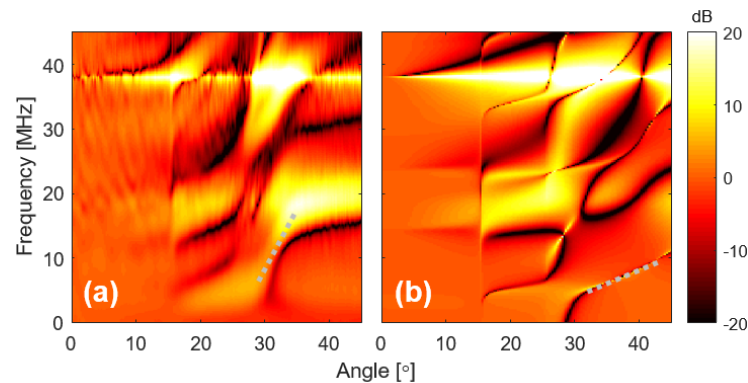


Figure 2.5: (a) Measured directional response of a soft-polymer sensor. (b) Modelled directional response of a soft-polymer sensor using an equivalent model to Cox [7].

Chapter 3

Elastic Waves in Layered Media

3.1 Introduction

An elastic material is one in which the force acting on a displaced particle is proportional to the displacement. Ignoring losses, the Fabry-Pérot interferometer has multiple elastic layers consisting of the spacer, mirrors, and substrate. When an acoustic wave is incident on the sensor, the stresses and displacements within the spacer and mirrors can be used to find the two terms governing the acoustic phase sensitivity. As discussed in Chapter 2. These are: 1) the change in refractive index of the spacer caused by a mechanical strain, and 2) the difference in vertical displacement between the two mirrors. This chapter introduces the partial-wave and global matrix method to model an acoustic wave propagating through a multilayered elastic medium.

Matrix methods, in particular the partial-wave and global matrix method, represent the stress and displacement fields as a sum of partial-waves for each material of the layered-structure. Each partial-wave represents an upward or downward travelling (quasi-)compressional or (quasi-)shear wave (bulk waves which are not purely shear or compressional but have similar characteristics are given the prefix quasi). The field properties (stresses and displacements) of every layer in the medium are represented by a field matrix multiplied by the relevant partial-wave amplitudes. By invoking boundary conditions at the interfaces of adjacent layers, the partial-wave amplitudes and field properties of the first layer can be related to

the last, and all the field matrices are assembled in the form of a ‘global’ matrix. The resulting matrix equation can be used in two different ways. Firstly, the roots of the equation can be found which give the modal solutions or dispersion curves. Secondly, a subset of partial-wave amplitudes can be defined and the remaining amplitudes solved for. This can be used to calculate the displacement and stress fields within the multi-layered structure when a plane wave is incident. This method is discussed further in Section 3.2 and 3.3.

This chapter begins by introducing the key equations needed to derive the wave equation for an infinite anisotropic elastic medium. The theory is expanded to consider the interaction of an infinite plane wave at the boundary between two elastic media. From this it is straightforward to derive the reflection and transmission coefficients. The final section of the chapter introduces the partial wave and global matrix methods for calculating the directional response of multi-layered Fabry-Pérot sensors. The propagation of elastic waves through layered media has been widely studied, and for further information the reader is directed to references [1, 77, 78, 79, 80, 81].

The journal article [82] has been reproduced and modified to form parts of this chapter, with reprint permission under CC BY.

3.2 The Elastic Wave Equation

3.2.1 Derivation of the Elastic Wave Equation

Here, the wave equation for an unbounded anisotropic elastic medium is derived. These equations are simplified for a medium with orthotropic symmetry. Figure 3.1 introduces the medium geometry (in two-dimensions), coordinate system and notation that is used throughout this chapter. The interfaces of each layer are in the (x_1, x_2) plane. The x_3 axis is orthogonal to this plane. Note, the coordinate notation has changed from Chapter 2 ($x_1 = x, x_2 = y, x_3 = z$). Each partial-wave has an amplitude B , where the superscript indicates the layer number.

An example of an isotropic material is glass, where the material properties are the same when measured from every direction. An example of a transverse-isotropic

material is a bundle of fibres, where the properties have translational symmetry axially along the fibre, and are isotropic in the plane perpendicular to this. An example of an orthotropic material is sheet metal which has been rolled between two rollers. The metal grains are stretched in the rolling direction and compressed perpendicular to this. The analysis below is restricted to model layered orthotropic materials if they are aligned such that the three orthotropic planes of symmetry are aligned with x_1, x_2, x_3 and the wave-vector of the propagating wave lies in a plane of symmetry. There are a number of reasons why the equations are simplified for this case. Firstly, it is assumed that many of the materials in the Fabry-Pérot sensor are isotropic. However, it is shown in Chapter 6, a commonly used sensor material, Parylene C, has a crystal structure which exhibits anisotropic acoustic properties. Column-like crystals of Parylene grow in the direction of (x_3) . This indicates it may have transverse-isotropic or orthotropic properties. Secondly, it has been shown that a stack of multiple, alternating isotropic layers can be represented by a single transverse-isotropic material in the case when the acoustic wavelength is much larger than the thickness of a single layer [83]. This indicates a single transverse-isotropic material may be suitable for modelling dielectric mirrors.

In an unbounded isotropic elastic medium there are two bulk wave types that exist. These are compressional waves and shear waves. In a compressional wave, the particle displacement of the medium is in the direction that the wave propagates. In a shear wave, the particle displacement is perpendicular to the direction of motion. In an unbounded anisotropic medium there are three bulk waves - quasi-compressional, quasi-shear-vertical and quasi-shear-horizontal. In an anisotropic medium the displacement in different axes are coupled, therefore a compressional type motion may also cause a shear motion. Hence, these bulk waves are termed “quasi”. The degree of the coupling is determined by the degree of anisotropy and the angle of wave propagation. For the coordinate system used here, quasi-shear-vertical waves are polarised in the (x_1, x_3) plane and quasi-shear-horizontal waves are polarised in (x_1, x_2) . Pure bulk waves may exist in an anisotropic medium under certain conditions, for example, if the direction of wave propagation is along an axis

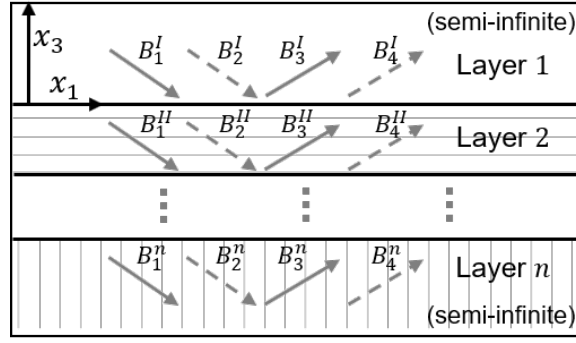


Figure 3.1: Diagram for an n -layered elastic medium. In the 2D plane there are four partial-waves with amplitude B_i^n , these represent (quasi-)compressional (solid arrows) and (quasi-)shear (dashed arrows) waves travelling upwards and downwards in each layer.

of symmetry [78]. When considering two semi-infinite media, for example, at the interface between a solid and a vacuum, guided wave modes may also exist that are the combination of both the quasi-shear and quasi-compressional waves.

For an elastic medium, Hooke's Law states that the deformation of a material is proportional to the applied stress. This is given by relating the stress tensor σ to the strain tensor ε by the stiffness tensor C . Using Einstein summation notation this is given by

$$\sigma_{ij} = C_{ijkl} \varepsilon_{kl}, \quad (3.1)$$

where $i, j, k, l \in \{1, 2, 3\}$ and the strain tensor ε is defined as

$$\varepsilon_{ij} = \frac{1}{2} \left(\frac{\partial u_i}{\partial x_j} + \frac{\partial u_j}{\partial x_i} \right), \quad (3.2)$$

where u_i is the displacement in the direction of the i axis. The stiffness tensor, C , is of rank four and has 81 individual components. However, exploiting symmetry, the stiffness tensor can be reduced to have only 21 individual coefficients to describe a fully anisotropic material [78]. Equation (3.1) can be combined with the equation of momentum conservation

$$\rho \frac{\partial^2 u_i}{\partial t^2} = \frac{\partial \sigma_{ij}}{\partial x_j}, \quad (3.3)$$

to arrive at the elastic wave equation for an unbounded, homogeneous, and lossless

anisotropic medium

$$\rho \frac{\partial^2 u_i}{\partial t^2} = \frac{1}{2} C_{ijkl} \frac{\partial}{\partial x_j} \left(\frac{\partial u_l}{\partial x_k} + \frac{\partial u_k}{\partial x_l} \right), \quad (3.4)$$

where the indices $i, j, k, l \in \{1, 2, 3\}$, x and t are the spatial and temporal variables, ρ is the total material density.

Here, the analysis is restricted to materials that are orthotropic, which reduces the number of independent coefficients in the stiffness tensor to 9. Firstly, Voigt notation is used to contract the indices of the stiffness-matrix (where $11 \rightarrow 1, 22 \rightarrow 2, 33 \rightarrow 3, 23 \rightarrow 4, 13 \rightarrow 5, 12 \rightarrow 6$). The expanded form of Hooke's Law for an orthotropic material is

$$\begin{bmatrix} \sigma_{11} \\ \sigma_{22} \\ \sigma_{33} \\ \sigma_{23} \\ \sigma_{13} \\ \sigma_{12} \end{bmatrix} = \begin{bmatrix} C_{11} & C_{12} & C_{13} & 0 & 0 & 0 \\ C_{12} & C_{22} & C_{23} & 0 & 0 & 0 \\ C_{13} & C_{23} & C_{33} & 0 & 0 & 0 \\ 0 & 0 & 0 & C_{44} & 0 & 0 \\ 0 & 0 & 0 & 0 & C_{55} & 0 \\ 0 & 0 & 0 & 0 & 0 & C_{66} \end{bmatrix} \begin{bmatrix} \epsilon_{11} \\ \epsilon_{22} \\ \epsilon_{33} \\ 2\epsilon_{23} \\ 2\epsilon_{13} \\ 2\epsilon_{12} \end{bmatrix}. \quad (3.5)$$

For $i = 1$, the momentum equation Eq. (3.3) is

$$\rho \frac{\partial^2 u_1}{\partial t^2} = \frac{\partial \sigma_{11}}{\partial x_1} + \frac{\partial \sigma_{12}}{\partial x_2} + \frac{\partial \sigma_{13}}{\partial x_3}, \quad (3.6)$$

substituting for the components of stress from Eq. (3.5) then gives

$$\begin{aligned} \rho \frac{\partial^2 u_1}{\partial t^2} &= \frac{\partial}{\partial x_1} (C_{11} \epsilon_{11} + C_{12} \epsilon_{22} + C_{13} \epsilon_{33}) \\ &\quad + \frac{\partial}{\partial x_2} (2C_{66} \epsilon_{12}) \\ &\quad + \frac{\partial}{\partial x_3} (2C_{55} \epsilon_{13}). \end{aligned} \quad (3.7)$$

Expanding the strain components using Eq. (3.2) yields

$$\begin{aligned} \rho \frac{\partial^2 u_1}{\partial t^2} &= \frac{\partial}{\partial x_1} \left(C_{11} \frac{\partial u_1}{\partial x_1} + C_{12} \frac{\partial u_2}{\partial x_2} + C_{13} \frac{\partial u_3}{\partial x_3} \right) \\ &+ \frac{\partial}{\partial x_2} \left(C_{66} \left(\frac{\partial u_1}{\partial x_2} + \frac{\partial u_2}{\partial x_1} \right) \right) \\ &+ \frac{\partial}{\partial x_3} \left(C_{55} \left(\frac{\partial u_1}{\partial x_3} + \frac{\partial u_3}{\partial x_1} \right) \right). \end{aligned} \quad (3.8)$$

Rearranging the previous equation leads to

$$\begin{aligned} \rho \frac{\partial^2 u_1}{\partial t^2} &= C_{11} \frac{\partial^2 u_1}{\partial x_1^2} + C_{66} \frac{\partial^2 u_1}{\partial x_2^2} + C_{55} \frac{\partial^2 u_1}{\partial x_3^2} \\ &+ (C_{12} + C_{66}) \frac{\partial^2 u_2}{\partial x_1 \partial x_2} \\ &+ (C_{13} + C_{55}) \frac{\partial^2 u_3}{\partial x_1 \partial x_3}. \end{aligned} \quad (3.9)$$

Here, the wave-vectors of each partial-wave are chosen to lie in the (x_1, x_3) plane. This means the displacement u_2 is constant, hence $\partial u_2 / \partial x_2 = 0$. Using a similar process for $i = 2$ and $i = 3$ the expanded form of the wave-equations for all the components are

$$\begin{aligned} \rho \frac{\partial^2 u_1}{\partial t^2} &= C_{11} \frac{\partial^2 u_1}{\partial x_1^2} + C_{55} \frac{\partial^2 u_1}{\partial x_3^2} + (C_{13} + C_{55}) \left(\frac{\partial^2 u_3}{\partial x_1 \partial x_3} \right) \\ \rho \frac{\partial^2 u_2}{\partial t^2} &= C_{66} \frac{\partial^2 u_2}{\partial x_1^2} + C_{44} \frac{\partial^2 u_2}{\partial x_3^2} \\ \rho \frac{\partial^2 u_3}{\partial t^2} &= C_{55} \frac{\partial^2 u_3}{\partial x_1^2} + C_{33} \frac{\partial^2 u_3}{\partial x_3^2} + (C_{13} + C_{55}) \left(\frac{\partial^2 u_1}{\partial x_1 \partial x_3} \right). \end{aligned} \quad (3.10)$$

In the isotropic case, the medium can be described with two material constants (λ, μ) called the Lamé parameters, or with the compressional c_L and shear c_S wave speeds. These are substituted for the stiffness coefficients as follows: $C_{11}, C_{22}, C_{33} = \lambda + 2\mu = c_L^2 \rho$, $C_{44}, C_{55}, C_{66} = \mu = c_S^2 \rho$ and $C_{12}, C_{13}, C_{23} = \lambda$.

3.2.2 Solutions to the Wave Equation

A single-frequency plane wave can be written in the form

$$u_i = A_i \exp(i(\zeta x_1 + \zeta \alpha x_3 - \omega t)), \quad (3.11)$$

where $i \in \{1, 2, 3\}$, $i = \sqrt{-1}$, $\omega = 2\pi f$ is the circular frequency, α is the ratio of the vertical and horizontal (ζ) wavenumbers, and A_i is the polarisation unit vector which describes the direction of displacement relative to the direction of wave propagation. The phase velocity v along the x_1 axis is calculated from the relation $v = \omega/\zeta$. When using this form, the real or imaginary part of the complex number should be taken to calculate the displacement of the plane wave at time t and coordinate x_3 . Taking the real part is equivalent to the incident plane wave having a cosine form, and taking the imaginary part is equivalent to the incident wave having a sinusoidal form. Taking the absolute value of the complex number gives the maximum amplitude of the displacement. When adding or subtracting multiple complex displacement fields, for example, to calculate the difference in vertical mirror displacement, care should be taken to manipulate the values in complex form before taking the real part, imaginary part, or absolute value.

3.2.3 Christoffel Equation

For an isotropic material, the horizontal ζ and vertical $\zeta \alpha$ wavenumbers are a function of the frequency, angle of propagation, and the compressional or shear speed. The horizontal wavenumber ζ is the same for every layer and bulk wave type as a result of Snell's law [77]. By definition, the shear and compressional speed is constant for every angle of propagation for an isotropic elastic medium. This makes it relatively straightforward to write down the wave-vector components. However, this is not the case for anisotropic materials as the quasi-compressional and quasi-shear speed is angle dependent. To find the ratio of the wave-vector components α and polarisations A_i of an anisotropic medium, the Christoffel equation needs to be used.

Firstly, the plane wave solution for the wave equation Eq. (3.11) is substituted

into Eq. (3.10)

$$\begin{aligned}
-\zeta^2 \rho v^2 A_1 &= -\zeta^2 A_1 C_{11} - \zeta^2 \alpha^2 A_1 C_{55} - (C_{13} + C_{55}) \zeta^2 \alpha A_3 \\
0 &= (C_{11} - \rho v^2 + C_{55} \alpha^2) A_1 + (C_{13} + C_{55}) \alpha A_3 \\
-\zeta^2 \rho v^2 A_2 &= -\zeta^2 A_2 C_{66} - \zeta^2 \alpha^2 A_2 C_{44} \\
0 &= (C_{66} - \rho v^2 + C_{44} \alpha^2) A_2 \\
-\zeta^2 \rho v^2 A_3 &= -\zeta^2 A_3 C_{55} - \zeta^2 \alpha^2 A_3 C_{33} - (C_{13} + C_{55}) \zeta^2 \alpha A_1 \\
0 &= (C_{55} - \rho v^2 + C_{33} \alpha^2) A_3 + (C_{13} + C_{55}) \alpha A_1
\end{aligned} \tag{3.12}$$

where the substitution $\omega^2 = \zeta^2 v^2$ has been used on the left hand side to simplify the equations. These equations can be rearranged into the Christoffel equation

$$\begin{bmatrix} \Gamma_{11} & 0 & \Gamma_{13} \\ 0 & \Gamma_{22} & 0 \\ \Gamma_{31} & 0 & \Gamma_{33} \end{bmatrix} \begin{bmatrix} A_1 \\ A_2 \\ A_3 \end{bmatrix} = 0, \tag{3.13}$$

where the components of the Christoffel matrix (Γ) are

$$\begin{aligned}
\Gamma_{11} &= (C_{11} - \rho v^2 + C_{55} \alpha^2) & \Gamma_{22} &= (C_{66} - \rho v^2 + C_{44} \alpha^2) \\
\Gamma_{33} &= (C_{55} - \rho v^2 + C_{33} \alpha^2) & \Gamma_{13} &= \Gamma_{31} = (C_{13} + C_{55}) \alpha \\
\Gamma_{12} &= \Gamma_{21} = \Gamma_{32} = \Gamma_{23} = 0.
\end{aligned}$$

Solving Eq. (3.13) admits three solutions for α^2 and therefore 6 solutions for α . In the general case, these solutions correspond to upward or downward travelling quasi-compressional or quasi-shear waves. From here, the notation α_q , where $q \in \{1, 2, \dots, 6\}$, is used to indicate each solution. It can be seen from Eq. (3.13) that the plane wave component A_2 is only dependent on Γ_{22} , hence displacement occurring in the (x_1, x_3) plane is independent of displacement in x_2 . This only occurs as a result of the imposed restrictions on the material symmetry and alignment of the material axes with the coordinate system used. Four solutions ($q = 1, 2, 3, 4$) of α_q

Eq. (3.13) can be found when

$$\det \begin{vmatrix} \Gamma_{11} & \Gamma_{13} \\ \Gamma_{13} & \Gamma_{33} \end{vmatrix} = 0. \quad (3.14)$$

These describe upwards and downward travelling quasi-shear-vertical (qSV) and quasi-longitudinal (qL) waves with the displacement restricted to the (x_1, x_3) plane. This leads to a polynomial equation in the form

$$a\alpha^4 + b\alpha^2 + c = 0, \quad (3.15)$$

where the coefficients are given by the expressions

$$a = C_{33}C_{55} \quad (3.16)$$

$$b = (C_{55} - \rho v^2)C_{55} + (C_{11} - \rho v^2)C_{33} \quad (3.17)$$

$$- (C_{13} + C_{55})^2 \quad (3.18)$$

$$c = (C_{11} - \rho v^2)(C_{55} - \rho v^2). \quad (3.19)$$

The solutions to α^2 are found using the quadratic equation

$$\alpha^2 = \frac{-b \pm \sqrt{b^2 - 4ac}}{2a}. \quad (3.20)$$

The positive solutions of the quadratic equation correspond to (quasi-)compressional waves and the negative solutions correspond to the (quasi-)shear waves. The order is arbitrary, however, in the following equations, $\alpha_1 = -\alpha_3$ and $\alpha_2 = -\alpha_4$, where α_1 and α_3 are downward and upward travelling (quasi-)compressional waves and α_2 and α_4 are downward and upward travelling (quasi-)shear waves. This order is indicated on Figure 3.1. The remaining two solutions ($q = 5, 6$) are found from $\Gamma_{22} = 0$, and correspond to upward- and downward- travelling quasi-shear-horizontal (qSV) waves, hence,

$$\alpha^2 = \frac{-C_{66} + \rho v^2}{C_{44}}. \quad (3.21)$$

The notation A_{iq} will now be used to indicate the polarisation vector for each solution q . The displacement field can now be written as a sum of the partial-wave components

$$u_i = \sum_{q=1}^4 A_{iq} B_q \exp(i(\zeta x_1 + \zeta \alpha_q x_3 - \omega t)), \quad (3.22)$$

where $i \in \{1, 3\}$ and B_q is the amplitude of each partial-wave. For a multi-layered medium, the Christoffel equation Eq. (3.13) is solved independently for every layer to calculate the polarisation vector and wave-vector of each partial-wave. However, the amplitude B_q of each partial-wave is solved by invoking the boundary conditions at the interfaces of adjacent layers. This is discussed in Section 3.3.

3.3 Partial-Wave and Global Matrix Method

3.3.1 Overview

Each partial-wave represents the superposition of waves that are multiply reflected or transmitted at the interfaces between each layer in a steady-state. The polarisation vector and wave-vector of each of these partial-waves can be found from the Christoffel Equation as described in Section 3.2.3. The degree of reflection and transmission depends on the boundary conditions at the interfaces and material properties of each layer. The coupled equations that arise from the boundary conditions can be combined into a ‘global-matrix’ which allows them to be solved simultaneously. This global matrix approach can be used to tackle various problems in elastic wave propagation. For example, the singularities of the global matrix give the dispersion curves, and by specifying an incident wave amplitude, the resulting wave-field throughout the structure can be calculated. More detailed descriptions of the partial-wave and global-matrix method can be found in [84, 78, 85, 77, 86, 79, 87, 88].

3.3.2 Boundary Conditions and Partial-Wave Amplitudes

As mentioned previously, the wave-vector of the plane waves are constrained to a plane of symmetry of the orthotropic or transverse-isotropic material reducing the analysis to two dimensions, (x_1, x_3) . From Eq.(3.2), Eq.(3.5) and Eq.(3.22) the normal and transverse displacement and stress describing (quasi-)longitudinal and (quasi-)shear-vertical waves for a single layer is written in the form

$$\begin{bmatrix} u_1 \\ u_3 \\ \sigma_{33} \\ \sigma_{13} \end{bmatrix} = \begin{bmatrix} A_{11} & A_{12} & A_{13} & A_{14} \\ A_{31} & A_{32} & A_{33} & A_{34} \\ D_{11} & D_{12} & D_{13} & D_{14} \\ D_{21} & D_{22} & D_{23} & D_{24} \end{bmatrix} \begin{bmatrix} e_1 \\ e_2 \\ e_3 \\ e_4 \end{bmatrix} = \begin{bmatrix} B_1 \\ B_2 \\ B_3 \\ B_4 \end{bmatrix}, \quad (3.23)$$

where

$$D_{1q} = (C_{13}A_{1q} + C_{33}\alpha_q A_{3q})(i\zeta) \quad D_{2q} = C_{55}(\alpha_q A_{1q} + A_{3q})(i\zeta),$$

$$e_q = \exp(i(\zeta x_1 + \zeta \alpha_q x_3 - \omega t)).$$

Only the first four solutions of α_q are needed as the motion in (x_1, x_3) is decoupled from (x_2) . The left hand vector of Eqs. (3.23) contains the components of the displacement and stress, and the right hand vector contains the amplitude of the partial-wave components. The product of the matrices in Eq. (3.23) can be written as a field matrix \mathbf{F} ,

$$\mathbf{F} = \begin{bmatrix} A_{11} & A_{12} & A_{13} & A_{14} \\ A_{31} & A_{32} & A_{33} & A_{34} \\ D_{11} & D_{12} & D_{13} & D_{14} \\ D_{21} & D_{22} & D_{23} & D_{24} \end{bmatrix} \begin{bmatrix} e_1 \\ e_2 \\ e_3 \\ e_4 \end{bmatrix}. \quad (3.24)$$

At an interface $x_3 = d$ between material layers in welded contact, the normal and transverse stress and displacement must be continuous across the interface. Therefore, the product of the field matrix and partial-wave amplitudes at the interface of one layer is set equal to the field matrix and wave amplitudes of the adjacent layer. For example

$$\mathbf{F}_1^I \mathbf{B}^I = \mathbf{F}_1^{II} \mathbf{B}^{II}, \quad (3.25)$$

where \mathbf{F}_N^n is the 4×4 field matrix for layer n at interface N and \mathbf{B}^n is a 4×1 vector of partial-wave amplitudes for layer n . For clarity a diagram has been included in Figure 3.2. This process is repeated for every interface of the layered medium. For n -layers, there are $4(n-1)$ boundary conditions and $4n$ wave amplitudes which can be arranged into a global matrix. This assumes the first and last layers are semi-infinite in thickness and every layer is elastic. For a medium consisting of n layers, the global matrix equation is written

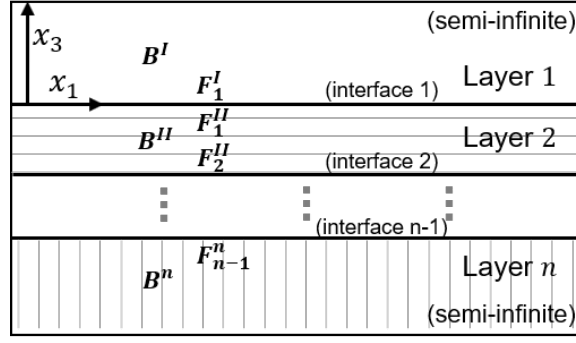


Figure 3.2: Field matrix and partial-wave amplitude vector labelling for an n -layered elastic medium. Here, \mathbf{F}_N^n is the 4×4 field matrix for layer n at interface N and \mathbf{B}^n is a 4×1 vector of partial-wave amplitudes for layer n .

$$\begin{bmatrix} \mathbf{F}_1^I & -\mathbf{F}_1^{II} & & & & \\ & \mathbf{F}_2^{II} & -\mathbf{F}_2^{III} & & & \\ & & \ddots & \ddots & & \\ & & & \mathbf{F}_{n-1}^{n-1} & -\mathbf{F}_{n-1}^n & \\ & & & & & \end{bmatrix} \begin{bmatrix} \mathbf{B}^I \\ \vdots \\ \mathbf{B}^n \end{bmatrix} = 0. \quad (3.26)$$

For clarity, it is helpful to write the problem for a specific case. For example, for three layers the global matrix is

$$\begin{bmatrix} \mathbf{F}_1^I & -\mathbf{F}_1^{II} & & \\ & \mathbf{F}_2^{II} & -\mathbf{F}_2^{III} & \\ & & & \end{bmatrix} \begin{bmatrix} \mathbf{B}^I \\ \mathbf{B}^{II} \\ \mathbf{B}^{III} \end{bmatrix} = 0. \quad (3.27)$$

By assigning values to four of the partial-wave amplitudes, Eq.(3.27) (and Eq.(3.26)), can be rearranged and solved for the remaining partial-wave amplitudes. For example, if a compressional wave in the first medium is incident on the layered-structure, the downward-travelling partial-wave amplitude relating to shear (B_2^I , Figure 3.1) in the first layer and upward-travelling partial-wave amplitudes relating to compressional (B_3^n) and shear (B_4^n) waves in the last (n th) layer are set to zero. Finally, the downward-travelling partial-wave amplitude relating to a compressional wave in the first layer is set to $B_1^I = 1$ (the calculated outputs can later be scaled if desired). In this case, the solved amplitudes describe the solution for an incident single-frequency plane-wave at an angle θ or wavenumber

ζ and frequency f . Separating the known wave amplitudes from the unknown wave amplitudes, Eq. (3.27) can be written as

$$\begin{bmatrix} \mathbf{F}_1^{\text{I}+} & -\mathbf{F}_1^{\text{II}} \\ & \mathbf{F}_2^{\text{II}} & -\mathbf{F}_2^{\text{III}-} \end{bmatrix} \begin{bmatrix} \mathbf{B}^{\text{I}+} \\ \mathbf{B}^{\text{II}} \\ \mathbf{B}^{\text{III}-} \end{bmatrix} = \begin{bmatrix} -\mathbf{F}_1^{\text{I}-} & \\ & \mathbf{F}_2^{\text{III}+} \end{bmatrix} \begin{bmatrix} \mathbf{B}^{\text{I}-} \\ \\ \mathbf{B}^{\text{III}+} \end{bmatrix}. \quad (3.28)$$

Here, + and – superscripts indicate the upwards and downwards travelling partial-wave amplitudes and their respective columns in the field matrices. The global matrix for systems with other numbers of layers follows analogously.

For clarity, an expanded form of Eq. (3.28) is given in Eq. (3.29). $\mathbf{F}_1^{\text{I}+}$ is the third and fourth columns of \mathbf{F}_1^{I} , and $\mathbf{B}^{\text{I}+}$ is the third and fourth elements of \mathbf{B}^{I} . In the example described above, the first element of $\mathbf{B}^{\text{I}-}$ is 1 and all the elements of $\mathbf{B}^{\text{III}+}$ and the second element of $\mathbf{B}^{\text{I}-}$ are 0.

Once the unknown wave-amplitudes for each layer are found, Eq. (3.23) can be used to find the displacement and stress anywhere in the layered structure. Additionally, for a two layered medium, normalising the wave-amplitudes by the incident wave amplitude gives the displacement reflection and transmission coefficients. This is compared to analytical solutions from the literature in Section 4.4.

Alternatively, the dispersion curves can be extracted from the model by setting the incident wave-amplitudes of the layered structure to zero and finding the frequency-wavenumber pairs in which the resulting left-hand-side matrix of Eq. (3.28) becomes singular. The algorithm used is described further in Chapter 4

3.3.3 Shear-Horizontal Waves

For the chosen coordinate system and material symmetry, shear-horizontal waves propagate independently of (quasi-)shear-vertical and (quasi-)compressional waves. Motion in x_2 decouples from (x_1, x_3) , which means there is no mode conversion and shear-horizontal waves only excite shear-horizontal waves at an interface [80]. The displacement in x_2 is written as a sum of partial wave components

$$u_2 = \sum_{q=5}^6 A_{iq} B_q \exp(i(\zeta x_1 + \zeta \alpha_q x_3 - \omega t)), \quad (3.30)$$

where solutions 5 and 6 of q correspond to shear-horizontal waves. From Eq. (3.2), Eq.(3.5) the displacement and shear stress is

$$\begin{bmatrix} u_2 \\ \sigma_{23} \end{bmatrix} = \begin{bmatrix} A_{25} & A_{26} \\ D_{35} & D_{36} \end{bmatrix} \begin{bmatrix} e_5 \\ e_6 \end{bmatrix} \begin{bmatrix} B_5 \\ B_6 \end{bmatrix}, \quad (3.31)$$

where

$$D_{3q} = C_{44} \alpha_q A_{2q}(i\zeta).$$

3.3.4 Potential Method

In the isotropic case, the method of potentials can also be used to model elastic wave propagation in multilayered materials [79, 84, 7]. In this method, the elastic wave equation can be split into two separate wave equations via the Helmholtz decomposition which states that a displacement field is the sum of the divergence of a scalar potential field and curl of a vector potential field ($\mathbf{u} = \nabla\phi + \nabla \times \boldsymbol{\psi}$). The first term $\nabla\phi$ relates to a dilation of the material, where the shape is constant but the volume changes. The second term $\nabla \times \boldsymbol{\psi}$ refers to a shear distortion of the material, where the material changes shape but the volume is constant. Hence, the first term corresponds to the propagation of compressional waves and the second to the propagation of shear waves.

Both the partial-wave and potential method were implemented during the course of this PhD. However, only the partial-wave method is discussed here. This

is because the partial-wave method is more general and reduces to the potential method in the isotropic case. For reference, the potential-amplitudes and partial-wave amplitudes are related by the following relations, where the superscript p indicates the potential method,

$$B_1^p = \frac{B_1}{ik_x}, \quad B_2^p = -\frac{B_2}{ik_t}, \quad (3.32)$$

$$B_3^p = \frac{B_3}{ik_x}, \quad B_4^p = \frac{B_4}{ik_t}. \quad (3.33)$$

For the partial-wave method in the isotropic case $k_x = \zeta$ indicates the horizontal wavenumber, and $k_t = \zeta \alpha_2 = -\zeta \alpha_4$ is the shear-vertical wavenumber.

3.3.5 Attenuation

The model from the previous section is capable of describing the propagation of elastic waves through a multilayered structure. In practice, as a wave travels along a layer, it may leak energy into the adjacent medium and the wave amplitude decays with distance. To see the effect of this behaviour, an attenuation term is needed. At this point, the introduction of a complex wavenumber allows for a viscoelastic description [84, 89].

The real part of the complex wavenumber describes the elastic propagation of the wave and the imaginary part describes an attenuation. This representation describes bulk waves whose attenuation is linearly increasing with frequency [84]. Note, it is also possible to include a complex frequency instead of wavenumber [90]. Here, just the isotropic case is considered. The plane wave solutions, Eq. (3.11), have a similar expression, however, the wavenumber k is now complex and can be written in the form

$$u_i \propto e^{i(k_i, \text{imag} x_i - \omega t)} e^{-k_i, \text{real} x_i}. \quad (3.34)$$

The first exponential term describes the harmonic propagation of the wave, and the second exponential term describes the exponential decay of the wave with distance [84]. The compressional c_L and shear c_S speeds of the media are defined as complex

values [84],

$$c'_{L,S} = \frac{c_{L,S}}{1 + iA/2\pi}. \quad (3.35)$$

Here, the attenuation is given by A in Nepers per wavelength, therefore a wave that has a unit amplitude will decay by e^{-A} every wavelength travelled.

3.4 Dispersion and Modal Solutions

3.4.1 Introduction

The previous sections describe the partial-wave method for modelling elastic wave propagation in layered media. This section investigates how these models can be used to gain a deeper insight into the underlying physical mechanisms of the Fabry-Pérot sensor and other layered media.

At interfaces between two different media and in embedded layers, there may exist wave modes that are a combination of compressional and shear waves and propagate independently of the bulk waves. These are termed guided wave modes. The wave velocity of guided waves often varies with frequency, a phenomenon called dispersion. A dispersion curve is thus a graph of how the speed of a guided wave varies with frequency. This section briefly describes the common guided waves which may appear in the Fabry-Pérot sensor and how they may be calculated from the matrix formulation described previously. For more information about guided waves, the reader is directed to references [1, 79, 91, 92, 93, 94, 95, 96, 97, 98].

Evanescent Wave

A plane wave incident on the interface of a half-space at the critical angle is transmitted parallel to the interface and is reflected normal to the interface. The transmitted wave has an exponential decay away from the interface, this is termed an evanescent or inhomogeneous wave. These manifest in the model as the partial-waves having complex wavenumbers.

Rayleigh Wave

A free wave is one which propagates indefinitely along a medium without leaking energy into the adjoining half spaces [91]. A Rayleigh wave is a type of free wave which propagates at the interface between a vacuum and a solid half space [96]. The Rayleigh wave has a maximum displacement at the interface and the displacement decays exponentially moving perpendicularly into the solid half-space away from boundary. Rayleigh waves have a characteristic elliptical motion.

Lamb Wave

In 1917, Lamb extended the theory derived by Rayleigh considering the problem of elastic waves in a medium bound by two parallel planes [97]. It was found that there exists an infinite number of solutions of Lamb waves which are higher order modes of two fundamental shapes: a symmetric mode, and an anti-symmetric mode. Symmetric or ‘compressional’ modes are distinguishable as being symmetric about the centre-line of the medium. The distance between the parallel planes of the medium are compressed or expanded resulting in an hour-glass shape. Anti-symmetric or ‘flexural’ modes are distinguishable as the mode is anti-symmetric about the centre-line of the medium. The distance between the parallel planes remain constant resulting in a rippled shape. An illustrative demonstration of the mode shapes can be seen in Figure 3.3.

Leaky Waves

If the guided waves lose some energy to the surrounding then they are termed “leaky”. In the previous examples, if the medium or solid half space is surrounded by a fluid instead of a vacuum then some energy is transferred into the fluid. These guided waves are then called “leaky-Rayleigh” or “leaky-Lamb” waves [91]. However, for large impedance differences, for example, a metal or glass plate in water, there is not a significant effect on the Lamb or Rayleigh modes.

Interface Waves

Stoneley [98] described a wave travelling along the interface between two elastic solid media. For special combinations of material properties, a free Stoneley wave

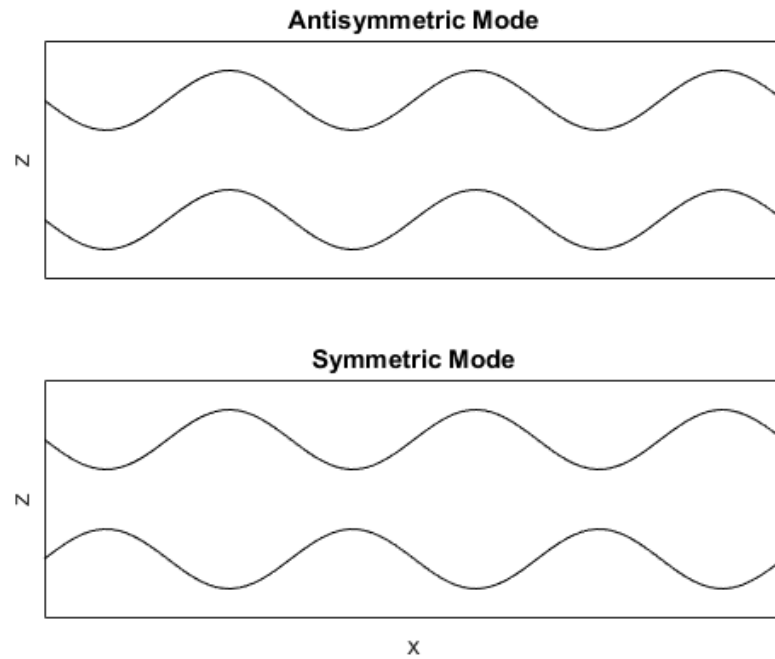


Figure 3.3: Illustrative example of anti-symmetric and symmetric mode shapes.

may exist. Otherwise, these guided waves are “leaky” or may be referred to simply as interface waves. If the interface is between a liquid/vacuum and a solid then this may be referred to as a surface wave.

3.4.2 Modal Solutions

By choosing the appropriate number of layers and material properties, the different wave modes described above can be found using the partial-wave method and the approach described here. In Section 3.3, the equations of stress and strain are assembled into a matrix equation which takes the form

$$\mathbf{S}B = b, \quad (3.36)$$

where \mathbf{S} is the system matrix of equations, B is a vector of partial-wave amplitudes, and b is a vector of known wave amplitudes (see Eq. (3.28)). Dispersion curves can be generated by finding non-trivial pairs of frequency and wavenumber where

$$\mathbf{S}B = 0. \quad (3.37)$$

At these points, a solution exists for free waves propagating along a layer without any incident wave. Solutions to Eq. (3.37) exist when the complex determinant of the system is singular. However, the presence of a singular determinant does not necessarily indicate the presence of a guided wave mode. In the instance when the component of the wavenumber parallel to the interface is equal to the wavenumber of any of the bulk waves of the system, the matrix has multiple columns which are identical, hence the determinant becomes singular [84]. The implementation of the numerical method to find the modal solutions is described in the next chapter.

3.5 Summary

The partial-wave method presented in this section can describe elastic wave propagation in isotropic, transverse-isotropic, and orthotropic media. The matrix formulation allows the partial-wave amplitudes of the first layer to be related to the last. The wave amplitudes can be used to calculate the stresses and displacements at any coordinate within the sensor and consequently calculate the directional response. Reflection and transmission coefficients and dispersion analysis have been presented as tools to understand the underlying physical mechanisms within the sensor and are discussed further in Chapter 4.

Chapter 4

ElasticMatrix: A MATLAB Toolbox for Anisotropic Elastic-Wave Propagation in Multilayered Media

4.1 Introduction

The previous chapter introduced the partial-wave method for modelling elastic wave propagation in layered media and the directional response of the Fabry-Pérot sensor. Additionally, dispersion curves were introduced, which can be used to analyse the wave-phenomena which give rise to the complex directional response.

The partial-wave method and other matrix models of wave propagation in multi-layered elastic solids have had a significant contribution to research areas such as acoustics, geophysics and electromagnetics. A few examples include: structural health monitoring [99], characterisation of interface bonding [100], detection of debonding in joints [101], measuring material properties [84], designing composite layered structures [78], mode sorting of guided waves [102], the physical interpretation of guided wave structures [103], the investigation of anisotropy on amplitude-versus-offset synthetic modelling [104], reflection and transmission of plane waves [105], elastography of layered soft tissues [106], and ice detection on wind turbines [107].

Despite its usefulness, there are few available implementations of the partial-

wave method. Additionally, coding the required matrix formation, inversion, and analysis for general multi-layered systems is non-trivial and time-consuming. The current state-of-the-art implementation is Disperse [108]. This software has been in development since 1990 and is primarily focused on calculating the dispersion solutions for multi-layered structures. The Disperse software was originally based on the partial-wave and potential method, however, it is currently being updated to use the spectral collocation method (SCM) [108, 109, 110, 111, 112]. The main limitation with Disperse is that it is closed-source. For this reason it is not easily adaptable for applications that are not dispersion analysis, for example, extracting reflection coefficients or slowness profiles. Other open source code modelling the partial-wave method include LAMB [113] (however this is limited to modelling only an isotropic plate) and ANIVEC [114] (however this code is not easily available).

In this chapter, a new open-source toolbox called `ElasticMatrix` is introduced which uses the partial-wave method for multi-layered structures with an arbitrary number of isotropic, transverse-isotropic and orthotropic layers. Where possible, it is validated against existing literature, analytic examples, and Disperse. Additionally, `ElasticMatrix` has been made publicly available with detailed documentation so that it is both easy to use and extend.

The partial-wave method was chosen over the SCM for a number of reasons. Firstly, the primary aim of the thesis is to model the directional response of the Fabry-Pérot sensor which requires modelling elastic wave propagation in multilayered media. For this use-case, the partial-wave method is suitable as it is analytic, more accurate, and faster than the SCM. Additionally, as the partial-wave method is well established it can be easily adopted by researchers who are aware of this method and easily adapted to model coupled systems and complex materials such as piezo-electric materials [78]. A secondary aim of this thesis is to improve the understanding of the underlying physical mechanism of the Fabry-Pérot sensor. One method to do this is to calculate the dispersion curves of the elastic structure. For simple layered structures the partial-wave method is robust and proven at

its ability to trace the correct dispersion curves. Hence, the partial-wave method is still a suitable choice for this purpose. However, the SCM casts the layered system as an eigenvalue matrix problem, where the eigenvalues give the dispersion solutions. This formulation makes the SCM generally superior at calculating dispersion curves. For simple layered structures the performance of both methods are comparable. Where the SCM really becomes advantageous is when calculating dispersion curves for strongly anisotropic and strongly absorbing materials, in these cases the partial-wave method struggles. In the future if the calculation of dispersion curves becomes the primary use-case of the toolbox it would be sensible to adapt the dispersion curve algorithm to use the SCM or a similar method. However, the remainder of the toolbox functionalities are useful as is, for example calculating reflection/transmission coefficients, slowness profiles, displacement fields and the directivity of the Fabry-Pérot sensor.

This chapter has three parts. Section 4.2 discusses the implementation of key algorithms in the software, such as how the dispersion curves are traced. Section 4.3 describes the `ElasticMatrix` software with example code of how to use different methods. Finally, Section 4.4 compares the results from the model with examples from analytical derivations and literature.

The journal article [82] has been reproduced and modified to form parts of this chapter, with reprint permission under CC BY.

4.2 Implementation

4.2.1 Field Matrices and Global Matrix

To construct the global matrix given in Eq. (3.27), a field matrix \mathbf{F}^n must be calculated for the interfaces of each layer n . To improve the conditioning of each field matrix, rows relating to stress are scaled by $i\zeta \times 10^9$. The stress equations have a common factor of $i\zeta$ (see Eq. (3.23)) and most stiffness coefficients are on the order of GPa. The global matrix is constructed by calculating the 4×4 field matrices above and below each interface and arranging them into a single matrix as given in Eq. (3.27) and Eq. (3.26). This leads to a rectangular matrix which has

$4n$ columns and $4(n - 1)$ rows. Additionally there are $4n$ partial-wave amplitudes. Two partial-wave amplitudes are defined in the first layer and two in the last, and the global-matrix in Eq. (3.27) is rearranged to be square as shown in Eq. (3.29). The resulting equation is solved using the `mldivide` function in MATLAB. This function solves a system of linear equations using the fastest algorithm based on the matrix structure. However, the global-matrix becomes singular at values of ζ and ω on or close-to dispersion curve solutions. In practice, it is unlikely that the exact dispersion solution will be chosen as a point of calculation.

4.2.2 Dispersion Curve Algorithm

Dispersion curves are used to gain an understanding of the underlying physics in the Fabry-Pérot sensor. The computation of dispersion curves in `ElasticMatrix` is similar to the algorithm described by Lowe [84] and is described here. As introduced in Section 3.4.2, the dispersion curves can be generated by finding non-trivial pairs of frequency and wavenumber where

$$S(f, \zeta)B = 0. \quad (4.1)$$

Here, S is the system matrix for a given frequency f and horizontal wavenumber ζ and B is a vector of partial-wave amplitudes. This corresponds to solutions of frequency and wavenumber where $\det|S(f, \zeta)| = 0$. The computation of dispersion curves is performed in the frequency-wavenumber domain as the curves are close to straight lines. After calculation, the curves can be transformed in terms of frequency-phasespeed or frequency-angle. The main steps in the dispersion curve algorithm are as follows:

(1) Firstly a range of frequencies f are chosen (this is a user chosen parameter in the `ElasticMatrix` toolbox described in Section 4.3). The range of wavenumbers ζ can be automatically generated by using the maximum frequency and finding the lowest bulk wave speed c_{min} in the material layers. The formula $\zeta_{max} = 2\pi f_{max} / (c_{min} * 0.8)$ is used to find the maximum value of ζ . This ensures the curves are traced to the maximum of the frequency range. The value of 0.8 is

used to ensure Rayleigh waves are captured. These typically have a phase velocity 85% to 95% of the shear wave speed.

(2) The starting points of each dispersion curve are found by fixing one parameter and sweeping over the other. For example, the lowest wavenumber is chosen and the determinant of the system matrix is calculated over the entire range of frequencies. Close to the dispersion solutions, the system matrix becomes singular leading to minima in the determinant. Figure 4.1 (a) shows the fully traced dispersion curves in wavenumber and frequency. The dashed blue lines indicates where the frequency and wavenumber sweep are taken. The determinant of the system matrix along the sweeps can be seen in Figure 4.1 (b) and (c). The minima in the determinant indicate starting points of the dispersion curves. The number of starting

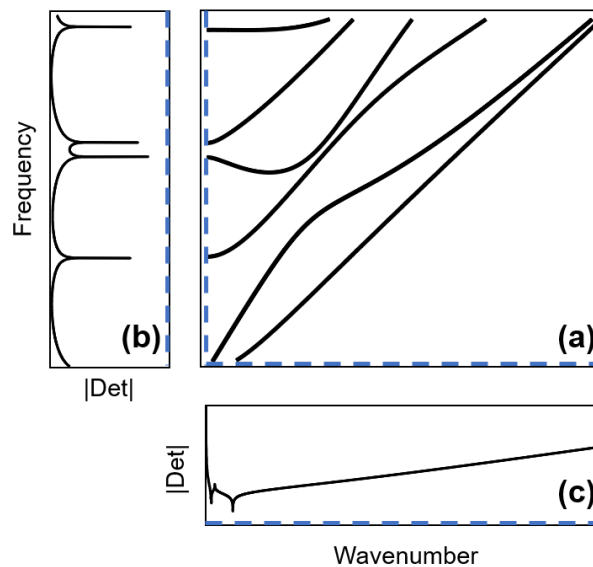


Figure 4.1: (a) Dispersion curves in wavenumber and frequency. The dotted blue lines indicate where the initial starting points sweeps are taken. (b) The determinant across the frequency sweep. Four minima can be seen corresponding to four dispersion curve starting points. (c) The determinant across the wavenumber sweep. Two minima can be seen corresponding to two dispersion curve starting points.

points depends on the thickness of the plate and the frequency. For example, along the frequency sweep, there are four starting points for a 1 mm titanium plate within the first 5 MHz, and there are four starting points for a 0.1 mm titanium plate within the first 50 MHz. Hence, the starting points for the product of the plate thickness-

frequency product are constant. The frequency intervals Δf are chosen based on the formula

$$\Delta f = \frac{f_{max}}{\frac{f_{max}d_T}{1000}N_f} = \frac{1000}{d_T N_f}. \quad (4.2)$$

Here, f_{max} is the maximum frequency, d_T is the total thickness of the finite layers and N_f is the number of sample points per frequency-thickness (MHz-mm) product (hence the origin of the factor of 1000). This formula scales Δf relative to the thickness of d_T so that the number of points per frequency-thickness product is constant. A graph of the number of starting points found in the frequency sweep versus N_f has been plotted in Figure 4.2 (a) for three different materials covering a range of sound speeds for Teflon, perspex and titanium. Note, the lower the sound speed the more starting points there are. All starting points are found at approximately $N_f = 100$. For this implementation $N_f = 200$. This improves the accuracy at no significant computational cost. A low value of N_f misses starting points as there is not enough sampling to find all the minima in the determinant. This is shown in Figure 4.2 (c) and (d). A similar metric is used to choose the $\Delta \zeta$ step size for the wavenumber sweep,

$$\Delta \zeta = \frac{\zeta_{max}}{\zeta_{max}d_T N_\zeta} = \frac{1}{d_T N_\zeta}. \quad (4.3)$$

Interestingly, low values of N_ζ over-estimate the number of starting points, as shown in Figure 4.2 (b). However, all three curves converge after $N_\zeta > 200$. Here N_ζ is chosen as 300. The minima are found by taking the gradient of the sweep and looking for crossing points of the x-axis when the gradient changes from positive to negative, as shown in Figure 4.2. These are used as the coarse starting points in the dispersion curve algorithm.

(3) A more precise frequency and wavenumber of the dispersive solution is found using a bisection algorithm. For every coarse starting point, the wavenumber is fixed and a minimisation function is used to find the exact frequency of the dispersion curve using the determinant as a cost metric. `ElasticMatrix` makes use of MATLAB's `fminbnd()` function to constrain the minimisation between $\pm \Delta f$. The tolerance between the previous and current value is set to stop at 1×10^{-4} ,

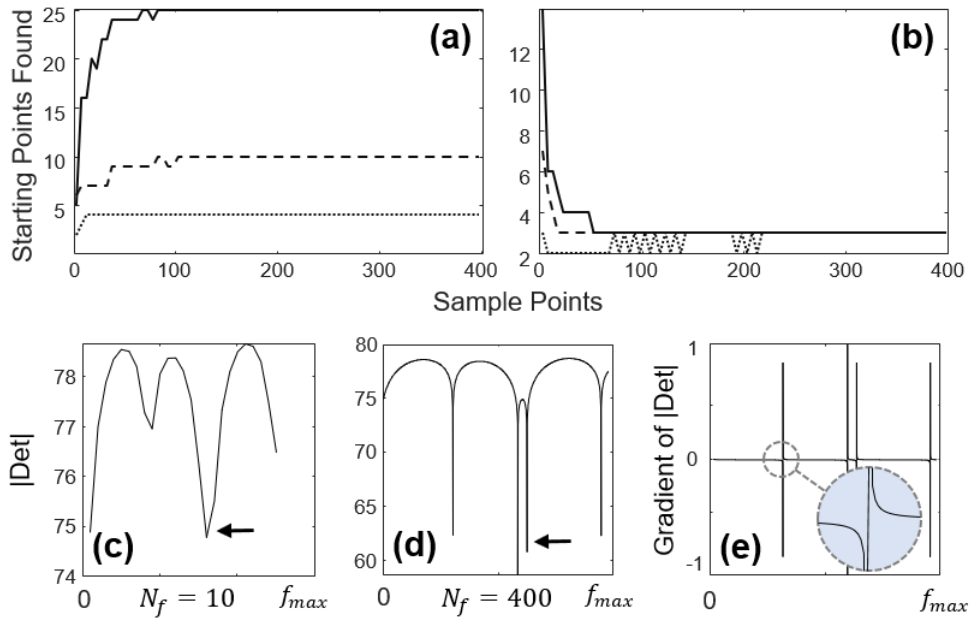


Figure 4.2: (a) Number of starting points found versus number of points per N_f for the frequency-sweep. The solid line is a Teflon plate, the dashed line is a perspex plate and the dotted line is a titanium plate. (b) Number of starting points found versus number of points per N_f for the wavenumber-sweep. (c) Low N_f for the frequency sweep. (d) High N_f for the frequency sweep. The arrow shows that there are two starting points which can only be found if N_f is high enough. (e) Gradient of the frequency sweep. Minima are found where the gradient changes from negative to positive.

which is sufficient accuracy in practice. Testing the algorithm at different tolerances did not have a significant impact on compute time. These refined values are used as the starting points for each dispersion curve where each starting point is used to trace a different curve.

(4) The algorithm starts tracing the curves from the lowest wavenumber value across the range of frequencies. The second point on the dispersion curve is found by increasing the fixed value of wavenumber ($+\Delta k$) and repeating the method from the previous step.

(5) The algorithm uses linear interpolation between the first two points to estimate the location of the third, fourth and fifth points on the dispersion curve. Here, `interp1()` is used with the 'linear' and 'extrap' flags. For each estimated point, a simple gradient descent algorithm moves the estimated point to the closest minimum in the determinant. This is illustrated in Figure 4.3. In Figure 4.3

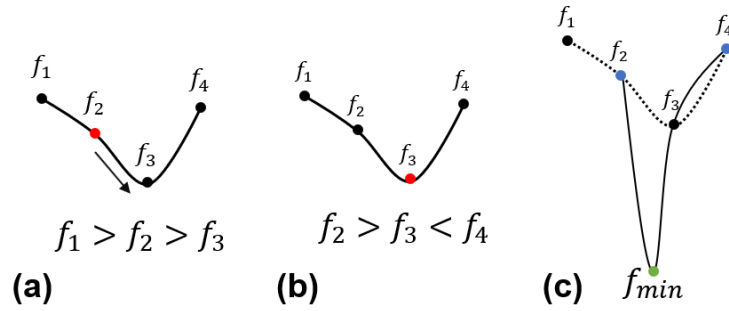


Figure 4.3: (a) The neighbouring points of the predicted point (in red) are evaluated. (b) If the predicted point is not the lowest, the next point along is chosen and the points either side are evaluated. (c) If the current point is the lowest, the two points either side (in blue) are used as bounds for `fminbnd` to find the minima.

(a), the red dot indicates the predicted frequency of the next point on the dispersion curve. The determinant value at this point is compared to the frequencies either side ($f_2 + \Delta f = f_3, f_2 - \Delta f = f_1$). The estimated point is updated until it is lower than the neighbouring points. Then, as before, `fminbnd` is used to find the exact frequency-wavenumber pair.

(6) A piece-wise cubic interpolation scheme (`pchip`) is used to estimate the remaining points. Following each prediction, step (5) is repeated to refine the value of frequency. The estimates use the `interp1()` function in MATLAB with the `'pchip'` and `'extrap'` flags. The `pchip` algorithm gives more accurate predictions than the linear scheme (see Figure 4.4 (a)). The cubic interpolation adds “inertia” to help prevent tracing the incorrect modes at points when dispersion curves cross. Additionally, the `pchip` algorithm has smooth behaviour at turning points and flat regions, unlike higher-order polynomials which have a tendency to overshoot and oscillate. The piece-wise cubic spline was fitted with 25 points. It was found that fitting with more points gave a more accurate prediction. This is shown in Figure 4.4 (b). Additionally, the improved accuracy of the predicted point decreased the total time the algorithm needed to run, which levels out at approximately 55 seconds (for a titanium plate in a vacuum between 0 and 5 MHz). This result is shown in Figure 4.4 (c). The decrease in compute time occurs because the predicted point is closer to the true minimum, so it requires less time to perform the

gradient descent part of step (5).

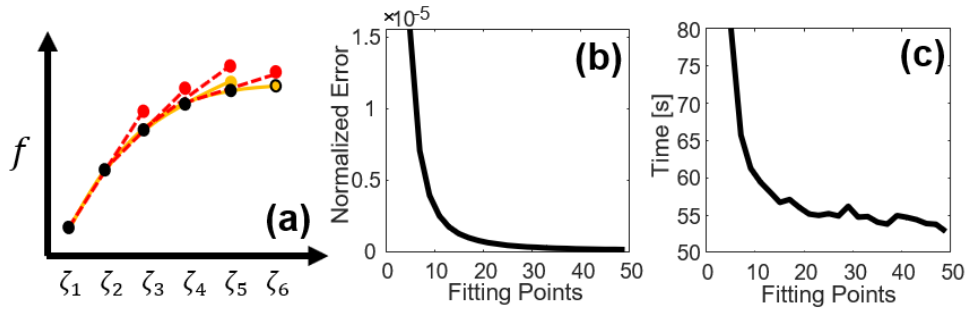


Figure 4.4: (a) For the first two steps in wavenumber (ζ), no interpolation is used. For ζ_2 to ζ_5 linear interpolation is used. For ζ_5 and onward a cubic spline is used. The red points and red dashed line indicated the predictions based on linear interpolation. The orange points and lines indicate the predictions based on the pchip algorithm. (b) Error between the dispersion curve point and the predicted point versus number of fitting points for the cubic spline. The more fitting points used, the more accurate the prediction of the next point. (c) Time taken for the entire dispersion curve algorithm to run versus number of fitting points for the cubic spline. The dispersion curve algorithm runs quicker when more points are fitted.

(7) Finally, a coarse method was also implemented that performs steps (2) and (3) for every wavenumber value and returns the points on the dispersion curves rather than tracing each curve individually. This method is computationally more expensive, but is also more robust as it does not rely on the dispersion curves being connected. This is particularly helpful for difficult problems to trace such as a polymer plate immersed in water. For these very leaky problems it can often be difficult to distinguish a minima. This is shown in in Figure 4.5. Here, the frequency sweep of a titanium plate is shown with a coupling medium of increasing impedance from Z_1 to Z_5 . The minima in the determinant become less pronounced. Currently, the algorithm implemented in `ElasticMatrix` only searches in the real domain of ζ and does not trace the attenuation of each dispersion curve. The attenuation of each curve describes how much of the guided wave energy is leaked into an adjacent medium, for example, a plate embedded in a polymer.

As mentioned previously, the dispersion curves can be easily converted into

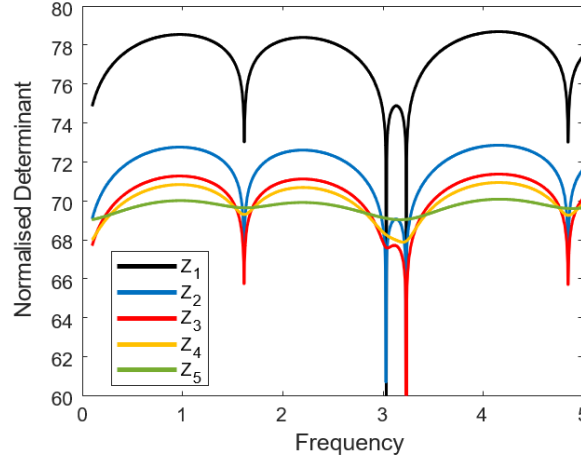


Figure 4.5: Effect of coupling materials with increasing impedance Z on the determinant of the frequency sweep. Here, $Z_1 < Z_2 < Z_3 < Z_4 < Z_5$. The minima become less pronounced when there is a coupling medium of increasing impedance, this makes it difficult to trace dispersion curves in the real ζ domain.

different domains using the relation

$$\zeta = \frac{\omega}{v} = \frac{\omega \sin(\theta)}{c_1}, \quad (4.4)$$

where ζ is horizontal wavenumber, v is the phase velocity, ω is the frequency and c_1 is the bulk velocity in the first medium and θ is the incident angle of the plane wave in the first medium. The group velocity can be found from the gradient of the dispersion curve

$$c_g = \frac{\partial \omega}{\partial \zeta}. \quad (4.5)$$

4.2.3 Time Domain Analysis

The partial wave method finds wave-amplitudes describing the (quasi-)compressional and (quasi-)shear waves in each layer for an incident continuous plane wave of a single frequency. The displacement and stress equations Eq.(3.23) are used to determine the displacement and stress at any coordinate within the sensor. The displacement at coordinate (x_1, x_3) is found by summing the individual contributions from the four partial-waves and taking the real part. The displacement equations

take the form

$$u_i = \sum_{q=1}^4 A_{iq} B_q \exp(i(\zeta x_1 + \zeta \alpha_q x_3 - \omega t)), \quad (4.6)$$

where A_{iq} is amplitude of the wave, ω is the circular frequency and ζ and $\zeta \alpha_q$ are the horizontal and vertical components of the wavevector. The wave-field is plotted by defining a mesh in (x_1, x_3) , and calculating the displacement at each point. This gives the wave-field for a single-frequency plane-wave at time t . The dynamic behaviour of the wave-field is observed by increasing t .

Note, for multilayered media the phase and displacement information at either side of the interface is contained within the complex partial-wave amplitudes. Hence when summing the wave fields, it is important to keep all the values complex and take the real value at the end.

Any incident wave-field can be decomposed into a sum of plane waves. Hence the interaction of a more complex wave-field with a layered structure can be determined. Firstly the angular-spectrum of the desired incident wave-field must be taken. Each component can then be used to calculate a plane wave displacement field. The Fourier coefficient at each frequency is used to weight the fields. They are then summed together and scaled to give the output field. Compared to conventional numerical schemes used to solve the elastodynamic equations, some benefits of this approach are that the results are exact and do not suffer from numerical instabilities, dispersion or stair-casing errors. Additionally, if only the final field at specific coordinates is desired, the simulation only needs to be calculated once for the desired spatial and temporal coordinates (x_1, x_3, t) .

4.3 Software Description

4.3.1 Overview

As mentioned in Section 4.1, the partial-wave method and other matrix models of wave propagation in multi-layered elastic solids have had a significant contribution to different areas of research. This section introduces the `ElasticMatrix` software which aims to make these methods freely available and adaptable to different

research communities.

Some potential uses of this software are: 1) plotting the slowness profiles of materials, 2) determining the reflection and transmission coefficients of multi-layered structures, 3) finding the dispersion curves of layered structures, 4) plotting the displacement and stress fields, 5) extending the toolbox for other applications, for example modelling the directional response of Fabry-Pérot ultrasound sensors [67, 7].

The `ElasticMatrix` toolbox implements the partial-wave method using an object-oriented framework in MATLAB. This allows the toolbox to be used with either a simple scripting or command line interface, and makes it easy to use and expand. The software is divided into three classes. The first class, `Medium`, defines the multi-layered geometry and material properties of each layer. The second class `ElasticMatrix` is initialised by a `Medium` object. This class contains the partial-wave method implementation and methods for extracting additional details such as dispersion curves and reflection coefficients. By default, all the calculations use double (64 bit) precision. The final class, `FabryPerotSensor`, is an example of how numerical models can be built from the `ElasticMatrix` and `Medium` objects. This class inherits `ElasticMatrix` and can be used to model the directional response of a Fabry-Pérot ultrasound sensor. Each class in the toolbox inherits the MATLAB handle class. Consequently, the object does not need to be reassigned when a method is called. The classes and their respective attributes and methods can be seen in Figure 4.6. The toolbox is self contained and has been tested with MATLAB 2016a and above. There are three steps to using the toolbox. Firstly, the geometry of the layered medium must be defined. Secondly, the input parameters to the model should be defined, which are generally a range of angles, frequencies, or wavenumbers. Finally, the model can be solved and details such as the reflection coefficients and dispersion curves can be extracted. Note, for clarity in the code implementation, the x_1 and x_3 coordinates are referred to as x and z , respectively.

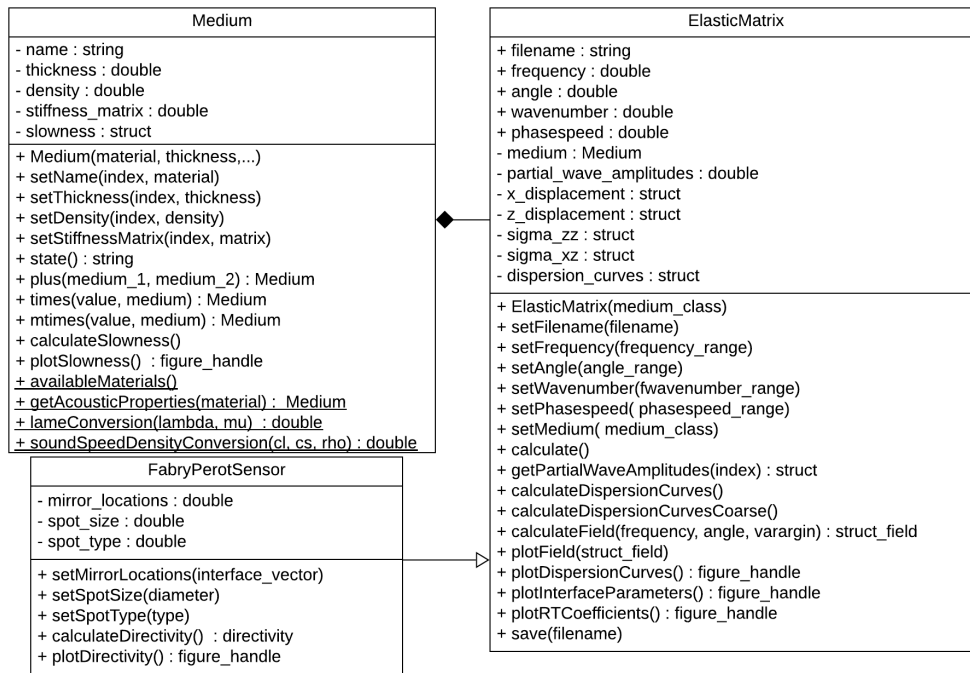


Figure 4.6: UML class diagram for `Medium`, `ElasticMatrix` and `FabryPerotSensor`. The top field for each box indicates the name of the class, the second field lists the properties, and the third field lists the methods. Here, `ElasticMatrix` is composed from `Medium` and `FabryPerotSensor` inherits `ElasticMatrix`. The (-) indicates a private method or property and (+) indicates a public method or property. Underlined methods are static. The type is indicated after the colon (:). Terms inside brackets are the inputs to methods. The figure has been reproduced from [82] with reprint permission under CC BY.

4.3.2 Documentation

A common problem with open-source and academic software is the lack of good documentation. This makes the uptake or use of open source software difficult. `ElasticMatrix` has been extensively documented using the k-Wave [115] coding standard so a user can download the code base and run their first examples within minutes. Detailed step-by-step examples are found in the `ElasticMatrix` `./examples` folder and html documentation can be accessed through the MATLAB help and clicking `ElasticMatrix` toolbox (see Figure 4.7).

The screenshot shows the ElasticMatrix website interface. At the top left, there is a large blue 'Download' button and the URL 'elasticmatrix.org'. To the right, there is a 'Documentation' button with a book icon and 'F1' next to it. Further right, there is a 'Supplemental Software' button with a downward arrow and 'ElasticMatrix Toolbox' below it. Below the 'Download' button, there is a list of examples under the heading 'ElasticMatrix Toolbox (Supplemental Software)'. The examples listed are: Example: Medium Class, Example: Periodic Media, Example: Slowness Profiles, Example: ElasticMatrix Class, Example: Reflection and Transmission Coefficients, Example: Dispersion Curves - Titanium Plate, Example: Dispersion Curves - Teflon Plate, Example: Dispersion Curves - PVDF Plate, and Example: Interface Parameters. To the right of the list, there is a section titled 'Example: Plot Field Parameters' with a paragraph of text explaining how to plot displacement and stress fields. Below this, there is a section titled 'Initialize an ElasticMatrix Object' with a paragraph of text and a code block showing the initialization of a Medium object.

Figure 4.7: ElasticMatrix can be downloaded from the web link or (<http://www.elasticmatrix.org>). After adding the software to the MATLAB path, the html documentation can be accessed in the supplemental software section.

4.3.3 Medium

The `Medium` class is used to define the material properties and thickness of each layer. The class is initialised by calling the class constructor with input arguments of the material name followed by its thickness. However, the thickness of the first and last layers are semi-infinite and their values should be set with the `Inf` keyword. The `Medium` class will automatically set the thickness of the first and last layer to `Inf` if another value is used. An example is given below.

```
my_medium = Medium('water', Inf, 'blank', 3e-3, ...
    'PVDF', 1e-3, 'glass', Inf);
```

Here, `my_medium` is an object array and every index in the object array corresponds to a different layer in the medium. In the current example, `my_medium(3)` returns an object with the material properties and thickness associated with PVDF. The `'blank'` keyword can be used for a material which is not predefined. The material properties and names can be set using their respective `set` functions. User defined materials can be added to the file `materialList.m`.

4.3.4 Slowness Profiles

Slowness profiles are a plot of the inverse of the phase velocity of each bulk wave component. They can be used to determine the angles of reflection and transmission between multi-layered media as well as the direction of energy propagation and skew angle [79]. Slowness profiles are found by solving the Christoffel equation, Eq. 3.13, and only depend on the material properties of each material. The method `.calculateSlowness` is part of the `Medium` class, and calls the function

```
calculateAlphaCoefficients(...)
```

which is an implementation of Eqs. (3.13) and (3.14). This takes input arguments of the material properties and phase-velocity and returns the polarisation and wave-vectors. The slowness profiles given by this function are plotted in terms of k_x/ω vs k_z/ω (where $k_x = \zeta$ is the horizontal wavenumber and $k_z = \zeta\alpha$ is the vertical wavenumber). For an isotropic material, the slowness profiles for each bulk wave are spherical, however, this is not true for an anisotropic material.

An example of the slowness profiles for isotropic-glass and transverse-isotropic beryl is shown in Figure 4.8. This figure has been reproduced from [116]. The slowness profiles of the (quasi-)longitudinal, (quasi-)shear-vertical and (quasi-)shear-horizontal bulk waves are shown. As glass is an isotropic material, the slowness profiles are spherical and the magnitudes of L,SV and SH when $k_x/\omega = 0$ or $k_z/\omega = 0$ are equal to the reciprocal of the compressional- and shear-speeds of glass. For the transverse-isotropic case, when $k_x/\omega = 0$, the value of qL is equal to $\sqrt{\rho/C_{33}}$ and qSV is equal to $\sqrt{\rho/C_{55}}$. When $k_z/\omega = 0$, the value of qL is equal to $\sqrt{\rho/C_{11}}$ and the value of qSV is equal to $\sqrt{\rho/C_{55}}$.

```
my_medium = Medium('glass', Inf, 'beryl', Inf);
my_medium.calculateSlowness;
my_medium.plotSlowness;
```

4.3.5 ElasticMatrix

The `medium` class is used to initialise the `ElasticMatrix` class which runs the partial-wave method over a range of frequencies, wavenumbers, phasespeeds and

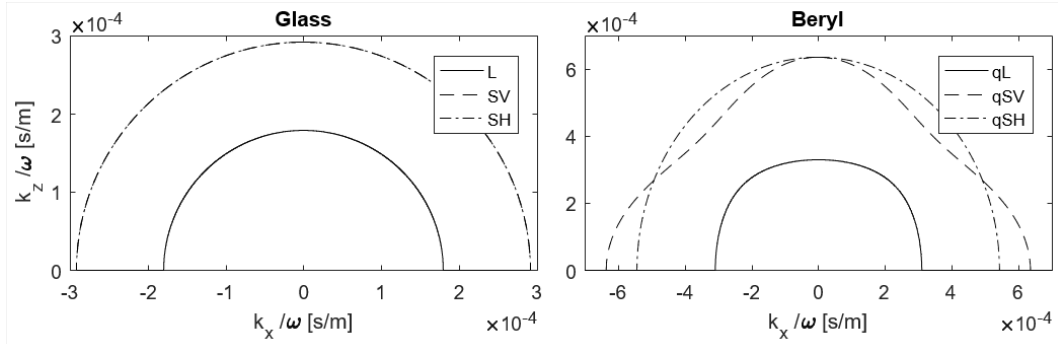


Figure 4.8: The slowness curves for isotropic-glass and transverse-isotropic beryl materials where (q)L, (q)SV, (q)SH correspond to the reciprocal of the (quasi-)longitudinal, (quasi-)shear-vertical and (quasi-)shear-horizontal partial-wave speeds. Note, the SV and SH modes are coincident for glass as it is isotropic. The figure has been reproduced from [82] with reprint permission under CC BY.

angles. Two of these must be defined using the `.set` functions. The `.calculate` method is then used to run the partial-wave procedure. The `.calculate` method constructs, rearranges and solves the global-matrix, Eq. (3.28), using the function

```
calculateMatrixMethod(...)
```

This function takes input arguments of the material properties and the parameters to calculate over (angles, frequencies, wavenumbers). It returns the determinant of the system matrix and the stresses and displacements at the layer interfaces. Each individual field-matrix is calculated using the function

```
calculateFieldMatrixAnisotropic(...)
```

which is an implementation of Eq. (3.23). This takes input arguments of the material properties, the wave-vector components, polarisation components and the phase velocity and returns the field-matrix. The default calculation is to find the partial-wave amplitudes and interface stresses and displacements when there is a single-frequency compressional wave incident on the structure from the first layer. An example is given below for a titanium plate.

```
my_medium = Medium('water', Inf, 'titanium', ...
    1e-3, 'water', Inf);
```

```

my_model = ElasticMatrix(my_medium);
my_model.setFrequency(linspace(1e6, 5e6, 100));
my_model.setAngle(linspace(0, 45, 100));
my_model.calculate;

```

4.3.6 Reflection and Transmission Coefficients

For a plane wave incident at an oblique angle on a multi-layered structure, the reflection and transmission coefficients determine the amplitude of the wave that is reflected and transmitted at each interface. Knowing these coefficients is useful for a number of applications. For example, selecting the appropriate launch angle when coupling energy into particular modes in a wave-guide, or determining the thickness and material properties of matching layers for ultrasonic transducers [79, 117].

The angles of refraction at the interfaces between multi-layered media can be found by studying the slowness profiles. However, slowness profiles do not take into account the boundary conditions at the interfaces. Consequently, the magnitude of each of the refracted waves cannot be calculated directly. For a plane wave incident on a multi-layered structure, the magnitude of the reflection and transmission coefficients are found by normalising the partial-wave amplitudes B_N^n by the incident plane wave amplitude B_1^1 . This is automatically calculated when using the `.calculate` method.

An example of the reflection and transmission coefficients at a PVDF-aluminium interface is given below and shown in Figure 4.9. For a plane compressional wave incident on a PVDF-aluminium interface, there are four resulting refracted waves. These are a reflected R and transmitted T compressional L and shear S wave. These are compared against analytical solutions in greater detail in Section 4.4.

```

my_medium = Medium('PVDF', Inf, 'aluminium', Inf);
my_model = ElasticMatrix(my_medium);
my_model.setFrequency(1e6);
my_model.setAngle(linspace(0, 90, 90));

```

```
my_model.calculate;
my_model.plotRTCoefficients;
```

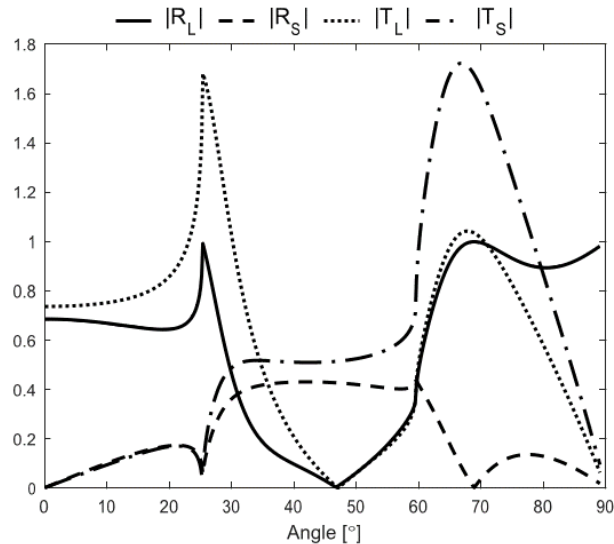


Figure 4.9: Longitudinal L and shear S reflection R and transmission T coefficients for a PVDF-Aluminium interface. The figure has been reproduced from [82] with reprint permission under CC BY.

4.3.7 Dispersion Curves

Dispersion curves describe the modal solutions of the multilayer structure. Knowledge of the dispersion curves is useful for determining the most appropriate modes to excite in ultrasonic inspection.

As mentioned in Section 4.2.2, the modal solutions are found when the global matrix becomes singular. The `ElasticMatrix` software can calculate dispersion curves for simple layered structures (i.e., a plate in a vacuum or water). An example of the dispersion curves for a 1 mm titanium plate in a vacuum is shown in Figure 4.10 (a). The dispersion curves are plotted on a graph of frequency vs wavenumber and show the first three symmetric S and anti-symmetric A Lamb modes. The results from `Disperse` are also plotted and have excellent agreement. Further examples and comparisons are made in Section 4.4.9.

```
my_medium = Medium('vacuum', Inf, 'titanium', ...
    0.001, 'vacuum', Inf);
```

```

my_model = ElasticMatrix(my_medium);
my_model.setFrequency(linspace(0.5e6, 5e6, 100));
my_model.calculateDispersionCurves;
my_model.plotDispersionCurves;

```

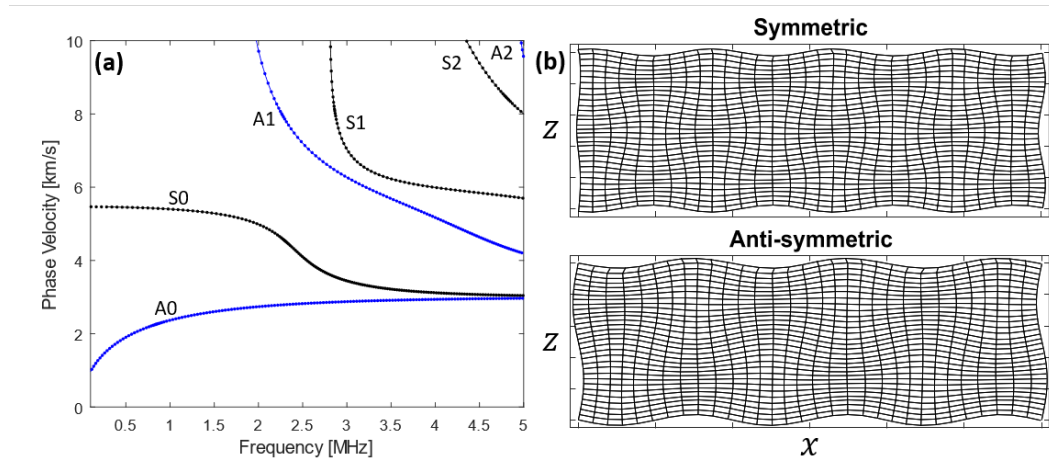


Figure 4.10: (a) Dispersion curves for a titanium plate in a vacuum. The solid lines are from `ElasticMatrix` and the points are generated using `Disperse` [108]. The first three symmetric (S, black) and anti-symmetric (A, blue) are plotted. (b) Displacement field for an anti-symmetric and symmetric mode shape. The figure has been reproduced from [82] with reprint permission under CC BY.

4.3.8 Displacement and Stress Fields

More information about the wave-physics and guided wave structures can be taken from dispersion curves by plotting the displacement and stress fields at different points. In the `ElasticMatrix` software implementation, the x and z ranges over which to plot the displacement or stress fields must be specified. The `.calculateField(...)` method returns a structure with the input ranges and field values at each point of the resulting grid. The values of the structure can be plotted independently or given as an argument to the `.plotField` method. An example is given below for the displacement field within an titanium plate for a symmetric and anti-symmetric mode. The resulting plot can be seen in Figure 4.10 (b).

```

field_values = myModel.calculateField(...)

```

```
freq, angle, {x_range, z_range});  
myModel.plotField(field_values, plot_style);
```

The `plotField` method only plots the displacement and stress field for a single frequency plane wave. Currently there is no available method for plotting field parameters of more complex sources, although more complex sources can be constructed from a sum of plane waves. This code is under development and two demonstrative examples are shown in Figure 4.11 and Figure 4.12. Figure 4.11 shows an incident ultrasound beam reflecting at the Rayleigh angle ($\approx 27^\circ$) at a water-aluminium interface. At this angle, a leaky-Rayleigh wave is generated on the aluminium surface. The incident beam is reflected, and a second beam is emitted which is displaced away from the directly reflected beam. This phenomenon is called Schoch displacement. The model has been used to reproduce this effect, although the two images cannot be directly compared as the exact properties of the experiment are not known. The second example is a finite Gaussian pulse in space incident on an aluminium plate immersed in water, with a snapshot taken at different time intervals. A guided wave is generated in the aluminium plate. This wave leaks energy at discrete intervals into the surrounding fluid and the amplitude decays with distance. There are some banding artefacts caused by wrapping from infinite plane waves. It is hoped these can be ameliorated with further development.

4.3.9 FabryPerotSensor

One of the aims of this thesis is to model the directional response of Fabry-Pérot ultrasound sensors. The `ElasticMatrix` class can solve the elastic-wave propagation problem in multilayered media which is needed for calculating the directional response. The `FabryPerotSensor` is a child class of `ElasticMatrix` and is one example of how the `ElasticMatrix` toolbox may be expanded. This class includes additional inputs for modelling the directional response. The `FabryPerotSensor` is initialised with a `Medium` class which defines the geometry of the Fabry-Pérot sensor. A range of angles and frequencies must be defined using the relevant set functions. The directional response is calculated from the difference in displacement of the mirrors. Currently, the mirror locations are set as

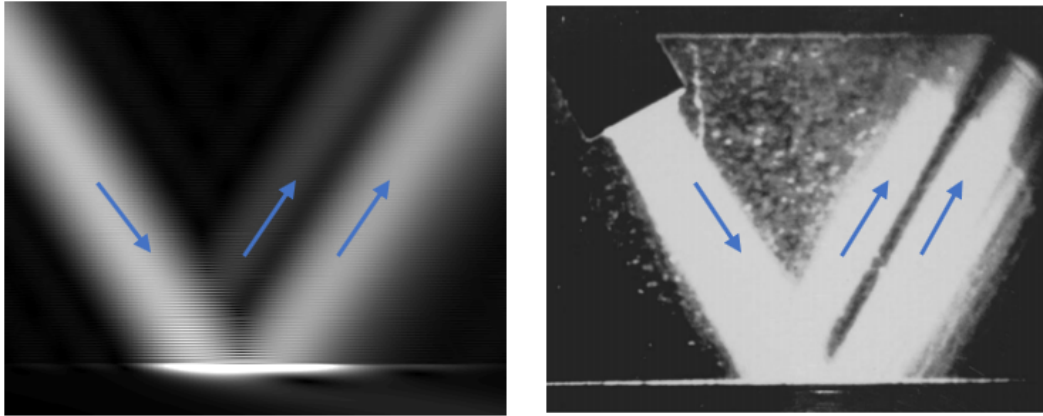


Figure 4.11: Example of Schoch displacement, an incident ultrasound beam at the Rayleigh angle, there is a direct reflected beam and a second beam emitted by the leaky-Rayleigh wave which is displaced from the first. Left: the model. Right: a Schlieren image of Schoch displacement which was presented in Lamanfi et al [118]

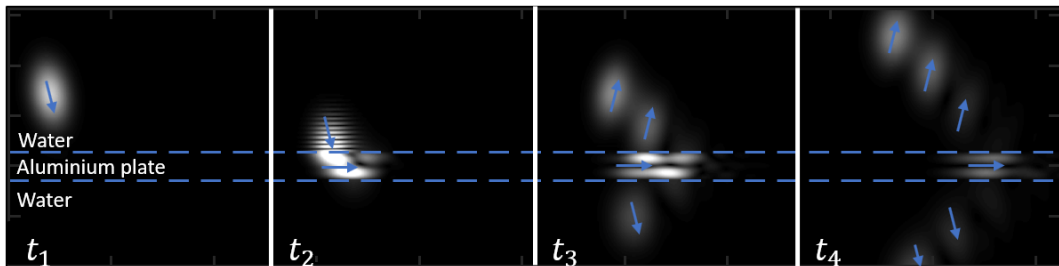


Figure 4.12: The magnitude of the stress of a plate in water. (t_1) A pulse is incident on the aluminium plate. (t_2) The pulse interacts with the aluminium plate, a guided mode is excited. (t_3) A reflected and transmitted pulse can be seen. (t_4) Multiple transmissions can be seen as the guided mode progresses. The amplitude of each subsequent transmission reduces.

the interface locations between layers. For example, for a sensor geometry consisting of three layers (modelling the coupling fluid, spacer and substrate), the mirror interface locations are set to 1 and 2. There is a separate function for modelling the directional response with the inclusion of the strain-optic coefficients, as described in Chapter 2. This will be fully integrated with the `FabryPerotSensor` class in the future. The `FabryPerotSensor` class uses the `ElasticMatrix` methods to calculate the partial wave amplitudes, as described in Chapter 3. The `FabryPerotSensor` then uses the displacements at the mirror interface locations to calculate the directivity. Since all the methods from the `ElasticMatrix`

class are inherited by the `FabryPerotSensor` class, analysis such as the reflection and transmission coefficients, dispersion curves, and plotting field parameters fields can be calculated just the same as before.

An example of the modelled and measured directional response for a glass etalon Fabry-Pérot sensor can be seen in Figure 4.13. Features of the directional response correspond to symmetric and anti-symmetric Lamb modes propagating within the sensor. These results are discussed in greater detail in Chapter 5.

```
my_medium = Medium('water', Inf, 'AlMir', 1e-8, ...
    'glass', 175e-6, 'AlMir', 1e-8, 'air', Inf);
fp_sensor = FabryPerotSensor(my_medium);
fp_sensor.setAngle(linspace(0, 45, 45));
fp_sensor.setFrequency(linspace(0.1e6, 100e6, 100));
fp_sensor.setMirrorLocations([1, 4]);
fp_sensor.calculateDirectivity;
fp_sensor.plotDirectivity;
fp_sensor.calculateDispersionCurves;
```

4.3.10 Run-time

`ElasticMatrix` runs the partial-wave method for every parameter pair specified. The compute time increases linearly with the number of layers for the same number of parameter pairs, and linearly with the number of parameter calculations. These operations use relatively little memory and processor power and can be run on most desktop or personal computers. Figure 4.14 plots the calculation time versus number of layers for 50^2 frequency-angle pairs. For example, the calculation took approximately 12 seconds for a model consisting of forty layers when running on a standard desktop computer (4-core Intel Xeon E3-1240 running at 3.50 GHz with 32 GB of DDR3 2133 MHz memory).

4.3.11 Summary

This section introduces a new open-source toolbox called `ElasticMatrix` which models elastic wave propagation in multi-layered media with anisotropic materi-

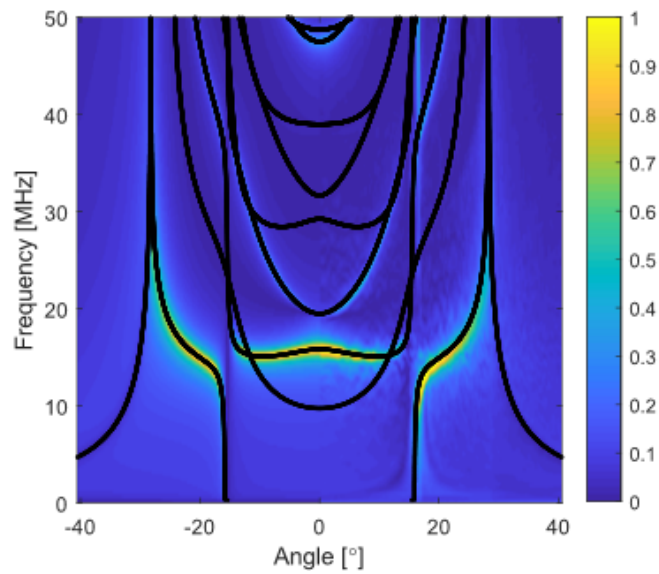


Figure 4.13: The modelled directional response ($-40^\circ - 0^\circ$) and measured directional response ($0^\circ - 40^\circ$) from [67]. The dispersion curves associated with this sensor are plotted as black points. The figure has been reproduced from [82] with reprint permission under CC BY.

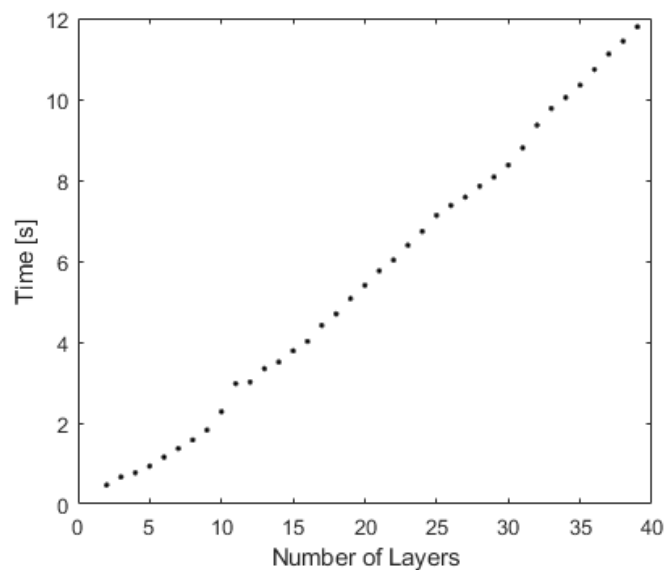


Figure 4.14: The run-time for the partial-wave method versus the number of layers for 50^2 frequency-angle pairs. There is a linear relationship between the number of layers and calculation time. The figure has been reproduced from [82] with reprint permission under CC BY.

als with isotropic, transverse-isotropic or orthotropic symmetry. The toolbox uses the partial-wave method which allows the calculation of slowness profiles, reflec-

tion and transmission coefficients, dispersion curves, and stress and displacement fields. The software has been implemented using the object-oriented capabilities of MATLAB allowing for a simple command line or scripting interface. The implementation allows researchers to add functionality and integrate the software into other projects. It is hoped the research user-base will actively contribute to `ElasticMatrix` and add to the functionality.

4.4 Validation

4.4.1 Introduction

The previous section demonstrates the `ElasticMatrix` toolbox for modelling elastic wave propagation in multilayered media. This section introduces a number of validation examples. Firstly, simple checks are performed to ensure the model is working as expected. Secondly, where possible the model is compared against analytic solutions and commercial software. In this chapter, the absolute difference error between the model and analytical solutions are normalised so that an error of 10^{-16} is machine precision. In most practical applications an error of 10^{-4} is acceptable. Lastly, the model is used to reproduce existing results from the literature.

4.4.2 Boundary Conditions

The simplest check for the model implementation is to ensure the boundary conditions. At the interface between two solid media, the normal and transverse stress and displacements are continuous. Therefore, the stresses and displacements at interface i calculated with the field matrix and partial-wave amplitudes of layer l must be the same as the stresses and displacements at interface i calculated with the field matrix and partial-wave amplitudes of layer $l + 1$.

A test was performed to check whether the partial-wave amplitudes from adjacent layers gave the same values for the stresses and displacements. This was done by evaluating the displacements and stresses at a small distance within both media, either side from the interface. The distances were reduced until both were evaluated at the same coordinate. As the distance is reduced, the percentage error reduces smoothly. At the limit of the interface, the errors in the displacements and stresses are on the order of machine precision (10^{-16}).

A similar test was performed to check the error at the interfaces for a multilayered structure containing fluid, elastic and anisotropic materials. It was found the mean errors in the stresses and displacements at the interfaces were on the order of (10^{-16}). It must be noted however the transverse displacement for fluid-elastic interface is discontinuous. Additionally, for fluid layers the shear stress should be

zero, however numerically the shear stress was on the order of (10^{-8}) . This error occurs for a couple of reasons. Firstly, fluid materials are represented as elastic materials with small shear speeds (1 m/s to avoid divide by zero errors). Secondly, the boundary conditions for transverse displacements are not explicitly removed when dealing with fluid-solid interfaces. The errors propagate into the calculation of the wave-vector components and global matrix construction. These small numerical errors could be ameliorated in future by explicitly calculating the wave-vector components for fluids and removing equations relating to the continuity of transverse displacements at fluid interfaces. The value of 1 m/s was chosen to minimize the errors that propagate. Figure 4.15 contains a plot of the displacement and stresses through an example multilayered structure. The $u_z, \sigma_{zz}, \sigma_{xz}$ are continuous across every interface and u_x is continuous across all interfaces except those adjacent to fluids.

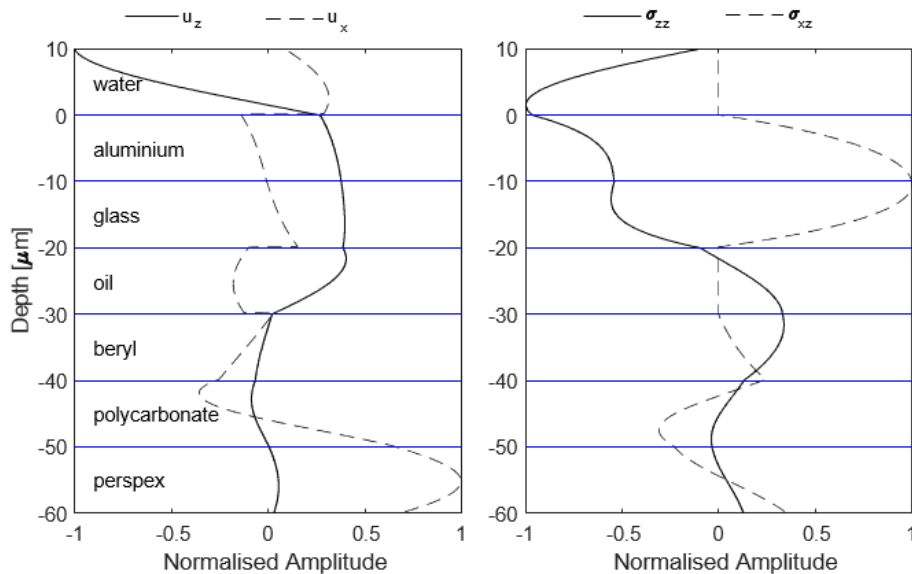


Figure 4.15: Visualisation of the field parameters for an arbitrary frequency and wavevector for an arbitrary multi-layered structure with a mixture of isotropic, anisotropic and fluid layers. Note, the displacement and stresses are continuous across every interface except for the fluids, hence the boundary conditions are holding. Additionally, the shear stress is 0 for a fluid as they cannot support shear waves.

4.4.3 Comparison with Potential Method

It was mentioned in Section 3.3.4 that the potential method was implemented separately. The potential method and partial-wave method are mathematically identical in the isotropic case. A test was performed for a multilayered structure over a range of frequencies and angles comparing the interface displacement, stresses, and the amplitudes of the potential and partial-wave amplitudes for each layer. The average error for each of these parameters was on the order of (10^{-16}). This test demonstrates that with two different implementations and derivations the same results are achieved. The following validation examples only describe the results from the partial-wave implementation for clarity, however, the same tests have been performed for the potential method and both implementations give the same results.

4.4.4 Displacement in Water

The displacements given by the model are arbitrarily scaled to that of an incident wave pressure of 1 Pa in water. The values from the model were compared to the analytical formula for the maximum particle displacement in water. This is given by

$$u_w = \frac{P}{Z\omega}, \quad (4.7)$$

where u_w is the maximum particle displacement, P is the pressure, Z is the acoustic impedance and ω is the angular frequency. This relationship indicates the maximum particle displacement for a harmonic plane wave is inversely related to frequency. A two layer medium was initialised and each layer was set to have the properties of water. The model was calculated for an acoustic wave incident normal and at 45 degrees to the “interface” between the layers. The magnitude of the complex displacements returned by the model were calculated and plotted against the analytical result for 0 and 45 degrees, this can be seen in Figure 4.16. (The model was checked at a range of angles between 0 and 90 degrees but only two are plotted). The model matched the analytical results with an average numerical error of less than ($< 10^{-8}$). The small numerical error compared to machine precision occurs because fluid media are represented with a small shear speed. The error propagates when calculating

the wavevector components with the Christoffel form. As discussed previously, these errors can be improved by explicitly removing equations related to transverse displacement for fluid-media, however, is small enough for almost all practical purposes. This test demonstrates the scaling of the model is correct. Additionally, as the scaling coefficient can be factored out of the partial-wave derivation, different scalings can be achieved by multiplying the output displacements by the relevant factor. For example, to have the displacements at 10 Pa, the output displacements simply need to be multiplied by 10. However, this may not be realistic for every material if the elastodynamic behaviour is non-linear with pressure.

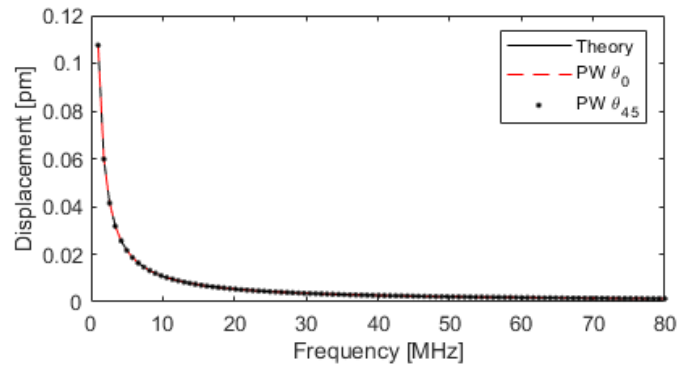


Figure 4.16: Check of the displacement scaling in water at a pressure of 1 Pa. The magnitude of the displacement calculated should be the same for a plane wave travelling at any angle.

4.4.5 Fluid-Fluid Interface

The angle-dependent reflection and transmission pressure coefficients at the interface between two fluid half-spaces are plotted in Figure 4.17. Two cases were modelled and compared to the analytical formulae found in Cheeke [1]. The first case is from a fluid of a higher impedance to a lower impedance, and the second is the reverse case. The sound speed and density of medium 2 are $c_L = 3000, \rho = 3000$ and the sound speed and density of medium 1 are $c_L = 1480, \rho = 1000$.

When the incident wave is travelling from a half space of lower impedance to a higher impedance there is a critical angle present. Figure 4.17 (c) and (d) demonstrates this as the pressure reflection coefficient peaks and becomes unity. In the reverse case, there are no critical angles hence there are no peaks in the reflected

or transmitted wave as seen in Figure 4.17 (a) and (b).

The partial-wave and analytical models are in close agreement. The average error between the partial-wave and analytical model is on the order of (10^{-5}) . As discussed previously, this numerical error occurs from the representation of fluid media with a small shear speed. Further tests were performed where the impedance ratio between the first and second fluid (and vice-versa) was taken from 1:1 to 1:1000. At the highest impedance ratio, the average errors were still on the order of (10^{-5}) .

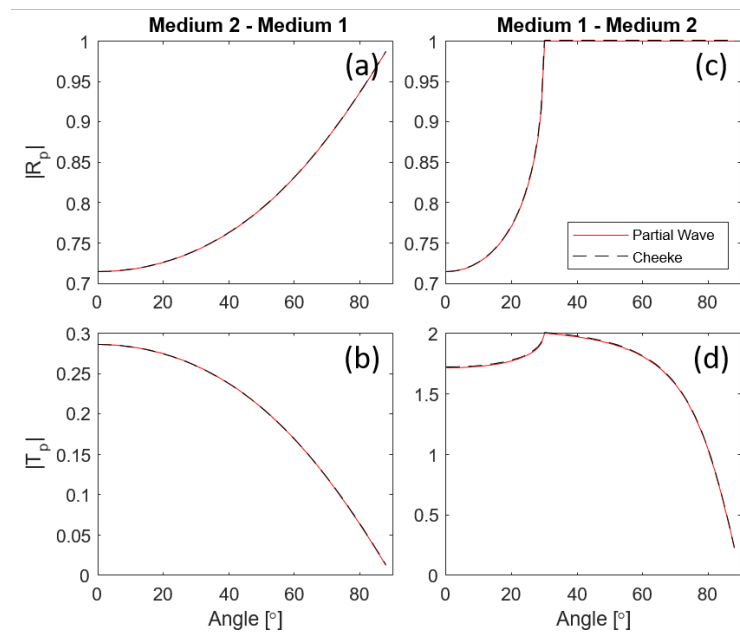


Figure 4.17: Fluid-Fluid interface. Medium 2 has a higher impedance than medium 1. (a, b) Magnitude of pressure reflection and transmission coefficients from medium 2 to medium 1. (c, d) Magnitude of pressure reflection and transmission coefficients between medium 1 and medium 2. There is a critical angle present seen as a peak in the reflection and transmission coefficients.

4.4.6 Fluid-Solid Interface

The angle-dependent reflection and transmission displacement coefficients at the interface between a fluid and solid half-space were validated against the analytical solutions in Cheeke [1]. These solutions only describe isotropic materials. Two different cases were studied. The first is the reflection and transmission between water and perspex, and the second is between water and aluminium. Three bulk waves may exist for a compressional plane wave incident on the interface between

a solid half space and liquid half space. These are a reflected compressional wave, a transmitted compressional wave, and a transmitted shear wave.

The displacement reflection and transmission coefficients of the water-perspex interface can be seen in Figure 4.18. The compressional and shear speeds of perspex are $c_L = 2700$, $c_S = 1300$. Only the compressional wave-speed is higher than that of water, which means there is only one critical angle at 34° from the compressional wave. This can be seen as a peak tending to unity in the reflection coefficient. After the first critical angle there is a strong shear wave generated in the perspex. This can be seen as the large increase in shear transmission coefficient, $|T_S|$. This decays at higher angles of incidence.

The energy coefficients of the water-perspex interface can be seen in Figure 4.19. There is a large peak in the reflected energy coefficient (blue) at the critical angle. Before this the majority of the energy is transmitted as a compressional wave (solid red). After the critical angle, the compressional reflection and transmission energy coefficients drop and the majority of the energy is converted into a transmitted shear wave (red dashed).

The displacement reflection and transmission coefficients of the water-aluminium interface can be seen in Figure 4.18. There is good agreement between the partial-wave and analytic models. The compressional and shear speeds of aluminium are $c_L = 6400$, $c_S = 3100$. Both the compressional (13.4°) and shear critical (28.5°) angles can be seen as the reflection coefficient becomes unity.

Additional information can be obtained from studying the energy in the reflection and transmission coefficients, as shown in Figure 4.19. Prior to the first critical angle, the majority of the energy is concentrated in a reflected compressional wave (blue) and transmitted compressional wave (solid red). At the first critical angle, all of the energy is reflected and the transmitted waves tend to zero. Between the first and second critical angle, there is no transmitted compressional wave and mode conversion occurs as there is a strong transmitted shear wave (red dashed). After the second critical angle, no energy is transmitted and all of the energy is reflected. Although the transmitted energy coefficient after the second critical angle is zero,

the displacement transmission coefficient may be non-zero. This is because after the second critical angle, the displacement transmission coefficients may become complex indicating the presence of an evanescent (inhomogeneous) wave. The amplitudes of evanescent waves are maximum at the interface and decay exponentially away from the interface. The result is that they do not carry energy away from the interface, hence have zero energy coefficients.

The mean error between the partial-wave and analytical model is on the order of (10^{-5}) for the reflection coefficient and transmission coefficients. Again, the small numerical errors occur from the representation of fluid media with a small shear speed. Further tests were done comparing where the impedance ratio between the first and second medium was taken from 1:1 to 1:1000. At the highest impedance ratio, the average errors were still on the order of (10^{-5}) . Rose [79] provides a solution for the reflection and transmission coefficients for a solid-solid interface. When calculating the reflection and transmission coefficients (for the two fluid-solid cases mentioned above) using the Rose model and comparing with the partial-wave method, the errors are on the order of (10^{-16}) . This is because the Rose model, like the partial wave model, represents the fluid layers with a small shear speed.

4.4.7 Solid-Solid Interface

The reflection and transmission coefficients from a compressional wave incident on the interface between two solid elastic half-spaces is considered here. In this case, there are four bulk waves generated from a single incident wave. These are reflected and transmitted shear and compressional waves. Two examples were chosen and compared with the solutions given by Rose [79]. These are an aluminium-perspex and an perspex-aluminium interface. Both examples have good agreement with the solution from Rose, and the mean error of the displacement coefficients is on the order of (10^{-16}) .

Figures 4.20 (a) and (b) show the shear and compressional reflection and transmission displacement and energy coefficients for the aluminium-perspex interface. Both the shear and compressional wave speeds of aluminium are higher than those

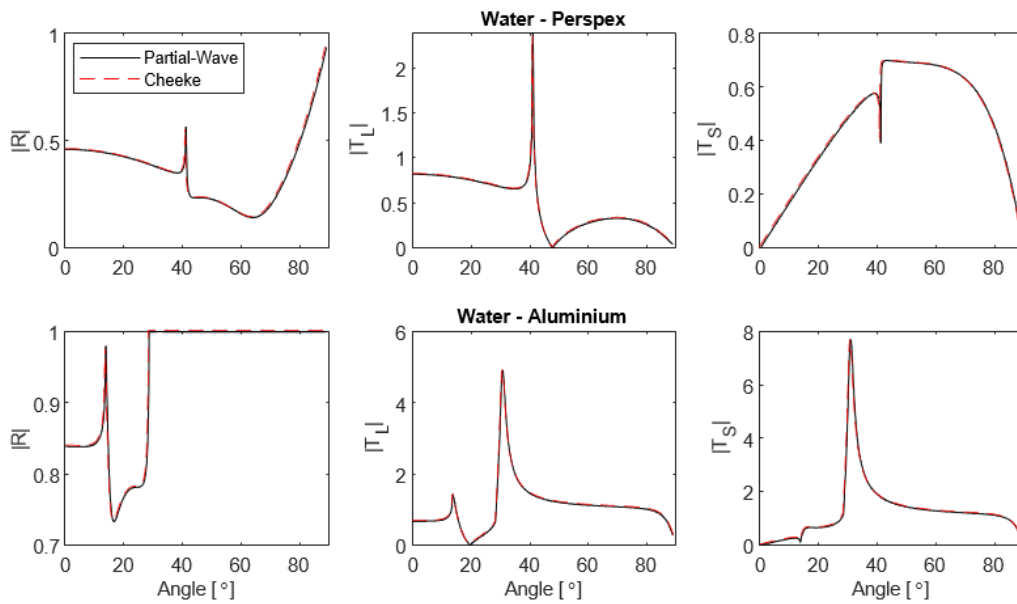


Figure 4.18: (Top-row) Magnitude of the displacement reflection and transmission coefficients for a wave incident on a water-perspex interface compared with analytical results from Cheeke. The horizontal axis is the angle of incidence and the vertical axis is the magnitude of the displacement coefficients. There is only one compressional critical angle which is seen as a sharp peak in the reflection coefficient. After the critical angle there is a large shear wave generated. (Bottom-row) Displacement reflection and transmission coefficients for a water-aluminium interface. There are two peaks in the reflection coefficient which occur from a compressional and shear critical angle. After the second critical angle the reflection coefficient becomes unity and the transmission coefficients become complex resulting in a non-zero magnitude.

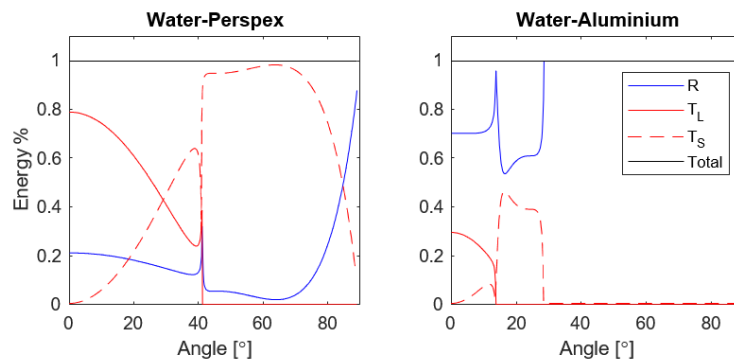


Figure 4.19: Reflection and transmission energy coefficients for a water-perspex and water-aluminium interface.

of perspex hence there are no critical angles present. The dominant reflected and transmitted waves are compressional, however, between 40° and 70° there is a

strong shear wave generated. At 90° there is total reflection as this is equivalent to a wave travelling perpendicular to the interface.

Figures 4.20 (c) and (d) shows the shear and compressional reflection and transmission displacement and energy coefficients for the perspex-aluminium interface. In this case there are two critical angles as the bulk wave velocities of perspex are less than that of aluminium. The two critical angles occur at 25° and 60° , which appear as peaks in the reflection and energy coefficients. Prior to the first critical angle, the dominant bulk waves are compressional, and between the critical angles the dominant wave type is shear.

Further tests were performed where the impedance ratio between the first and second solid, and vice versa were taken from 1:1 to 1:1000. In each case the shear speed was set to half the compressional wave speed. At the highest ratio, when the lowest impedance was in the second layer, the average errors were still on the order of (10^{-16}) . In the reverse case (1:1000) the errors were on the order of (10^{-10}) . This might not be reliable as the Rose solution was badly scaled in this case. However, when the ratio was 1:100, the average errors were on the order of (10^{-16}) . This ratio is higher than the vast majority of material combinations. For example the speed of sound in diamond is approximately 12 kms^{-1} and the density is 3500 kgm^{-3} , hence the impedance $Z_d = 42 \text{ MRayl}$ while the impedance of water is approximately $Z_w = 1.5 \text{ MRayl}$, hence the ratio of impedance between these two materials is 1:28.

4.4.8 Three-Layers Normal Incidence

The model was compared to the analytical expression describing pressure reflection and transmission coefficients for a three-layer structure at normal incidence from [119]. This can be seen in Figure 4.21. The three layers are PZT ($c_L = 4000, \rho = 7500$), a matching layer ($c_L = 1540, \rho = 2236, d = 100 \mu\text{m}$) and tissue ($c_L = 1540, \rho = 974$). At 7.5 MHz, the reflection coefficient tends to zero and the transmission coefficient peaks. This occurs when there is a quarter wavelength in the matching layer leading to destructive interference in the reflected field and maximum transmission occurs. The mean error between the analytical and partial-wave model for the reflection and transmission coefficients is on the order

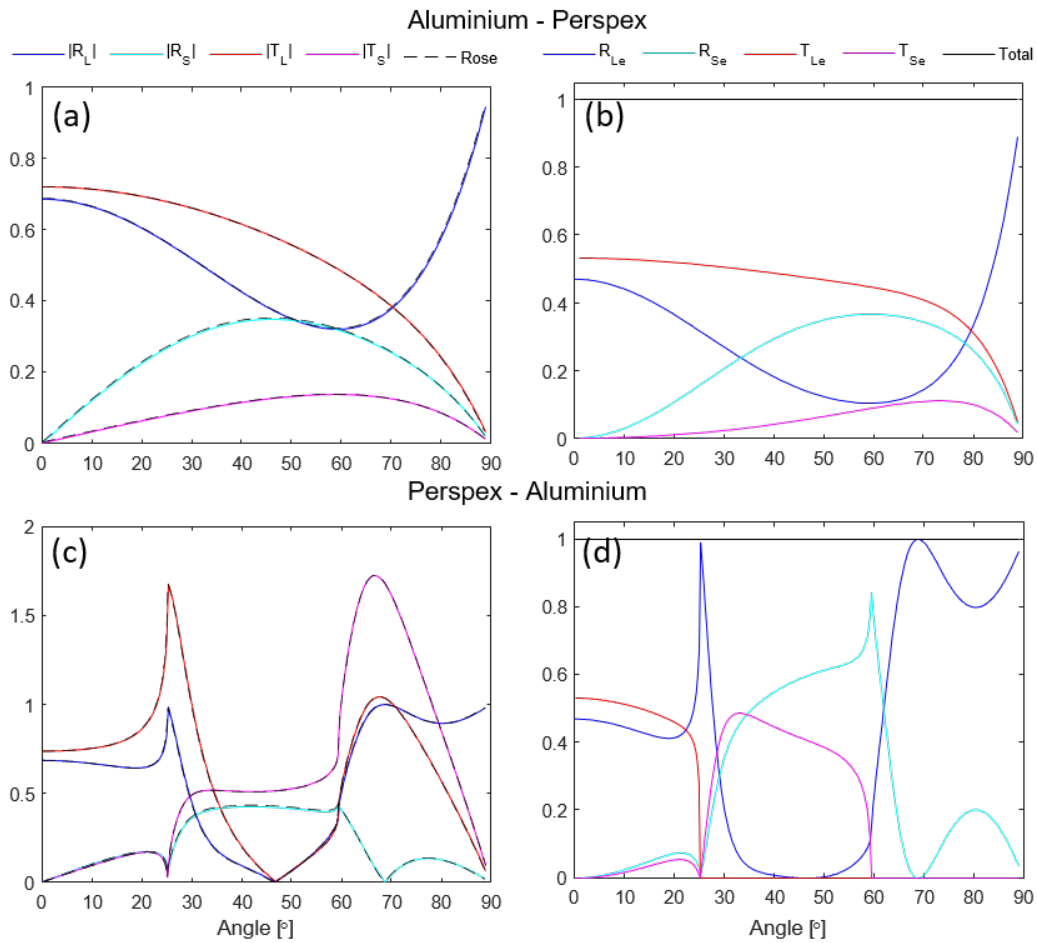


Figure 4.20: (a) Magnitude of the displacement reflection and transmission coefficients for a aluminium-perspex interface. (b) Energy coefficients for aluminium-perspex interface. (c) Displacement coefficients for a perspex-aluminium interface. (d) Energy coefficients for perspex-aluminium interface.

of (10^{-16}) .

4.4.9 Dispersion Curves

The dispersion curve algorithm was compared with examples in Disperse [108]. A number of examples were chosen to represent different use cases. The first two examples correspond to a 1 mm titanium and Teflon plate in a vacuum. These can be seen in Figure 4.22 (a) and (b). There is excellent agreement between Disperse and `ElasticMatrix`, however, a direct comparison was not possible because it is not possible to choose the corresponding wavenumbers and frequencies in the Disperse calculation. The red curves correspond to symmetric Lamb modes and the

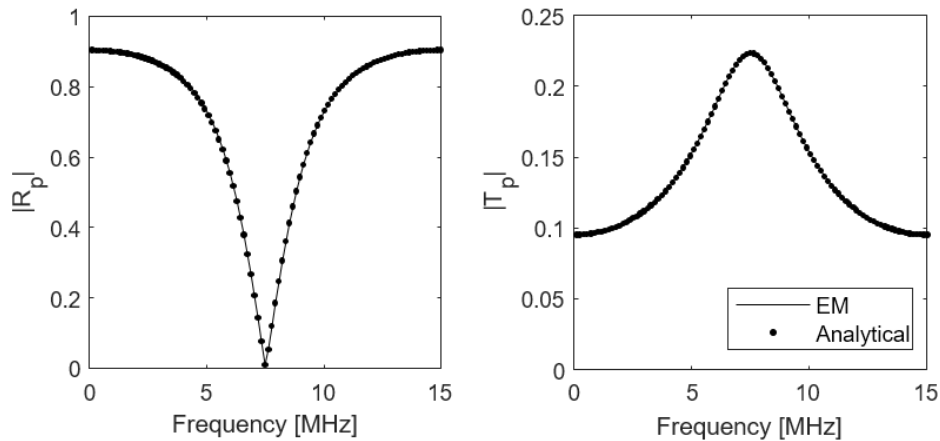


Figure 4.21: Pressure reflection and transmission coefficients for three layers at normal incidence. The reflection coefficient dips and the transmission coefficient peaks when the quarter wave condition is met in the matching layer.

blue curves correspond to anti-symmetric Lamb modes. At low frequencies, only the fundamental modes exist, (A0) and (S0). At higher frequencies, higher order modes appear. The A0 and S0 mode shapes coalesce at high frequencies and couple into a Rayleigh wave travelling on the interface of the plate. The Lamb modes are discussed in more detail in the next subsection. The third example is a two-layered plate consisting of 1 mm of Teflon on 1 mm of Titanium in a vacuum. This can be seen in Figure 4.22 (c). Here, the curves from Disperse are in red and the black points are from `ElasticMatrix`, and again there is excellent agreement. These modes are guided modes but cannot be classed into symmetric or anti-symmetric modes.

The previous examples were relatively easy for `Disperse` and `ElasticMatrix` to compute as the guided modes solutions are not attenuated by being embedded in a coupling fluid or medium. In the next few examples, the plates are immersed in a fluid. Figure 4.23 (a) and (b) correspond to a titanium and Teflon plate in oil. The red curves are from `Disperse` and the points are from `ElasticMatrix` using the “coarse” method. It can be seen that `Disperse` cannot completely trace the dispersion curves. `ElasticMatrix` seems more robust with the coarse method but also appears to pick up spurious modes and bulk wave speeds. The final example is for a titanium plate embedded in Teflon, both `Disperse` and `ElasticMatrix`

struggle to trace the modes correctly.

Tracing leaky-modes is a notoriously difficult problem and both `Disperse` and `ElasticMatrix` struggle to completely trace the guided modes. Some advantages of `Disperse` is speed as it is a compiled application it can trace the curves in seconds whereas `ElasticMatrix` takes minutes. Additionally `Disperse` can trace the attenuation coefficients of leaky-modes. The lack of robustness for very leaky-cases is a limitation of the partial-wave method. Other techniques based on the spectral-collocation method or semi-analytic finite element method have been shown to be more accurate and robust [108, 109, 110, 111, 112, 120].

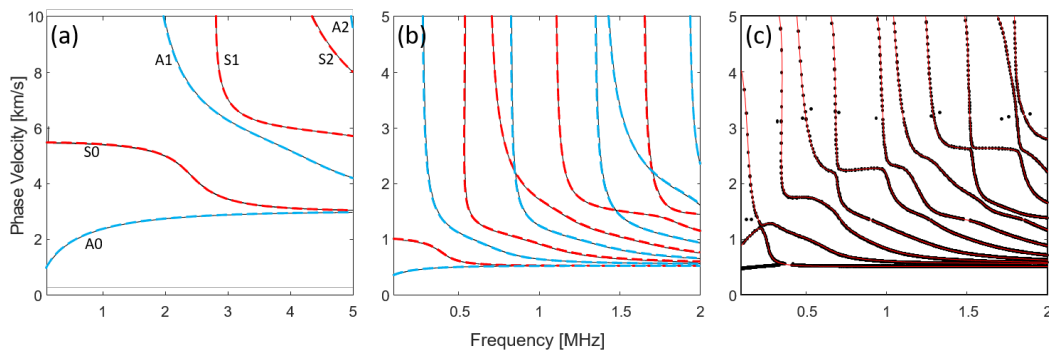


Figure 4.22: (a) 1 mm Titanium plate in a vacuum. (b) 1 mm Teflon plate in a vacuum. For examples (a) and (b) the solid black line is from the `ElasticMatrix` implementation and the dashed coloured lines are from `Disperse`. The red lines correspond to symmetric Lamb modes and the blue lines correspond to anti-symmetric Lamb modes. (c) A 1 mm Teflon + 1 mm titanium plate in a vacuum. In this example the solid red line is from `Disperse` and the black points are from `ElasticMatrix` using the “coarse” method. These curves correspond to guided modes but cannot strictly be classified as symmetric or anti-symmetric Lamb waves.

4.4.10 Mode shapes of Guided Waves

A selection of mode shapes from a water-aluminium interface and an aluminium plate immersed in water are plotted here. Figure 4.24 plots the mode shapes, vector fields of characteristic motion of the Rayleigh wave (R), symmetric (S0) and anti-symmetric (A0) Lamb modes.

Figure 4.24 R demonstrates the characteristic motion of a Rayleigh wave. Here, a vector field has been plotted where the vertical axis represents the distance into the aluminium, and the horizontal axis is parallel to the surface of the

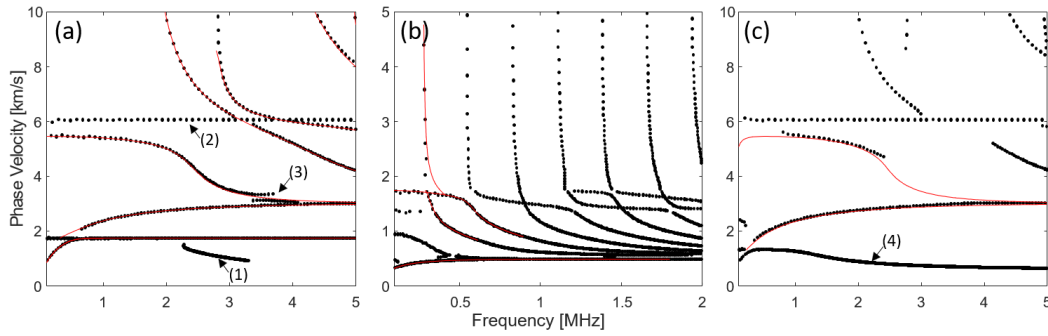


Figure 4.23: (a) Titanium plate in oil. (1) A spurious wave mode. (2) Bulk wave speed on Titanium. (3) Incorrect position of the A0 and S0 mode. (b) Teflon plate in oil. (c) Titanium plate embedded in Teflon. (4) Spurious mode. The red curves are from Disperse and the points are from ElasticMatrix.

half-space. $z = 0$ is the location of the water-aluminium interface. The vector field demonstrates the elliptical motion of the Rayleigh wave that decays exponentially away from the surface (located at $z = 0$). This is more clearly demonstrated in the mode shape plot. The vertical axis is the same as the vector field and the horizontal axis represents the relative displacement amplitude in z (dashed) and x (solid). This plot demonstrates how the amplitude of the Rayleigh mode decays with depth and the maximum displacement is just below the interface.

The mode shapes of the S1 and A1 Lamb waves can be seen in Figure 4.24. The vector plots of the displacement fields have been plotted. Here, the horizontal axis is parallel to the interface of the plate and the vertical axis from 0 to -1 is the thickness of the plate. The normalised mode shape has been plotted to the right. The in-plane (x) displacement is symmetric and anti-symmetric about the centre of the plate for the S1 and A1 mode shape, respectively. The vector plot of the S1 mode indicate there are regions of rotation that periodically alternate direction and are symmetric about the centre of the plate ($z = -0.5$). This has the effect of stretching or compressing the plate causing an hour glass shape. The vector plot of the A1 mode has alternating regions of displacement which causes one side of the plate to compress and one side of the plate to stretch. This gives rise to the rippled structure of the anti-symmetric mode.

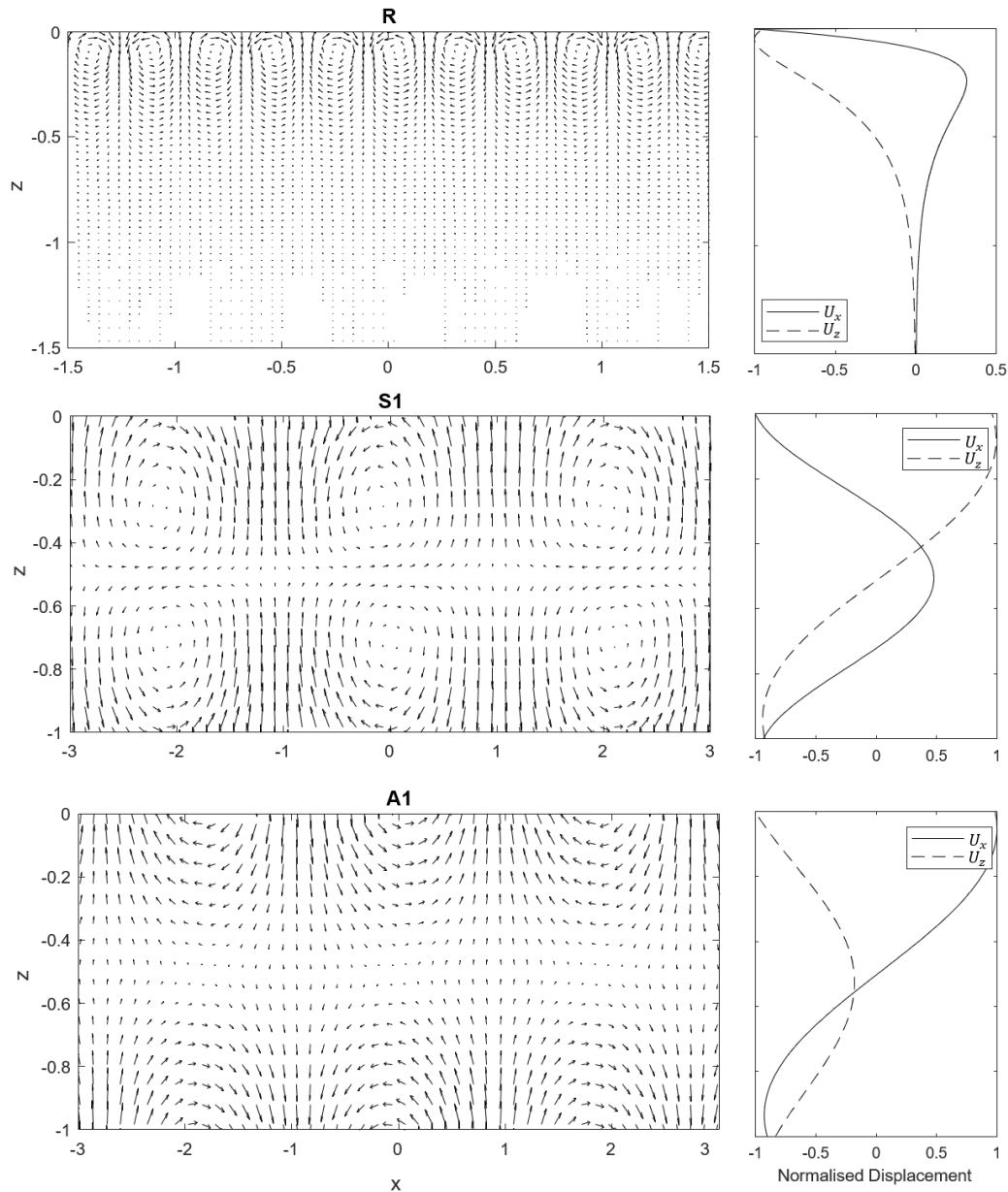


Figure 4.24: Vector field snapshot (left column) and a profile through Z of the normalised u_x, u_z displacement (right column) of the Rayleigh (R), first-order symmetric (S1) and anti-symmetric (A1) modes.

4.4.11 Comparison with Previous Models

The partial-wave implementation for modelling directivity was compared with previous results from Beard [49] and Cox [7], to demonstrate the partial-wave model reduces down to previous models. Figure 4.25 shows the modelled frequency response of six different sensor configurations against the measurement data from

Beard [49]. The vertical axis is the mean stress amplitude normalised to value at $f = 0$, and the horizontal axis is the frequency. These sensors primarily consisted of a PET film glued to a glass or PMMA backing or with a water backing. Discrepancies appear at higher frequencies ($> 20\text{MHz}$), which may occur from uncertainties from low SNR, jitter, uncertainty in the glue thickness, and differences between the angular alignment [49].

The system matrix produced by the partial-wave method can be shown analytically to simplify to the previous three-layer model by Cox [7]. Figure 4.26 reproduces the key frequency-dependent directional response result from Cox between $0 - 45^\circ$ and $0 - 15\text{MHz}$. The sensor modelled by Cox consists of a Parylene C spacer deposited on a glass substrate. The sensor was illuminated by a collimated beam with a diameter of $400\mu\text{m}$. This means the effect of spatial averaging dominates the response of this sensor, and appears as concentric rings.

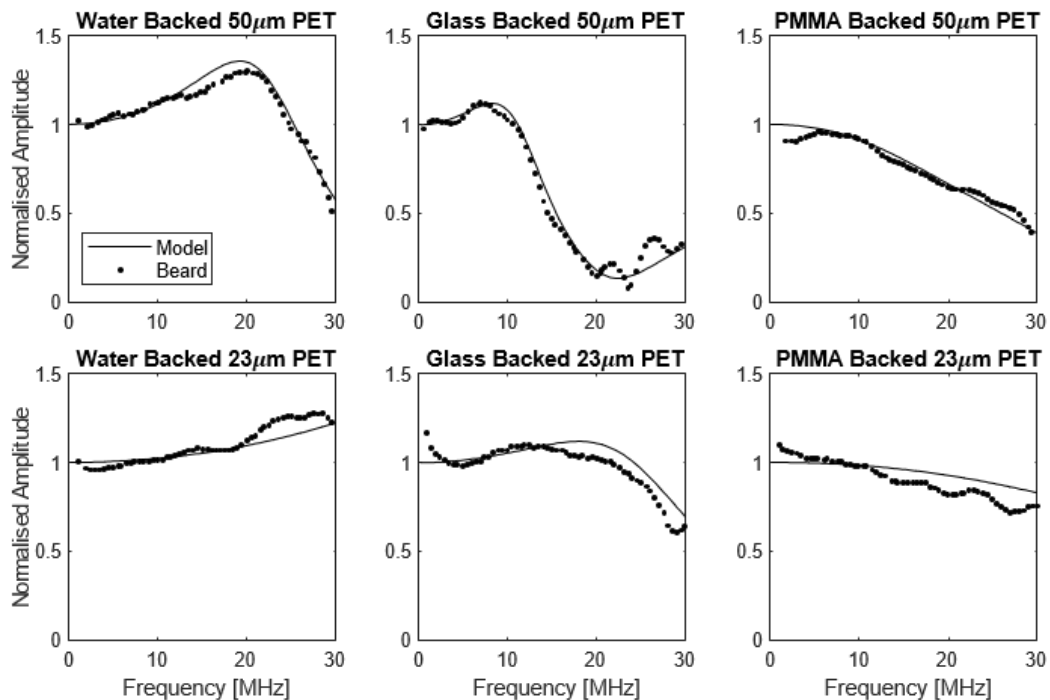


Figure 4.25: Reproduction of six results from Beard [49]. The horizontal axis is frequency and vertical axis is the mean stress amplitude normalised to the value at $f = 0$. The blue line is the frequency response modelled by the partial-wave method and the points indicate data taken from Beard.

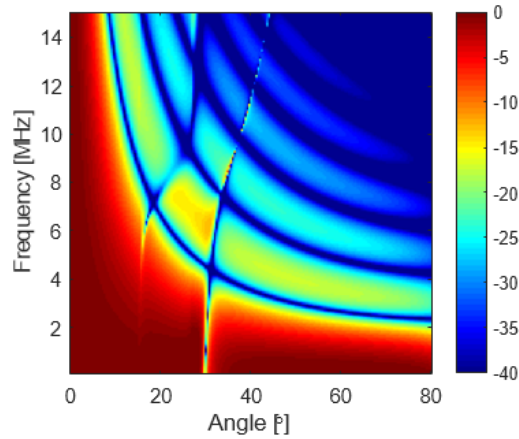


Figure 4.26: Reproduction of the key frequency-dependent directional response result from Cox [7]. The vertical axis represents the frequency and horizontal axis angle. The directivity is normalised to the on-axis frequency response and the colour represents the sensitivity of the sensor at that angle and frequency in decibels. The concentric rings occur from spatial averaging from the beam width of the interrogation laser.

4.5 Summary

This chapter introduced a new open-source toolbox called `ElasticMatrix` which models elastic wave propagation in multi-layered media with anisotropic materials with isotropic, transverse-isotropic or orthotropic symmetry. The software has been implemented using the object-oriented capabilities of MATLAB allowing for a simple command line or scripting interface. The implemented model has been validated against analytical solutions, commercial software and existing literature.

Chapter 5

Analysis of the Directivity of Glass Etalon Sensors

5.1 Introduction

This chapter brings together the analysis and methods of the previous chapters to model the directivity of two glass-etalon Fabry-Pérot sensors. Firstly, the model was compared with the experimentally measured directional response of an air-backed cover-slip Fabry-Pérot sensor with well-known material properties. This was used to validate the model for high frequencies (up to 100 MHz) where there were multiple acoustic wavelengths within the spacer. Secondly, the model was compared with the measured directional response of an all-hard-dielectric Fabry-Pérot sensor. This sensor can be used for high-intensity focused ultrasound (HIFU) measurements [5]. Additionally, the model was used to analyse, in detail, how different features of the directivity arise from wave modes present in the sensor.

The transduction mechanism has been discussed previously in Section 2. However, for clarity a brief description of the sensor's transduction mechanism is repeated in Section 5.2. Directivity measurements and comparisons to the model are given in Section 5.3 and Section 5.4. The origin of the features present in the directional response are discussed in Section 5.5. Finally, the influence of the strain-optic coefficients on the directional response is investigated in Section 5.6.

The conference proceeding in [121] © IEEE 2017, conference proceeding in

[122] © IEEE 2019, and journal article in [67] © IEEE 2019 have been adapted to form parts of this chapter.

5.2 Transduction Mechanism Review

Two different Fabry-Pérot sensors were investigated. The first sensor was constructed from a glass microscope cover-slip ($175\ \mu\text{m}$), which had thin partially-reflecting aluminium mirrors ($< 1 \times 10^{-8}\ \text{m}$) deposited on either side. The cover-slip was mounted at the edges to a polycarbonate frame which gave the cover-slip an air-backing. The second sensor consisted of two partially reflecting dielectric mirrors separated by a thin spacer deposited on a glass substrate. The dielectric mirrors were constructed from twelve $\lambda/4$ thick (at $1550\ \text{nm}$) alternating layers of silicon dioxide, SiO_2 , and zirconium dioxide, ZrO_2 , separated by a spacer made from SiO_2 , where λ refers to the optical wavelength within the material. An illustrative diagram of the sensors can be seen in Figure 5.1. The material properties of these sensors can be found in Table 5.1.

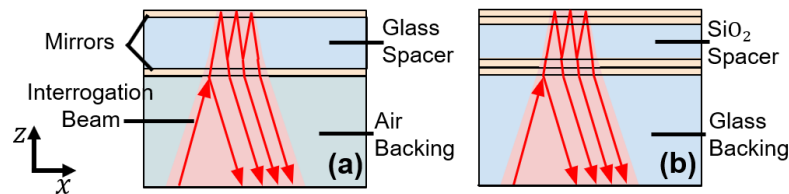


Figure 5.1: (a) Air-backed glass cover-slip sensor with thin aluminium mirrors. (b) Hard-dielectric sensor with a glass backing.

The Fabry-Pérot ultrasound sensor detects ultrasound using interferometry, where an incident acoustic wave modulates the optical path length via two mechanisms. The first mechanism is a physical change in the optical path length as the distance between the two mirrors is modulated. This is calculated by taking the difference in the vertical component of the displacement field, u_z , at the top and bottom mirrors. The second mechanism is a change in the refractive index Δn of the spacer layer caused by local changes in density. The spacer layer is assumed to be optically isotropic, homogeneous and non-absorbing. If the interrogation laser

beam is parallel to the z -axis and polarized in the x -axis, the change in refractive index can be written

$$\Delta n = -\frac{1}{2}n_0^3 \left(p_{11} \frac{\partial u_x}{\partial x} + p_{12} \frac{\partial u_z}{\partial z} \right). \quad (5.1)$$

Here, n_0 is the refractive index of the glass cover-slip and p_{11} and p_{12} are strain-optic coefficients (SOCs). As discussed previously in Section 2, this is only valid for planar sensors. If the incident laser light is parallel to z and polarized in y , the SOC p_{11} is replaced with p_{12} in Eq. (5.1). The p_{12} SOC is multiplied by the normal strain in the z -axis and the p_{11} SOC is multiplied by the normal strain in the x -axis. For clarity, the normal strain in the x -axis will be referred to as the transverse strain. The SOCs for a few glassy materials are given in Table 5.2.

The frequency-dependent directional response, $D(f, \theta)$, to a plane wave of frequency f and angle of incidence θ can be calculated by weighting the two mechanisms by the interrogation beam profile $S(x, y)$ and integrating over the interrogated area A :

$$D(f, \theta) \propto \int_A \left(n_0 (u_z(z_2) - u_{z_2}(z_1)) + \int_{z_1}^{z_2} \Delta n \cdot dz \right) S(x, y) dA. \quad (5.2)$$

The aluminium mirrors are significantly thinner than the cover-slip for the air-backed cover-slip sensor. In this case, the mirrors can be considered infinitesimally thin and the acoustic phase changes associated with the mirrors can be accounted for by increasing the thickness of the cover-slip [19]. Additionally, since the aluminium mirrors are highly reflective for the optical interrogation wavelength used here, the contribution of the strain-induced refractive index changes in the coupling fluid can be considered much smaller than the interference effect within the cover-slip. Hence, just the strain-optic effect within the cover-slip needs to be considered [19]. This is not necessarily the case for multi-layered dielectric mirrors, which are thicker and have different refractive indices and SOCs for each material layer [60, 50, 51].

Table 5.1: Table of material properties. Table reproduced from [67] © IEEE 2019.

Material	c_L (m/s)	c_S (m/s)	ρ (kg/m ³)
Water [79]	1448	0	1000
Glass [79]	5570	3430	2500
SiO ₂ [123]	5900	3700	2500
ZrO ₂	-	-	5680
Air [79]	330	0	1
Aluminium [79]	6250	3100	2700

c_L , c_S : compressional and shear sound speeds, ρ : density.

Table 5.2: Table of strain-optic coefficients. Table reproduced from [67] © IEEE 2019.

Material	p_{11}	p_{12}	n_0
SiO ₂ /Quartz [75, 51]	0.121	0.27	1.456
Fused silica (7940) [124]	0.126	0.26	1.457
Fused silica (7070) [124]	0.113	0.23	1.469
PMMA (Plexiglass 55) [125, 126]	0.300	0.297	1.49

5.3 Measuring the Directional Response

5.3.1 Overview

There are a number of different methods of measuring directivity, these can be found in the references [9, 20, 127, 128, 33, 13, 3, 14, 33, 129, 31]. The method employed in these measurements is the same as demonstrated by Guggenheim [31].

The Fabry-Pérot sensors were mounted within the base of a specially designed water bath suspended above the optics required for the interrogation of the sensors. A diagram is included in Figure 5.2. A focused laser beam, which had an estimated interrogation spot size of 50 μm and was tunable in the range of 1440 to 1640 nm (Tunics T100S-HP, Yenista Optics, France), was used to interrogate the Fabry-Pérot sensor. A broadband mono-polar photoacoustic source was created using a 25 mm diameter polymer disk coated with a thin layer of highly absorbing black paint (Super Gloss, PlastiKote). This polymer disk was positioned at the end of a 10 cm lens tube and was irradiated by an (Ultra) Q-Switched Nd:YAG laser at 1064 nm emitting short (≈ 6 ns) pulses at a rate of 20 Hz. The pulse was mono-polar and broadband (Figure 5.3). This source was attached to a mechanical arm connected to

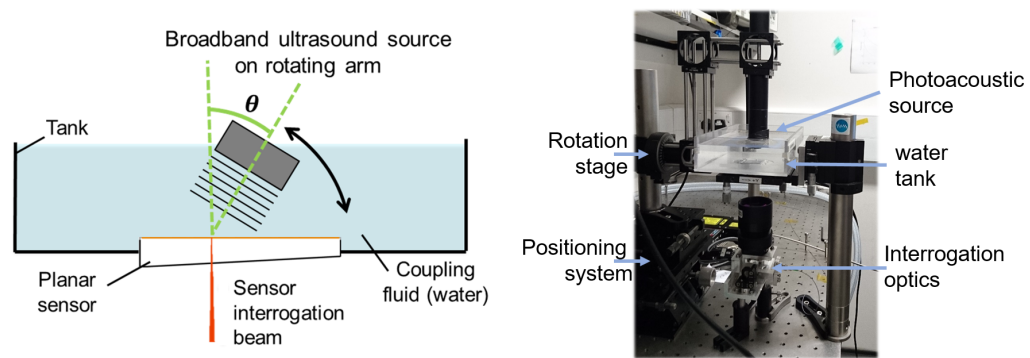


Figure 5.2: The Fabry-Pérot sensor is placed at the base of a bath of deionised water. A broadband laser generated ultrasound source is attached to a moveable stage which rotates at 0.25° increments about the interrogation point on the surface of the Fabry-Pérot sensor. Figure reprinted from [67] © IEEE 2019.

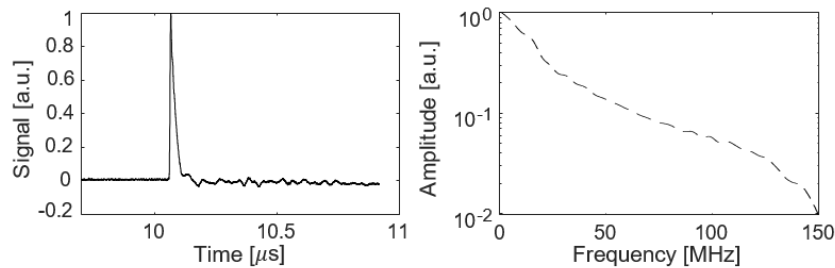


Figure 5.3: Left, waveform of the photoacoustic pulse at normal incidence after 100 averages. Right, FFT of the waveform. The data was collected with an all hard-dielectric sensor which has a -3dB bandwidth at 62 MHz [5].

a rotation stage (PRM1/MZ8, Thorlabs). The rotation stage was controlled through a custom LabVIEW program which allowed precise angular movements in steps of 0.25° . To allow precise alignment of the Fabry-Pérot sensor with the source, the sensor was positioned on a manual five-axis (x , y , z , tip and tilt) positioning system, as shown in Figure 5.2 [31].

5.3.2 Process of Alignment

To accurately measure the directivity, it was important to ensure the position of the sensor was a constant distance from the source at every acquisition angle. Firstly, the correct lateral position was found, which made it easier to find the correct vertical position. With reference to Figure 5.4, to get the correct lateral position, the source angle θ was moved to a $+\theta$, (for example, $\theta = 10^\circ$), and the time of arrival

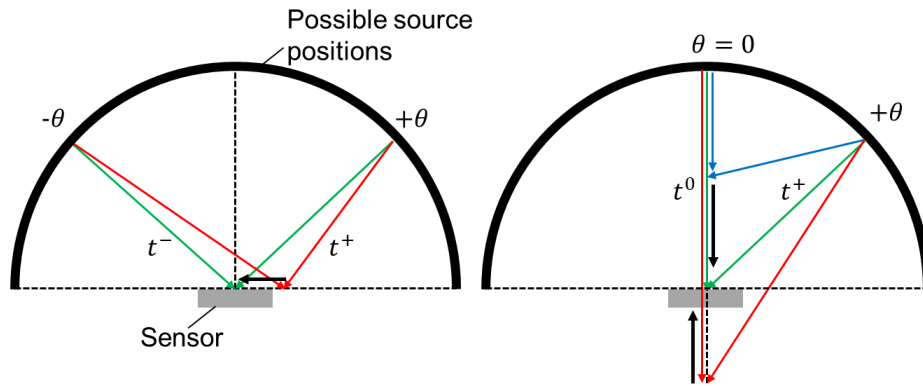


Figure 5.4: Left, the process of lateral alignment. The sensor is moved to the left or right until the time of arrival $t^+ = t^-$. Right, the process of the vertical alignment.

t^+ (TOA) of the photoacoustic pulse was noted. The source was then moved to a $-\theta$, and the TOA t^- of the pulse was compared with the first. If $t^+ < t^-$ the sensor was moved to the left (see Figure 5.4), and if $t^+ > t^-$ then the sensor was moved to the right. This procedure was repeated until $t^+ = t^-$ to give the correct lateral alignment. After the sensor has been aligned laterally, the vertical alignment was found by comparing the TOA of the pulse at normal incidence, t^0 and the TOA from a positive (or negative) angle, t^+ . If $t^0 < t^+$ then the sensor was moved down and if $t^0 > t^+$ the sensor was moved up. When $t^0 = t^+$ the sensor was aligned vertically.

5.3.3 Data Processing

The data was acquired by rotating the photoacoustic source about the sensor in 0.25° steps and recording the waveform at each angle with a digital storage oscilloscope [31]. Each signal acquisition was triggered by the digital trigger from the laser source. Due to the geometry of the water bath in which the sensor was positioned, the directional response measurement was limited to $\pm 45^\circ$. At the extreme angular ranges the lens tube of the photoacoustic source was in contact with the walls of the water bath. There were 20 averages taken for the hard-dielectric sensor and 100 averages for the air-backed cover-slip. Each acquired signal was zero padded, multiplied by a Tukey window (taper ratio = 0.7) of 3 to 6 μs centered about the maximum of the signal and fast Fourier transformed (FFT). An example of an acquired waveform can be seen in Figure 5.3. In most cases, the measurements were

normalised to the normal-incidence frequency response. If there were many zeros in the normal incidence response the data (and model) was scaled so that the maximum of the normal incidence response was equal to unity. If the data is normalised, when there are zeros in the frequency response, it causes banding artefacts in the directional response.

5.4 Model Results

5.4.1 Validation Air-Backed Glass Cover-slip

`ElasticMatrix` was used to model the frequency-dependent directional response. The model was validated by comparing it with measurements made with the air-backed cover-slip sensor.

The medium geometry consisted of a three layer structure using the predefined materials: water, glass and air. The range of frequencies was set from 0.1 to 100 MHz. The range of angles was set from 0 to 45°. As there were three layers, the mirror locations were set to the first and second interface (as the aluminium mirrors were assumed to be negligibly thin). The interrogation spot was set to ‘Gaussian’ with a diameter of 50 μm .

Figure 5.5 shows the measured (a) and modelled (b)-(c) directional response between $\pm 40^\circ$ and 0 – 100 MHz. To remove the effect of the frequency-dependence of the photoacoustic source, the measured data in these figures were normalized so that the magnitude of the normal-incidence frequency-response matched the modelled frequency-response, as shown in Figure 5.5 (d). Usually, the directivity would be normalised by the low frequency-normal incident value. However, zeros in the normal-incidence frequency-response causes significant banding artefacts. Therefore this alternative normalisation was chosen.

Figures 5.5 (b) and 5.5 (c) show the modelled directivity with and without refractive index changes. The differences due to including the refractive index changes are negligible when compared with the noise in the measurement. In Section 5.5, the features of the directional response are sufficiently described by considering only the difference in the vertical displacement of the two mirrors. Ad-

ditionally, the strain-optic coefficients are not known or easily measured for thin-film dielectric-mirrors and add further uncertainty in the modelling of the all-hard-dielectric sensor [51]. For the following figures and directivity analysis of the two sensors the contributions from refractive index changes are neglected. However, the strain-optic effect is given special consideration in Section 5.6.

The air-backed cover-slip is thick ($\approx 175 \mu\text{m}$) when compared with the shortest acoustic wavelength supported by the incident wave. At resonant frequencies there is constructive or destructive interference within the cover-slip which cause peaks and nulls in the frequency response. At normal incidence, the resonant peaks occur when $n\lambda + \lambda/2$ is equal to the cover-slip thickness, where $n = 0, 1, 2, 3, \dots$ and λ is the acoustic wavelength within the cover-slip. The peaks can be seen at 16, 47 and 79 MHz in Figure 5.5. The nulls occur when $n\lambda$ is equal to the cover-slip thickness. There are nulls at 31, 62 and 94 MHz. At non-normal angles of incidence there are a variety of features which can be best seen in Figure 5.6 which shows horizontal profiles through the directivity colormap. These arise from critical angles and guided wave phenomena and are described in more depth in Section 5.5.

5.4.2 Hard-Dielectric Sensor

The model was used to help interpret and explain the features of the directional response of a hard-dielectric sensor recently used for measuring the field generated by a HIFU transducer [5]. However, the acoustic properties of the dielectric mirrors used in this sensor are not known. To overcome this, effective material properties were found by fitting the model to the measured directional response of the HD sensor.

The dielectric mirrors consisted of twelve alternating layers of vapour-deposited silicon dioxide and zirconium dioxide. Over the measurement bandwidth, the shortest acoustic wavelength is much larger than the thickness of any individual layer in the dielectric mirror. Therefore, the multilayered mirror structure was modelled as a single layer with effective properties for thickness, compressional sound speed, and shear sound speed. In total, the medium geometry was modelled as a five layer structure, water, mirror, silicon-dioxide, mirror, and glass. As the mir-

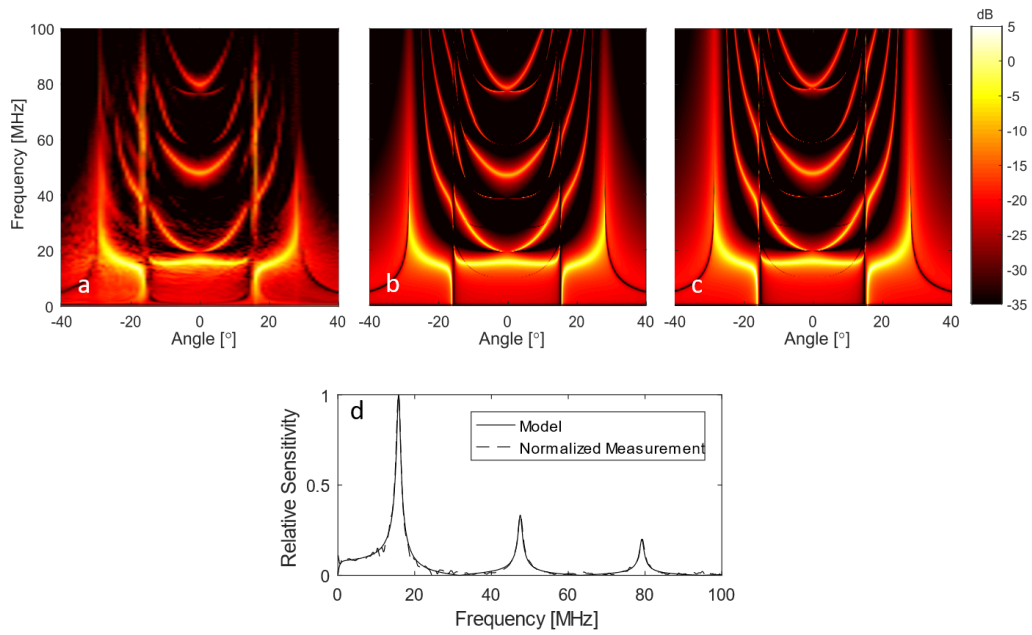


Figure 5.5: (a) Measured directivity in decibels of the air-backed cover-slip sensor. The measurements were taken at 0.25° intervals using a photoacoustic signal generated by a 40 mJ laser pulse with 200 averages acquired between -40° and 40° . (b) Modelled directivity excluding refractive index changes and (c) modelled directivity including refractive index changes where $p_{11} = 0.113$ and $p_{12} = 0.23$ [124]. Both the measured and modelled directivity have been normalized by the maximum of the first peak in the normal-incidence frequency-response. (d) Model excluding refractive index changes (solid line) and normalized measurement (dashed line) of the normal-incidence frequency-response. Figure reprinted from [67] © IEEE 2019

rors were significant in thickness compared with the spacer, their thicknesses were included in the “two effective interfaces” method described in [19]. The material parameter fitting was performed using the `globalsearch` and `fmincon` functions from the Global Optimization Toolbox in MATLAB. These functions were used to minimize the sum-of-squared differences (SSD) between the measured and modelled directional responses by varying the model values for the compressional sound speed, shear sound speed, and thickness of the dielectric mirrors. The range of values were 2000 to 6000 ms^{-1} for the compressional sound speed, 1000 to 6000 ms^{-1} for the shear sound speed and 0.5 to $5\mu\text{m}$ for the thickness. The measured data was filtered using a low-pass filter (one-sided Gaussian, -3dB point at 30 MHz) to regularize the inversion against high frequency noise in the measurements. The

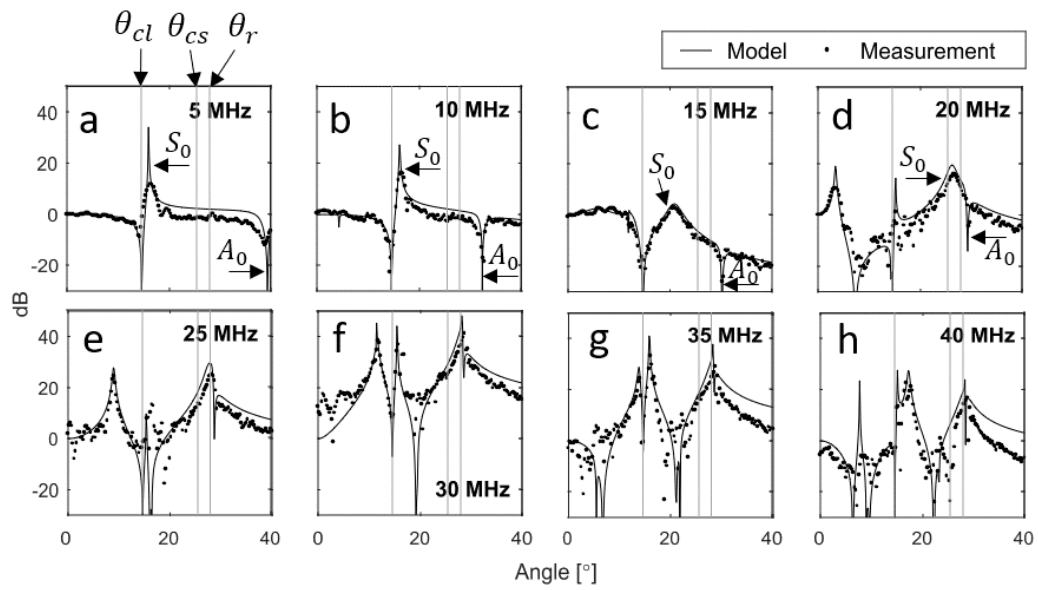


Figure 5.6: One sided profiles of the air-backed sensor at 5 MHz intervals up to 40 MHz of the measured (points) and modelled (line) directivity normalised to the normal-incidence frequency response. Note the vertical axis is in decibels. Figure reprinted from [67] © IEEE 2019

implementation of the inversion routine was validated using both noise-free and noisy synthesized data. The values found for the estimated parameters are shown in Table 5.3.

When using these fitted material properties, there is good agreement between the measured and modelled directional response. Figure 5.7 shows the magnitude of the measured (a) and modelled (b) directional response for the hard-dielectric sensor normalized to the normal-incidence frequency response. This is plotted between $\pm 45^\circ$ for a range of frequencies from 0 – 50 MHz. The corresponding phase response is shown in Figure 5.7 (c) and (d). One-sided profiles of the directional response are shown in Figure 5.8. The mirrors and spacer of the hard-dielectric sensor is thin ($\approx 9 \mu\text{m}$) when compared with the shortest wavelength present in the incident wave resulting in a flat frequency-response.

Table 5.3: Effective dielectric mirror parameters. Table reproduced from [67] © IEEE 2019.

Parameter	5-layer
Spacer thickness (μm)	3.885
Effective Thickness HD Mirror (μm)	1.40
Effective HD mirror c_L (ms^{-1})	4921
Effective HD mirror c_S (ms^{-1})	1930

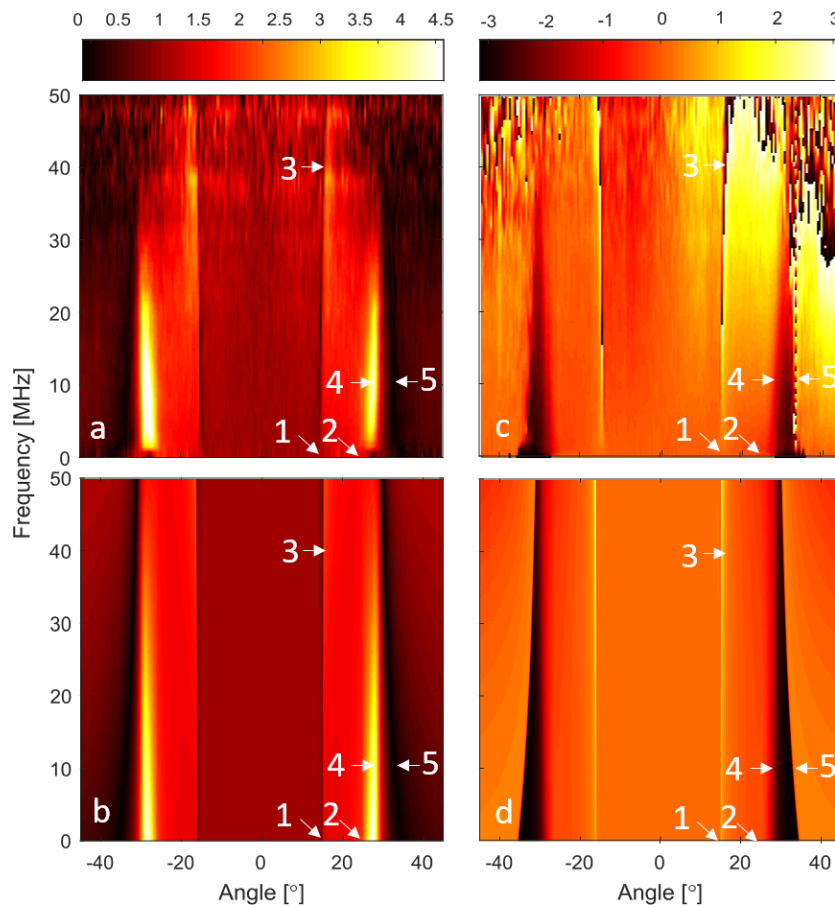


Figure 5.7: (a) Directivity measurement of the hard-dielectric sensor presented by Martin et al. [5], and (b) modelled directivity of the same sensor. The results are given on a linear scale. (c) Phase response of the directivity measurement presented by Martin [5] and (d) modelled phase response of the hard-dielectric sensor. Key features: 1) compressional and 2) shear critical angles, 3) peak after water-substrate and water-spacer compressional critical angles at high frequencies, 4) peak preceding Rayleigh wave with a frequency-dependent phase speed, 5) minimum due to no difference in the vertical displacements of the mirrors. Figure reprinted from [67] © IEEE 2019.

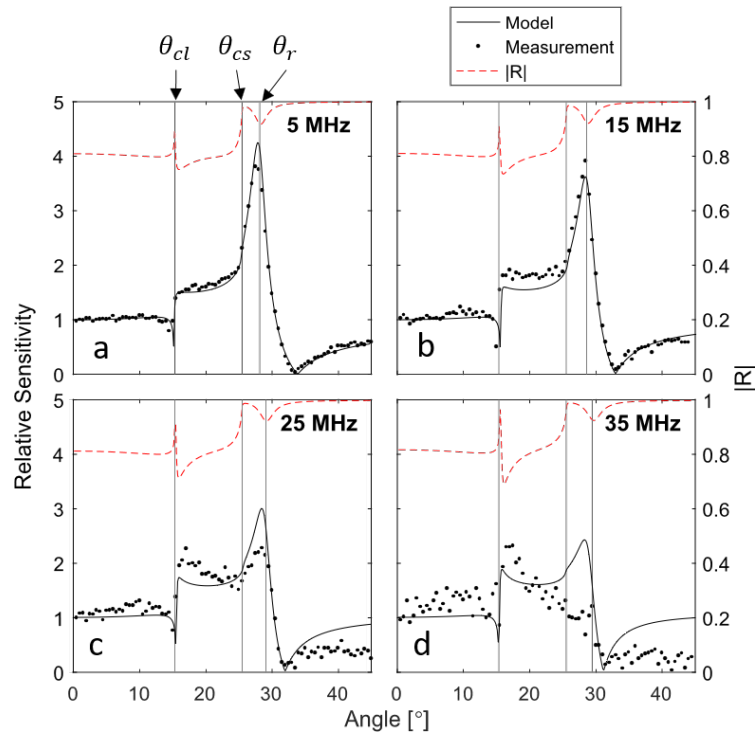


Figure 5.8: One sided profiles of the hard-dielectric sensor at 5, 15, 25 and 35 MHz of the measured (points) and modelled (solid) directivity. The magnitude of the modelled reflection coefficient (red dash) at each frequency is plotted for reference. The left vertical axis is the relative sensitivity of the directional response profiles. The right vertical axis is the magnitude of the reflection coefficient. The vertical grey lines indicated on (a) represent the compressional critical angle θ_{cl} between water and glass, the shear critical angle θ_{cs} , and the leaky-Rayleigh angle θ_r . Figure reprinted from [67] © IEEE 2019.

5.5 Feature Analysis

5.5.1 Overview

In Section 5.4, the model was validated by comparing it with directional response measurements, but the responses themselves were not analysed in terms of the underlying acoustic wave interactions. The key features of the directional responses for the hard-dielectric and air-backed cover-slip sensors have been labelled in Figure 5.7 and Figure 5.10, and are discussed in detail in Sections 5.5.2 to 5.5.4. Generally, the features of the directional response can be associated with wave phenomena in the sensor. For example, features which occur over a narrow angular range for every frequency appear as vertical bands in the directional response and are associated with compressional and shear critical angles. Also, maxima occur when the incident wave couples into symmetric Lamb waves or Rayleigh waves, and minima may occur from anti-symmetric Lamb waves or other cases when both mirrors are moving in phase and have the same displacement.

5.5.2 Critical Angles

Hard-dielectric sensor: In general, the acoustic wave incident on the Fabry-Pérot sensor couples into both compressional and shear waves. These effects are more apparent on the directivity of the hard-dielectric sensor, hence this is discussed first. At the water-substrate compressional critical angle ($\theta_{cl} = 15.4^\circ$) there is an evanescent compressional wave which is perpendicular to the substrate. The vertical displacement of the evanescent mode decays exponentially from the water-mirror interface into the substrate. At low frequencies, the wavelength is large compared to the thickness of the mirrors and spacer, and both mirrors have a similar displacement. As there is no significant difference in displacement between the two mirrors there is a null in the sensitivity. This can be more clearly observed when looking at profiles of the directivity, as shown in Figure 5.8 (a) to (d). Here, one-sided profiles of the directivity have been plotted at four frequencies. The modelled reflection coefficient $|R|$ has also been plotted as a reference commonly used in this type of analysis. There is a lack of sensitivity at the compressional critical angle and a corresponding

peak in $|R|$. This is also the cause of the vertical banding features in Figure 5.7 (a) and (b) and a change in phase seen in (c) and (d) label (1).

The compressional critical angle feature is frequency-dependent due to the increasing significance of the thin mirror and spacer layers at shorter wavelengths. Considering individual plane waves of different frequencies incident on the sensor, long wavelengths will only ‘see’ the bulk sound speed of the substrate. However, for short wavelengths, the effective sound speed will be a combination of the spacer, the mirrors and substrate and there may be multiple compressional critical angles. This can be seen in Figure 5.8. As the frequency increases from 5 – 35 MHz there is a broadening of both the critical angle dip and reflection coefficient peak. This is illustrated further in Figure 5.9 which shows the modelled directivity and reflection coefficient for three frequencies over a small angular range between 14° – 18° . As the frequency changes from 0.1 – 100 MHz, the dip in the directional response associated with the compressional critical angle moves from 15.4° to 15.7° .

Immediately following the compressional critical angle, there is strong mode conversion into the shear mode. Less of the incident wave energy is reflected causing an increase in the magnitude of the displacements of the mirrors. This corresponds to a small peak in directivity which can be seen in Figure 5.7 (a) and (b) label (3).

After the shear critical angle $\theta_{cs} = 25^\circ$, the incident wave couples into an evanescent wave which decays exponentially from the surface. The surface displacement increases as the incident wave starts to couple into the leaky-Rayleigh mode at θ_r and decreases after. This can be seen as a rapid increase in sensitivity in Figure 5.8 (a) to (d) following the water-substrate shear critical angle when the reflection coefficient approaches unity. There is also a dip in the reflection coefficient after the shear critical angle. This is a result of adding a small value of attenuation to the model to help visually identify when the Rayleigh wave occurs. With no attenuation in the model, a leaky-Rayleigh wave is still present but all the energy from the Rayleigh wave is re-emitted into the coupling fluid, hence the magnitude of the reflection coefficient is equal to unity. By including absorption, some of the energy

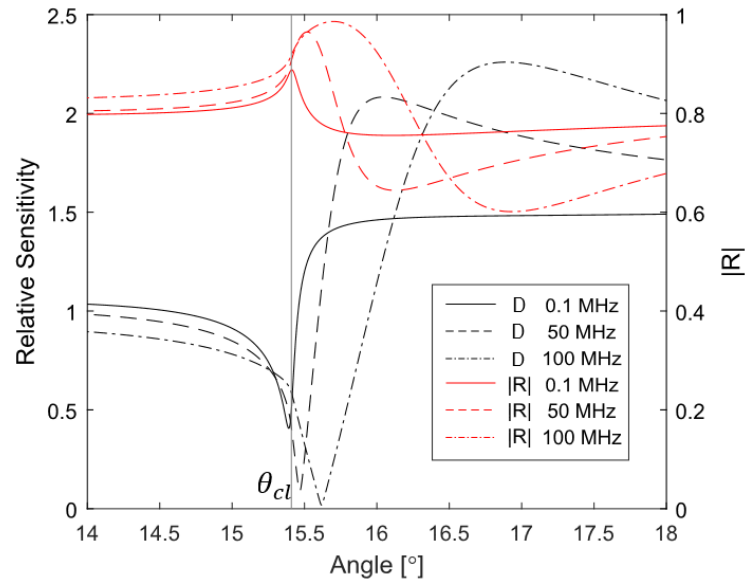


Figure 5.9: Critical angle separation in the hard-dielectric sensor. The modelled directivity and reflection coefficient have been plotted at three frequencies over a narrow angular range near the compressional critical angle between water and glass. The left vertical axis indicates the relative sensitivity of the directional response and the right vertical axis indicates the magnitude of the reflection coefficient. The gray vertical line indicates the critical angle between glass and water. A dip in the directional response is associated with the first critical angle and moves from 15.4° to 15.7° as the peak in the reflection coefficient broadens. Figure reprinted from [67] © IEEE 2019.

of the Rayleigh wave is absorbed, hence, the reflection coefficient is less than unity [1].

Air-backed cover-slip sensor: Like the hard-dielectric sensor, the air-backed cover-slip sensor has a minimum in the directional response at the compressional critical angle. This can be seen in the directivity profiles for the air-backed sensor in Figure 5.6. These have been plotted between 0° to 40° at 5 MHz intervals up to 40 MHz. The additional peaks and troughs, which can be seen in the profiles, are a result of Lamb modes and will be discussed in the following section.

5.5.3 Guided Wave Features

Lamb waves: The majority of the observable features of the air-backed cover-slip arise from the incident wave coupling energy into leaky-Lamb modes. Generally, the sensor has a low sensitivity at frequencies and angles where the incident wave couples into anti-symmetric modes. At frequencies and angles where the incident

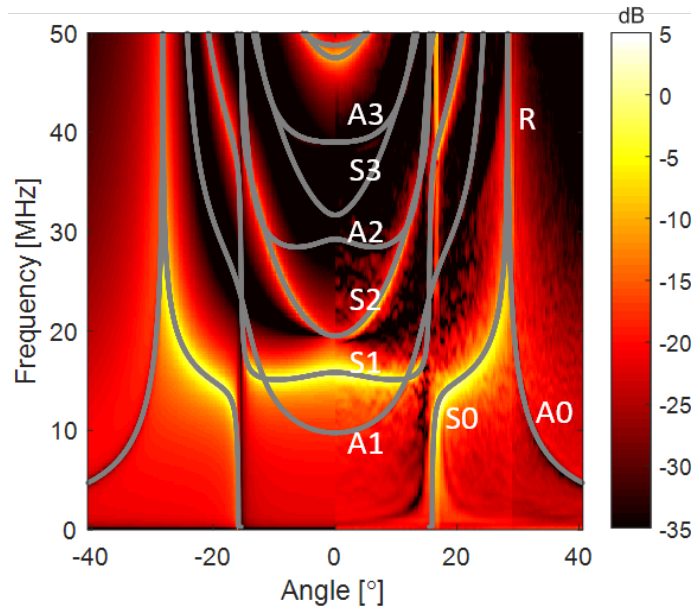


Figure 5.10: Modelled directivity between -40° to 0° , and measured directivity between 0° to 40° from 0 to 50 MHz for the air-backed cover-slip sensor. The color-scale has been plotted in decibels. The calculated dispersion curves have been plotted in gray and identified as symmetric (S) anti-symmetric (A) Lamb-modes and the Rayleigh mode (R). The guided wave modes present in the sensor cause a complex directional response. Note, the A1 dispersion curve in the measured data is precluded by the plotted modelled dispersion curves. Figure reprinted from [67] © IEEE 2019.

wave couples into symmetric Lamb modes the sensor has a high sensitivity. This is illustrated in Figure 5.10 which shows the dispersion curves for the glass plate plotted over the directivity. These have been labelled anti-symmetric (A), symmetric (S) and Rayleigh (R).

For anti-symmetric mode shapes, the vertical displacement at the top and bottom of the sensor are the same. As there is no change in the distance between the two mirrors, there is a null in the sensitivity. For a symmetric mode, the vertical displacements at the top and bottom of the sensor have the same magnitude but in opposite directions. This opposing movement results in a large difference in vertical displacement and thus a high sensitivity. For frequencies and angles that do not couple into a Lamb-mode, the displacement of the top and bottom surfaces will be somewhere between the symmetric and anti-symmetric mode and hence there is a gradual change in sensitivity between different modes. The mode shapes for the first and second order symmetric and anti-symmetric modes are plotted in Fig-

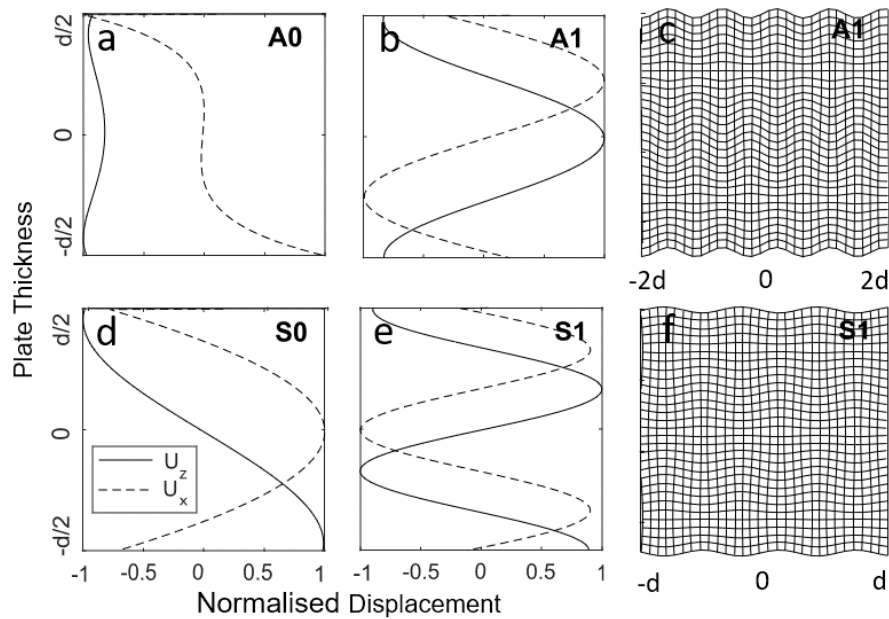


Figure 5.11: (a), (b), (d) and (e) The first and second order mode shapes of the symmetric and anti-symmetric Lamb waves present in the air-backed cover-slip sensor. The vertical (solid) and transverse (dashed) displacement across the thickness of the plate d have been plotted and normalized by the maximum displacement. For anti-symmetric modes the displacement at the top of the glass cover-slip is the same as the bottom. For symmetric modes the displacement at the top and bottom of the glass plate are out of phase. (c),(f) Visualization of the symmetric and anti-symmetric mode shapes. Figure reprinted from [67] © IEEE 2019.

ures 5.11 (a), (b), (d) and (e). Figures 5.11 (c), (f) demonstrate the shape of the glass cover-slip for the second order symmetric and anti-symmetric mode. Note, the displacement has been exaggerated for visualisation.

At normal incidence, the frequencies at which higher-order Lamb modes begin can be calculated as the resonant frequencies of the glass cover-slip. For a $175 \mu\text{m}$ thick cover-slip, the resonances from a compressional mode occur at approximately 16, 31, 47 MHz and from shear mode at 10, 19, 29, 48 MHz which can be seen in Figure 5.10. The lowest-order Lamb waves, S0 and A0 can be seen from the lowest frequencies and couple into the leaky-Rayleigh mode. The fundamental Lamb modes have been labelled Figure 5.10 and in Figure 5.6 (a) to (d). The Rayleigh mode is a common feature of both the hard-dielectric sensor and the air-backed cover-slip and will be discussed in the next section.

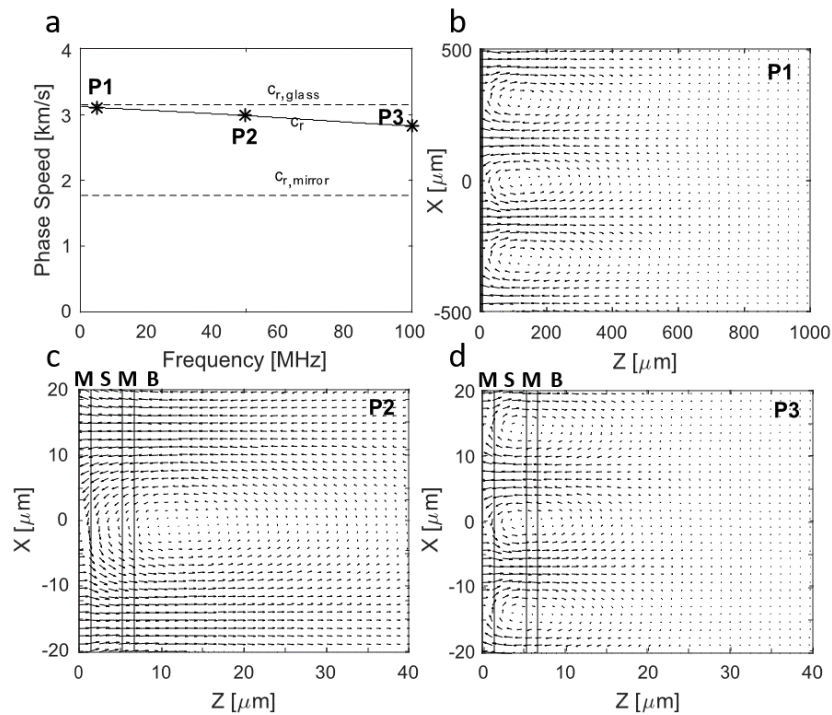


Figure 5.12: Rayleigh wave plots generated for the hard-dielectric sensor. (a) Leaky-Rayleigh wave phase speed (solid) with frequency. The Rayleigh speed for the glass substrate and the mirrors are also plotted (dashed). (b)-(d) Vector field plots at three points on (a). The horizontal axis represents the depth from the water-mirror interface in μm and the vertical axis is the position parallel to the interface. The vertical lines indicate the boundary between the mirror (M)-spacer (S) - mirror - backing (B). The vertical lines cannot be seen on (b) over the plotted depth. Figure reprinted from [67] © IEEE 2019.

Leaky-Rayleigh wave: Both the hard-dielectric and the air-backed cover-slip sensors have a feature of high sensitivity associated with a leaky-Rayleigh wave. This result agrees with measurements of the directional response of a similar sensor presented in [60].

The Rayleigh wave has an elliptical motion with the greatest displacement at the surface. As there is a large displacement at the surface, there is a difference in the vertical displacement between the mirrors causing a region of high sensitivity. This can be seen as a peak in the directivity which occurs immediately preceding the leaky-Rayleigh angle, θ_r , which is labelled in Figure 5.8 (a) to (d) and Figure 5.7 label (4) for the hard-dielectric sensor. This can also be seen for the cover-slip sensor after the A0 and S0 Lamb modes couple, Figure 5.6 (e) to (h), Figure 5.10

label R.

The leaky-Rayleigh wave for the air-backed cover-slip has a frequency-independent phase speed as the sensor is primarily constructed from a single material. The Rayleigh speed of glass is 3152 ms^{-1} , which can be found using the approximation $c_r/c_s = (0.862 + 1.14\nu)/(1 + \nu)$ [130], where ν is the Poisson's ratio of the material and c_r/c_s is the ratio of the Rayleigh and shear speed.

The hard-dielectric sensor has multiple elastic layers and the Rayleigh wave exhibits a frequency-dependent phase speed, shown in Figure 5.12 (a). The Rayleigh wave speed is generally close to the bulk shear speed of the material it is travelling in. At low frequencies, the wavelength of the leaky-Rayleigh wave is much larger than the spacer and mirrors and the majority of the wave motion occurs in the substrate, as shown in Figure 5.12 (b). At high frequencies, the wavelength is shorter and more motion occurs within the spacer and mirrors, as shown in Figure 5.12 (c) to (d). The leaky-Rayleigh wave speed starts at that of the glass-substrate (3152 ms^{-1}) and moves towards the Rayleigh speed of the mirrors and spacer (1780 ms^{-1}). The dispersion curve for the leaky-Rayleigh mode can be seen Figure 5.12 (a). At even higher frequencies (not shown here), higher order Rayleigh modes will appear [131, 132]. The displacement field plots, shown in Figure 5.12, also show elliptical motion for angles after the shear critical angle. However, the greatest sensitivity occurs at the Rayleigh angle, when the surface displacement is a maximum. There is a gradual decrease in sensitivity after the Rayleigh angle.

5.5.4 Other Features

Low sensitivity in the hard-dielectric sensor The peak in directivity associated with the leaky-Rayleigh wave is diminished by the crossing of the minimum highlighted in Figure 5.7 label (5). The displacement field within the sensor has an elliptical motion for angles larger than the shear critical angle. The depth of this motion into the sensor depends on the wavenumber component into the sensor (k_z). The value of this component gets smaller for both a higher frequency and a larger angle of incidence. As the angle is increased from the shear critical angle, the depth of the elliptical motion becomes shallower. The displacements of the mirrors change

from the top mirror having the larger displacement to the bottom mirror having the larger displacement. Through this transition there is an angle where both mirrors will have the same magnitude and are moving in phase. Here, there is no difference in the vertical displacement between the top and the bottom mirror and there is a null in the sensitivity. This is illustrated in Figure 5.13 where the magnitude and phase profiles of the directional response are plotted at 25 MHz. The minimum can be seen at 32° . There is also a discontinuity in phase as the magnitude is zero and a $-\pi$ change in phase as the second mirror has the larger displacement.

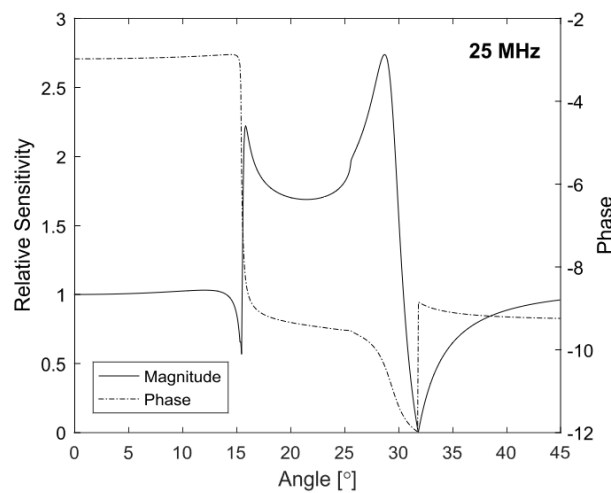


Figure 5.13: Relative sensitivity at 25 MHz for the hard-dielectric sensor. The solid line represents the magnitude of the difference in the complex mirror displacements and the dashed line indicates the phase. The minimum at 32° occurs when the mirrors have both the same absolute displacement and are in phase. Figure reprinted from [67] © IEEE 2019.

5.6 Influence of Strain-Optic Coefficients

5.6.1 Strain-Optic Coefficients

Previously in Section 5.4 and Figure 5.5 it was shown the inclusion of the strain-optic coefficients did not have a significant impact on the directional response for the air-backed glass cover-slip. However, it is of interest to know why this is the case and when it may become important. This is investigated further for the air-backed cover-slip in this section. The hard-dielectric sensor has not been investigated for two reasons. Firstly, the SOCs are not well known for the mirrors, and secondly,

it is possible the fitting of the mirror material properties has compensated for the strain-optic effect.

Profiles of the measured and modeled directional response for the cover-slip sensor at four frequencies are plotted in Figure 5.14. The profiles are normalized to the normal incidence frequency-response. As the directional response is symmetric about 0° the profiles have been plotted from 0° to 40° . Each sub-plot contains four profiles, the model without the SOCs (solid), the model including SOCs polarized in x (dashed) and y (dash-dotted) and the measured response (points).

Additionally, the modelled directivity profiles at 10 MHz have been plotted in Figure 5.15 for clarity in comparing the model with and without SOCs. The vertical dashed line at $\theta = 15.4^\circ$ corresponds to the compressional wave critical angle between water and glass.

At the critical angle there is only a compressional wave traveling perpendicular to the interfaces within the glass cover-slip. If the SOCs are excluded, the directional response is only dependent on the vertical displacement of the mirrors. At the critical angle there is no vertical displacement and therefore a minima in the response (this was discussed in Section 5.5.2). This can be seen in Figure 5.15 (solid line). When the SOCs are included, the sensor is sensitive at the critical angle as there is a transverse strain component which effectively shifts the minima associated with the critical angle towards 0° . This can be seen in Figure 5.15 (solid black and dashed lines). The minima is shifted to the left as the transverse strain component increases, peaking at the fundamental symmetric mode, S_0 which is excited just after the critical angle. The Lamb modes produce large normal and transverse strains within the cover-slip when they are excited. This can be seen in Figure 5.16 which shows the normal (a) and transverse (b) strain components integrated over the cover-slip thickness. These terms are important in the directivity equation, Eq. (5.2).

In the directivity equation, the p_{12} coefficient is multiplied by the integral of the normal strain over the thickness of the sensor. This is equivalent to taking the difference in the vertical displacement of the mirrors. Hence, if p_{12} is large and p_{11}

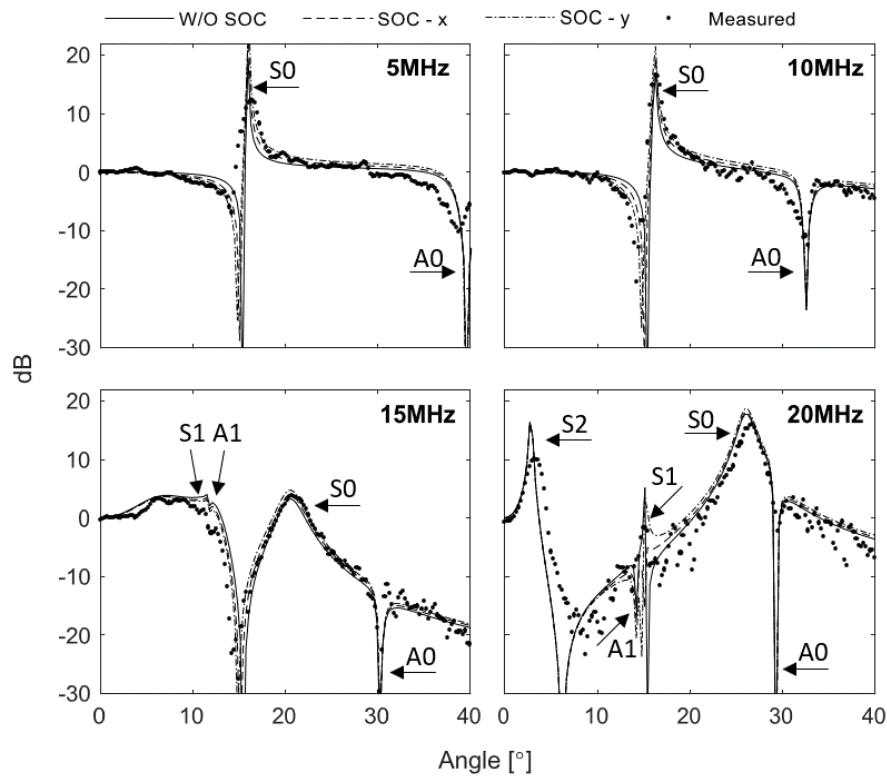


Figure 5.14: Enlarged plot of Figure 5.6 (a)-(d). Profiles of the measured and modeled directional response at four frequencies: 5 MHz, 10 MHz, 15 MHz and 20 MHz. Profiles of the measured data (points), modeled directivity excluding (solid) and including the SOCs have been plotted (polarized in x - dashed, polarized in y - dash-dotted). Features in the directional response correspond to the fundamental and higher-order symmetric (S) and anti-symmetric (A) Lamb modes. Figure reprinted from [122] © IEEE 2019.

is small (tending to zero), the directivity after normalisation will be the same as just taking the difference in vertical displacement of the mirrors. The p_{11} coefficient is multiplied by the integral of the transverse strain over the thickness of the sensor. As mentioned previously, the minima associated with the critical angle appears shifted. These results indicate the strain-optic effect may not be significant for materials with large p_{12} coefficients but will be most pronounced in materials with large p_{11} coefficients. Additionally, the impact of the strain-optic effect is different for an oblique angle of light, as demonstrated in [60].

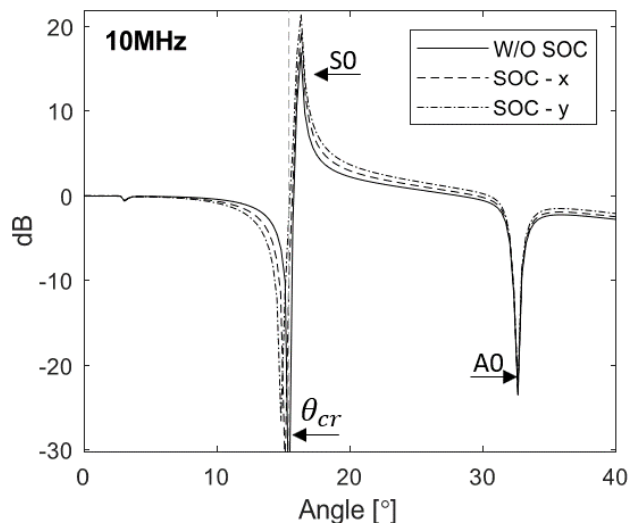


Figure 5.15: Profiles of the modeled directional response at 10 MHz. Modeled directivity excluding (solid) and including the SOCs have been plotted (polarized in x - dashed, polarized in y - dash-dotted). Figure reprinted from [122] © IEEE 2019.

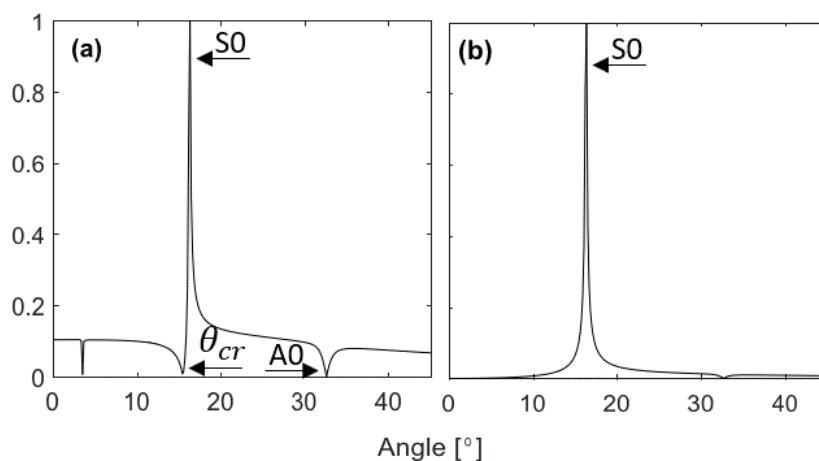


Figure 5.16: (a) Integral of the normal strain component over the spacer thickness, $\int (\partial u_z / \partial z) . dz$. (b) Integral of the transverse strain component over the spacer thickness, $\int (\partial u_x / \partial z) . dz$. The profiles have been normalized to the maximum value. Figure reprinted from [122] © IEEE 2019.

5.6.2 Discussion

The isotropic elastic multilayered model of the directional response of planar Fabry-Pérot ultrasound sensors introduced in Section 5.1 agrees well with the measurements of directivity as discussed in Section 5.4. However, it should be noted that this model may not be applicable for every Fabry-Pérot ultrasound sensor. First, the dominant transduction mechanism is considered to be the difference in dis-

placement of the two mirrors and, for the analysis of the features, the strain-optic mechanism was neglected. However, when including the strain-optic effect for the spacer in the model of the directional response, see Figure 5.5 (c) and Figure 5.14, there were minimal changes in the directivity. Additionally, the strain-optic coefficients are not well-known nor easily measured for thin-films. For other Fabry-Pérot sensors the strain-optic effect could contribute more significantly to the directional response. However, it does not affect the frequency and angle the features in the directional response occur due to guided modes, but could affect the amplitude response.

Second, the model assumes each elastic layer is infinitely long and planar and the model displacement is constrained to the (x, z) plane, which explicitly excludes bulk horizontally polarized shear waves. Although horizontally polarized shear modes do not affect the vertical displacement of the mirrors, they may have an influence on the refractive index of the material, which may be important in materials with large strain-optic coefficients.

The geometry of the sensors in this study is simple, effectively consisting of a few elastic layers, and the majority of features are associated with critical angles or Lamb and Rayleigh modes. Other Fabry-Pérot sensors may be constructed from multiple elastic layers. The features in the directivity of these sensors will be different and include other types of guided modes. Additionally, the SOCs for each material may have to be considered in the transduction mechanism [60, 51].

The materials used for the Fabry-Pérot sensors may have a significant impact on the strain-optic effect. Soft-polymer Fabry-Pérot sensors commonly use Parylene C and PMMA as the substrate and spacer materials. The SOCs of PMMA can be seen in Table 5.2. Note the $p_{11} = 0.3$ and is larger than the equivalent SOC of glass. Values for Parylene C SOCs are not known, however, if they are similar to PMMA the strain-optic effect would be more pronounced for soft-polymer planar sensors than glass sensors. Additionally, the acoustic and optical properties of thin films are not always well known and can often be optically or acoustically anisotropic. Acoustically anisotropic materials might increase the transverse strain

and the effect of the p_{11} coefficient. For example, a plane acoustic wave at normal incidence could cause a transverse motion in anisotropic media. For optically anisotropic materials there are additional terms in the Δn equation, for a laser beam parallel to z and polarized in x

$$\Delta n = -\frac{1}{2}n_0^3 \left(p_{11} \frac{\partial u_x}{\partial x} + p_{12} \frac{\partial u_z}{\partial z} + p_{15} \frac{\partial u_z}{\partial x} \right). \quad (5.3)$$

The additional term introduces the shear-strain into the directivity equation $\partial u_z/\partial x$ and multiplies it by the p_{15} SOC. Further study is needed to accurately determine the optical and acoustic properties of the materials used in other Fabry-Pérot sensors, to have greater certainty into how significant the strain-optic effect is.

5.7 Summary

In this chapter, the `ElasticMatrix` toolbox was used to model the frequency-dependent directional response of planar glass-etalon Fabry-Pérot ultrasound sensors. The model was compared with measurements made with an air-backed cover-slip and an all-hard dielectric sensor. The main features in the directivity were described as effects of physical wave phenomena such as compressional and shear critical angles, Lamb modes and Rayleigh modes. The model had good agreement with measured data both with and without the inclusion of the SOCs. This suggests that the strain-optic effect is not significant for glass cover-slip sensors. However, this may not be true for all types of Fabry-Pérot sensors, for example, soft-polymer sensors.

Chapter 6

Soft-Polymer Sensors

6.1 Introduction

In Chapter 5, the directional response of two glass etalon sensors was investigated. The modelled and measured data had good agreement and the directional response features were mostly associated with critical angles and guided modes. Other types of Fabry-Pérot sensors use soft-polymers as spacer materials, in particular Parylene C. These are more sensitive than an equivalently sized glass spacer. This can be understood by considering the magnitude of displacement of a spacer material made from a soft polymer or glass. If both spacers have the same thickness and the incident wave is the same pressure, the soft polymer will deform more than the glass material. Since the sensitivity of the sensor is dependent on the rate of change of the optical phase difference between the two mirrors, a greater deformation causes a greater phase change and hence a greater sensitivity. Some material properties of Parylene have been collated in Table 6.1.

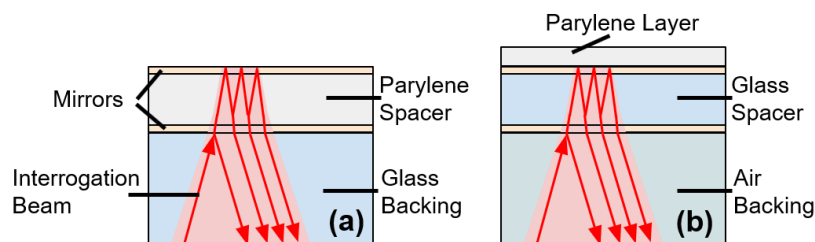


Figure 6.1: (a) Diagram of a soft-polymer sensor with a glass backing. (b) Diagram of a glass cover-slip sensor with a layer of Parylene C. Note, the Parylene layer is not optically interrogated in this configuration.

Table 6.1: Table of Parylene C properties.

Ref	Density [kg/m ³]	c_L [m/s]	c_S [m/s]	Impedance [MRayls]	E [GPa]	ν
[133]	1289	2142 ¹	-	2.8	-	-
[134]	1289	2050.3 ²	878 ²	-	2.760	0.388
[7]	1180	2200	1100	-	-	-
[135]	1288	2135 ± 85	-	2.75	-	-
[136]	1100	2350 ¹	-	2.58	-	-
[137]	-	-	-	-	3.1 to 5.4	-

c_L and c_S are the compressional and shear speed respectively. E is the Young modulus and ν is the Poissons ratio. ¹These values were calculated using the impedance and density. ²These values were calculated from the Youngs modulus and Poisson ratio and density.

The material values used by Cox [7] ($c_L = 2200$ m/s, $c_S = 1100$ m/s, $\rho = 1100$ kg/m³) were used to model a soft-polymer sensor consisting of a Parylene C spacer (≈ 60 μ m), glass backing and hard-dielectric mirrors. A relatively thick spacer was purposefully chosen as features in the directivity caused from guided waves would occur over a narrower bandwidth. This is beneficial for validating the acoustic model. A diagram can be seen in Figure 6.1 and the measured and modelled directional response can be seen in 6.2 and Figure 6.3. The hard-dielectric mirrors were not modelled here as the exact thickness and material properties are unknown. Additionally, they are typically an order of magnitude thinner than the spacer and therefore the directional response is dominated by the properties of the Parylene spacer and backing material. The model has been plotted with and without the inclusion of the strain-optic coefficients. The strain-optic coefficients are not known for Parylene C and the coefficients for PMMA were used instead. The strain-optic coefficients for PMMA were used for a number of reasons. Firstly, there is little data for the strain-optic coefficients of polymers, however, PMMA has similar strain-optic coefficients to other polymers [138]. Secondly, the stiffness coefficients of PMMA is closer to Parylene than glass [138, 125, 126]. There is poor agreement between the model and the measurements. A dashed grey line has been added to the figures to indicate the location of a bright region caused by a guided mode. The mode appears in different places in the measured and modelled data which

indicate the material properties are incorrect. It is worth noting that the strain-optic coefficients do not alter the location of the features that are caused by guided modes, as these are governed by the elastic properties of the sensor. However, the strain-optic coefficients can affect the amplitude of the features and where some minima occur.

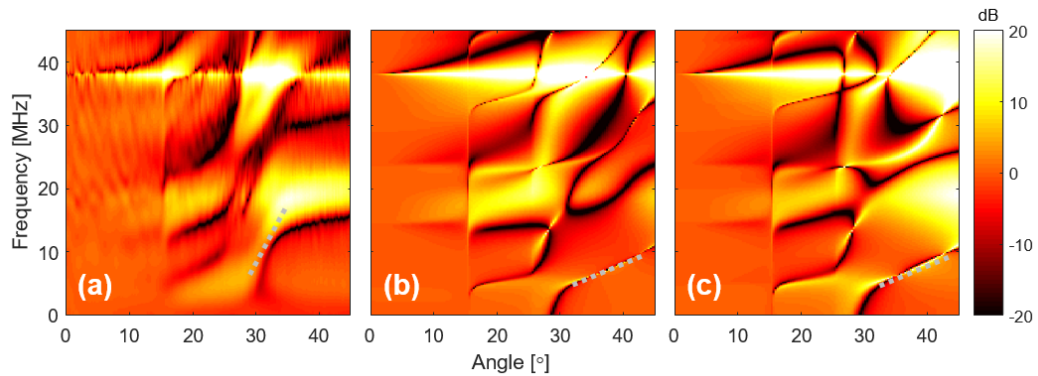


Figure 6.2: (a) Measured directional response of a soft-polymer sensor with a glass backing. The data has been normalised to the normal-incident frequency response. (b) Modelled directional response using isotropic values of Parylene but excluding the strain-optic effect. (c) Modelled directional response using isotropic values of Parylene and including the strain-optic effect with the coefficients from PMMA. A grey line has been added to each figure which is representative of the location of a dispersion curve. This is in a different place in the modelled and measured data indicating that the material properties of Parylene are incorrect.

In this instance, the strain-optic coefficients have a large effect on the directional response. This is because the p_{11} coefficient used (PMMA, $p_{11} \approx 0.3$) is much larger than that used in glass $p_{11} \approx 0.12$, hence there is a larger influence from the transverse strain term in the directional response equation.

As the strain-optic parameters are not known, the influence of these parameters on the directional response may be significant. In an attempt to separate the optical and acoustic modelling problem, a layer of Parylene ($26 \mu\text{m}$) was deposited on the air-backed cover-slip sensor from Chapter 5 (a diagram can be seen in Figure 6.1). This meant the optical cavity included only the glass cover-slip. However, the directional response is affected as the Parylene layer alters the dispersion characteristics of the guided modes.

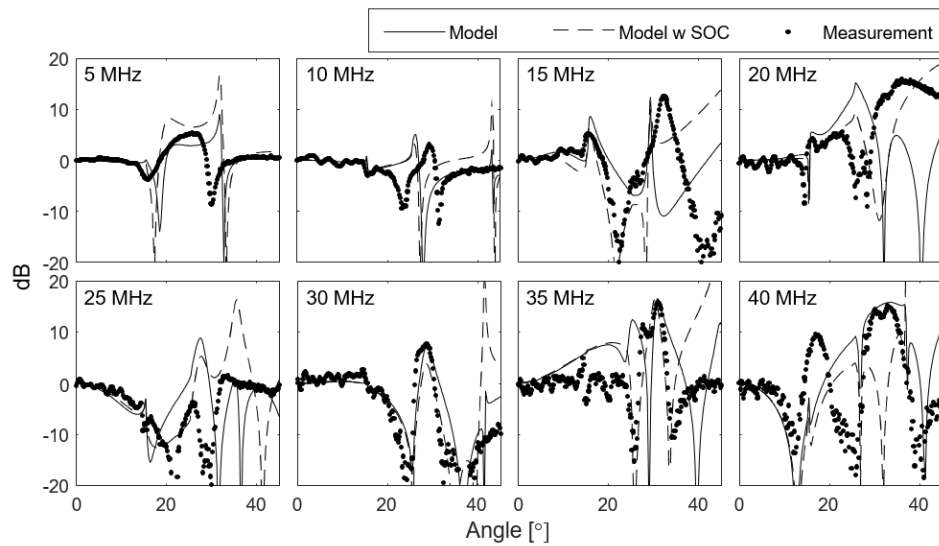


Figure 6.3: Profiles of the directional response of a soft-polymer sensor. The data has been normalised to the normal-incident frequency response. There is poor agreement with the measured and modelled data.

The measured and modelled directional responses are shown for the coated cover-slip sensor in Figure 6.4 and Figure 6.5. It appears as if the material properties for Parylene are incorrect. This can be clearly seen by focusing on the guided mode highlighted with a dashed grey line in Figure 6.4. This mode corresponds to an anti-symmetric leaky-Lamb mode in the glass cover-slip. The dispersion characteristic of this mode is modified by the presence of Parylene. Hence, it occurs at a different frequency and angle in the measurement when compared with the model. However, it is worth noting that the features at angles $< 10^\circ$ do have good agreement. This suggests that the shear properties of Parylene might be incorrect (there is very little data on this property), or that Parylene might be anisotropic such that the wave speed in the transverse axis is different than in the normal axis. The properties of Parylene are investigated further in Section 6.3.

6.2 Evidence for Crystal Structure

6.2.1 Deposition of Parylene

A brief description on the deposition process of Parylene is given here to facilitate the following discussion. Parylene C (and other Parylene variations) is a polymer

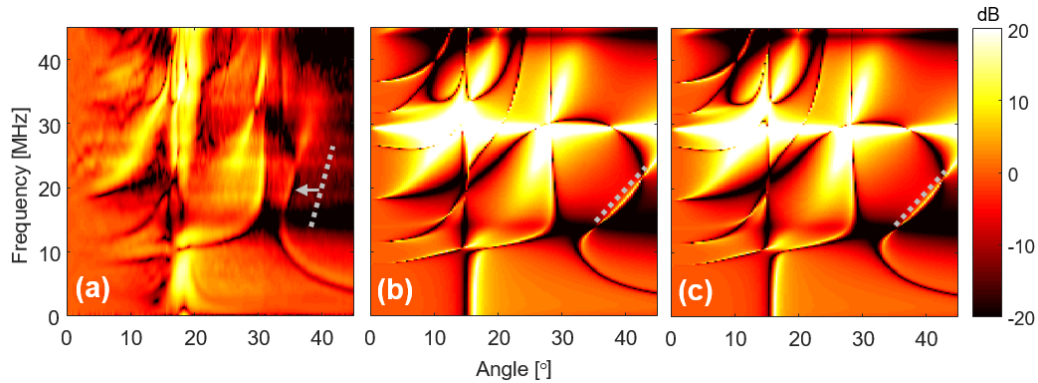


Figure 6.4: (a) Measured directional response of a Parylene coated cover-slip sensor with an air backing. In this sensor, the optical cavity only includes the glass cover-slip. Note, the banding artifacts which occur between 15° to 20° are caused by clipping of the oscilloscope which did not have sufficient dynamic range. The data has been normalised to the normal-incident frequency response. (b) Modelled directional response using isotropic values of Parylene but excluding the strain-optic effect in the cover-slip. (c) Modelled directional response using isotropic values of Parylene and including the strain-optic effect in the cover-slip. A grey line has been added to each figure which is representative of the location of a dispersion curve. This is in a different place in the modelled and measured data indicating that the material properties of Parylene are incorrect. A banding artefact in (b) and (c) at 30 MHz is caused from the modelled data being normalised to the normal incidence frequency response.

which is deposited through vacuum deposition (Speciality Coating Systems, Indianapolis). The raw material, the dimer, is heated under a vacuum where it vaporises into a gas. A dimer is made from two monomers bonded by a weak or strong covalent or inter-molecular bonds. The vaporised dimer is pyrolyzed, which cleaves the bonds of dimer leaving it in a monomeric form [139]. The gas is passed into the deposition chamber where it deposits on all the surfaces while simultaneously polymerizing [140]. The thickness of the coating is dependent on the time the substrate is in the deposition chamber. However, there are a number of other factors which can affect the coating. For example, the preparation of the substrate, the rate of deposition, the temperature and the pressure. The Parylene C used in Fabry-Pérot sensors is deposited at room temperature. These factors lend themselves to creating a thin (angstroms to millimeters) and uniform “pin-hole” free coating. The uniformity, control of the thickness, and optical properties are what makes Parylene a good choice for Fabry-Pérot spacers.

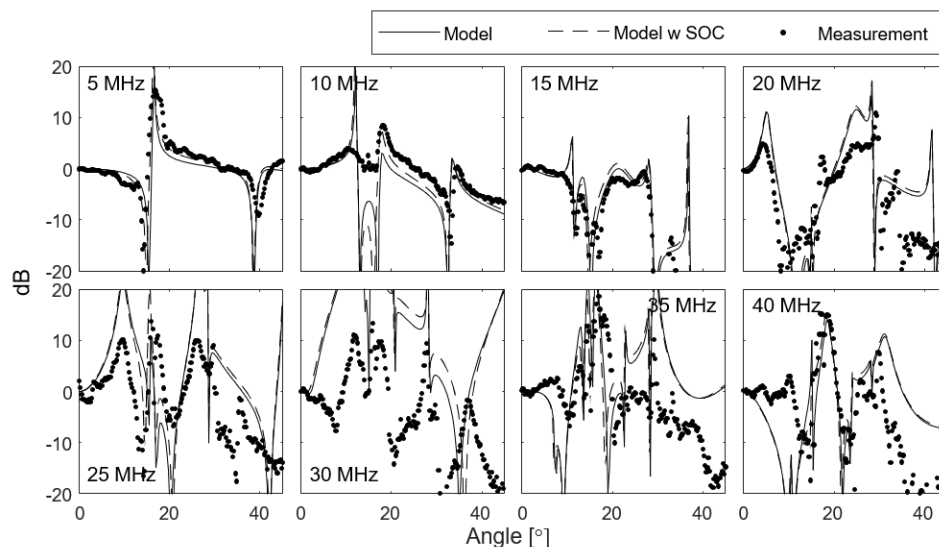


Figure 6.5: Profiles of the directional response of a Parylene coated cover-slip sensor. The data has been normalised to the normal-incident frequency response. There is poor agreement with the measured and modelled data.

6.2.2 X-ray Diffraction and Electron Microscopy Measurements

The structure of Parylene was investigated with X-ray diffraction and electron microscopy measurements. If Parylene has an ordered crystal structure it may indicate anisotropy. X-ray diffraction can be used to determine if a material has a crystal structure and the orientation of the crystal planes. A sample is deposited on a substrate, and a beam of monochromatic x-rays are fired at a range of oblique angles to the sample. The beam may reflect off the sample surface, or enter the sample lattice which diffracts the beam. The beam is diffracted differently by the sample if the atoms or molecules are arranged in a periodic way.

A 25 μm sample of Parylene C was deposited on glass and was measured with the help of Martin Vickers (Inorganic Chemistry Section, University College London). The results of this measurement and a similar result from literature [140] is plotted in Figure 6.6. In the measurement there is a broadband peak corresponding to Parylene C at an angle of 14° . There is a similar peak in the literature measurement occurring at 12° . The discrepancy in angle is due to different photon energies. The broadband peak indicates Parylene does have some structure and periodicity. If

Parylene was amorphous there would not be a peak in the measurement. Note, in the measurement from literature, the Parylene sample was deposited on a silicon substrate. The silicon is also structured and has corresponding peaks in the diffraction measurement, whereas there are none in our measurement as glass is amorphous.

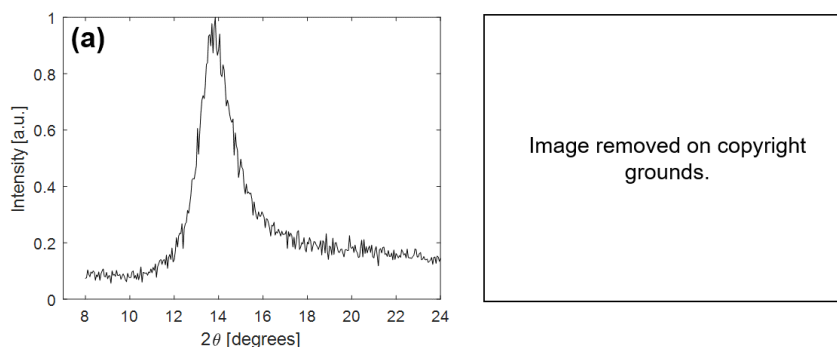


Figure 6.6: (a) X-ray diffraction measurement taken with the help of Martin Vickers (Inorganic Chemistry Section, University College London). (b) A similar result seen by Tan, this figure has been reproduced from [140].

The diffraction measurement from the literature is for Parylene at different thicknesses (from $0.32 \mu\text{m}$ to $120 \mu\text{m}$), and shows an increase in intensity of the diffraction peak with the thickness of Parylene. This indicates that the thicker the sample of Parylene, the more crystalline it becomes. Further measurements from Tan suggested that the Parylene chains fold over one another to form column-like or fibre structure. An illustrative diagram can be seen in Figure 6.7 (d). This result is corroborated by measurements from Jackson who investigated the effect of annealing temperature on the crystallinity of Parylene thin films [137]. Jackson found that Parylene was crystalline when annealing at room temperature. Additionally, annealing at a higher temperature increased the crystallinity of the material up-to the melting point of Parylene. Jackson provided scanning-electron microscope (SEM) images and showed the annealed Parylene had very clear fibre structures. This can be seen in Figure 6.7 (a) to (c).

Transmission electron microscope (TEM) images of Parylene were taken to investigate if our samples also had a fibrous structure. A $500 \mu\text{m}$ sample of Parylene was prepared over multiple runs (and months) by Edward Zhang and Jamie Guggenheim (Photoacoustic Imaging Group, University College London) and TEM images

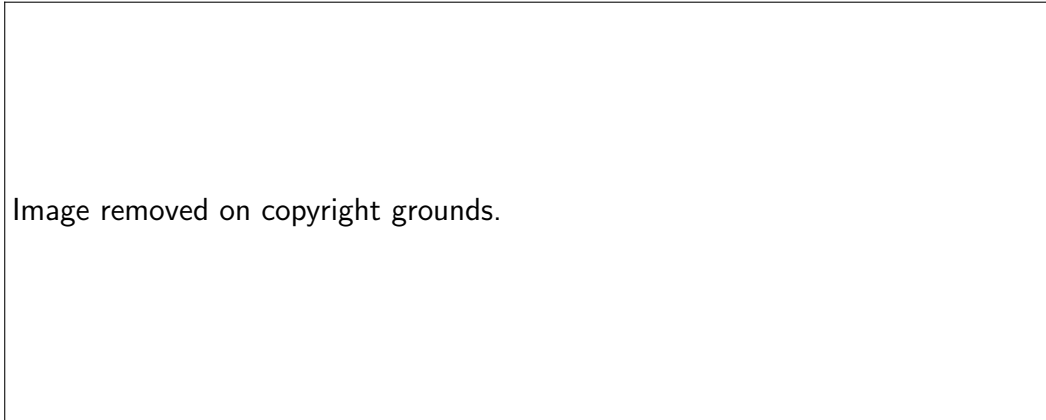


Figure 6.7: (a) Cross section SEM images of unannealed Parylene. (b) Cross section SEM images of annealed Parylene at 150° . There are clear column-like structures in the Parylene sample. The black bars represent a scale of $10\ \mu\text{m}$. (c) X-ray diffraction results at different annealing temperatures. These show similar results to Figure 6.6. (d) A diagram to show Parylene chains folder over to grow into column like crystals during deposition. (a), (b) and (c) have been partially reproduced from [137]. (d) has been partially reproduced from [140].

were taken by Jan Laufer and Sylvia Goerlitz (Institut für Physik, Martin-Luther-Universität Halle-Wittenberg). These can be seen in Figure 6.8.

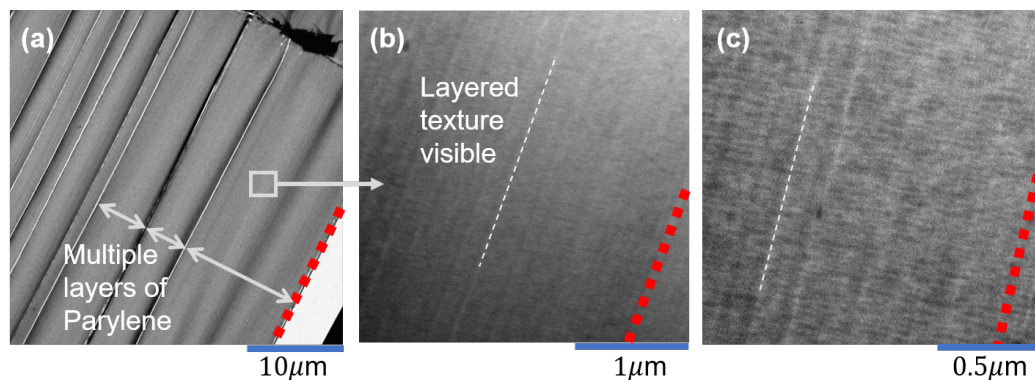


Figure 6.8: (a) TEM image of a thick Parylene sample made from multiple runs. Each individual run can be seen and some have been labelled. The red dashed line indicates the orientation of substrate backing. (b) A zoomed section of one of the Parylene layers. There appears to be layered structures oriented with the substrate. A white line has been added to help visualise the lines. (c) Same as (b) but zoomed-in further. These measurements were taken by Jan Laufer and Sylvia Goerlitz (Institut für Physik, Martin-Luther-Universität Halle-Wittenberg).

A dashed red line has been added to the images to indicate the location of the substrate backing as in some images the sample is in a different orientation. There

are multiple straight lines which occur from different runs of Parylene. Focusing in on a single run of Parylene, there is a layered structure which is physical property of the Parylene samples. This is present in all of the Parylene layers. The structure appears to be a different orientation to the fibre structures shown in the previously described literature, and is parallel to the substrate ([140, 137]). It is not known what causes this structure.

There are noticeable gaps at the interfaces between multiple runs of Parylene deposition, which indicates Parylene may have poor adhesion to itself. Discussion in the literature agrees with this, for example, “Parylene suffers from poor adhesion to itself and noble metals, such as gold and platinum, a considerable drawback in the implementation of Parylene for bioMEMS. The adhesion of Parylene devices, which consist of thin films of Parylene-metal-Parylene sandwiches, is compromised when devices are soaked in wet environments” [141]. Some Fabry-Pérot sensors consist of mirrors made from noble metals with Parylene C spacers, and some thick Parylene spacers are constructed from multiple runs of Parylene deposition. Although not directly related to the material properties, this introduces new problems in the modelling process. When modelling the multilayered structure, it is assumed the normal and transverse stress and displacement are continuous across interfaces between different elastic materials. If there is poor adhesion, the perfect boundary conditions assumed before may not be true, however, it does not necessarily mean a new modelling technique is required. Imperfect boundary conditions can be modelled by introducing a thin, modelling layer with artificial properties [84]. Additionally, adhesion problems will cause instabilities of the sensor performance and sensitivity over time due to water ingress. This may be a practical restriction for the use of Fabry-Pérot sensors.

Although the acoustic and mechanical properties of Parylene are not determined through these methods, the layered or columnated structure may point to acoustic anisotropy in the Parylene C depositions used in Fabry-Pérot sensors, similar to how these structures give rise to anisotropy in the earths crust in seismological applications.

6.3 Determining Material Parameters

6.3.1 Physical and Optical Measurement of Thickness

To accurately model Parylene sensors it is important to determine all the correct parameters. The simplest parameter to measure is the spacer thickness. This measurement was taken optically and physically. The two different techniques were used to ensure the sensors thicknesses used in the modelled directional response were accurate. The optical measurements of thickness uses the free spectral range, which is the distance between two adjacent minima in the interferometry transfer function. The length of the undeformed Fabry-Pérot cavity can be calculated as follows

$$l = \frac{\lambda_0^2}{2\Delta\lambda n_i}, \quad (6.1)$$

where l is the cavity length, λ_0 is the centre wavelength, $\Delta\lambda$ is the free spectral range, and n_i is the refractive index of the spacer material. The measured ITF for a glass-backed polymer sensor can be seen in Figure 6.9. The calculation for the cavity length is

$$l = \frac{(1550 \times 10^{-9})^2}{2 \times (19 \times 10^{-9}) \times 1.64}, \quad (6.2)$$

$$= 38.5 \mu\text{m}. \quad (6.3)$$

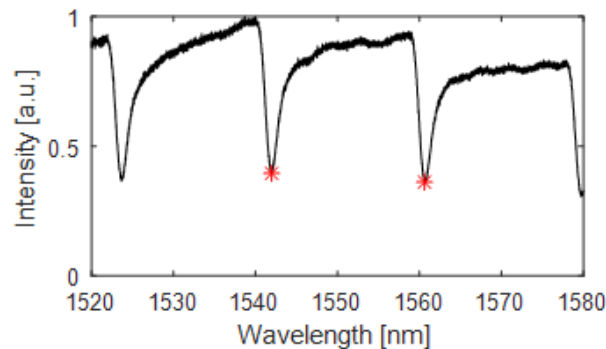


Figure 6.9: ITF of a soft-polymer sensor, two red stars have been added. These correspond to the bottom of the fringe.

A physical measurement of the spacer thickness was performed using a pro-

Table 6.2: Table of Parylene C thickness measurements.

Serial Number	Measurement	Mean (μm)	ITF (μm)
L50AL2 ¹	barrier + spacer	41.8 ± 0.3	38.3 ± 1.0
H50AL1 ¹	barrier + spacer	42.8 ± 0.4	38.7 ± 1.0
H50AL1 ¹	spacer	39.9 ± 0.5	38.7 ± 1.0
hdie4ab ²	barrier + spacer	63.2 ± 0.3	62.2 ± 2.64

¹Parylene spacer with thin aluminium mirrors (estimated $< 0.01 \mu\text{m}$) deposited on a glass substrate. ²Parylene spacer with hard-dielectric (estimated 2 to 4 μm) mirrors deposited on a glass substrate. Some indicated profilometer measurements include a barrier coating (estimated to be 1 to 2 μm). ITF measurements are just of the cavity and use a refractive index of $n = 1.64$ [139].

filometer DektakXT, Bruker Massachusetts, US) with the help of Srinath Rajagopal (National Physical Laboratory, Teddington). The samples were secured in a mount within the device and a diamond tip stylus was brought down to touch the surface of the material. The stylus traces in a straight line along the surface of the sample and measures height variations to within 1 nm when set to the 65 μm height range. Figure 6.10 contains an example of the analysis used to determine the thicknesses. The height data was imported into MATLAB, and the data points were thresholded to eliminate points where the spacer had detached from the substrate. The data was clustered into two groups with k-means. This was done to automate analysis as there were multiple measurements taken for each sensor. The results from the profilometer and ITF measurements can be found in Table 6.2. The predicted thicknesses derived from the ITF were within a few microns of the physical thickness measurements. Discrepancies arise in the ITF measurements as the sensors are low finesse which make it difficult to estimate the bottom of the fringe. Additionally, the profilometer was only accurate to 0.83 μm . In any case, a variation in the estimated thickness of a few microns from the ITF will have a negligible change on the observable features of the directional response as the sensors investigated here are tens of microns in thickness.

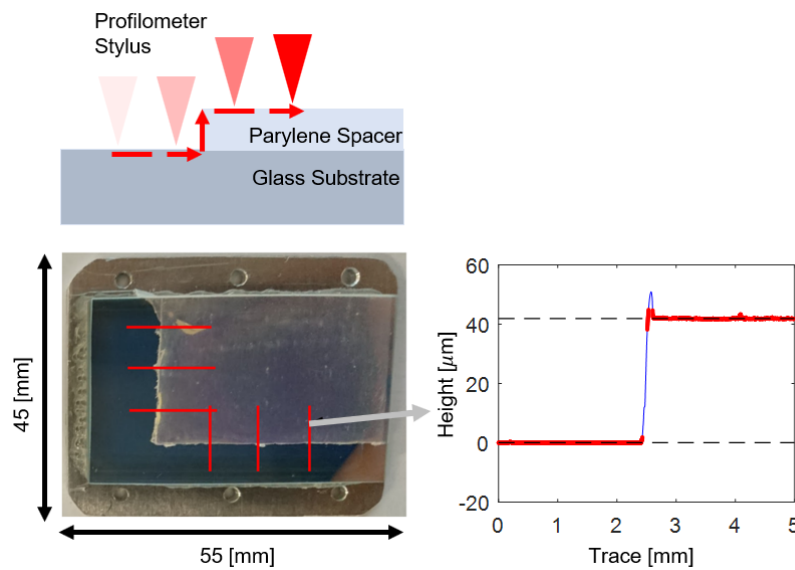


Figure 6.10: Profilometer measurement of a Parylene spacer. The Parylene coating was partially removed from the substrate. A profilometer stylus is traced across a region with and without Parylene. The difference in height of the stylus indicates the thickness of the Parylene spacer. These measurements were taken with the help of Srinath Rajagopal (National Physical Laboratory, Teddington).

6.3.2 Acoustic Impedance Measurement

Acoustic impedance measurements of Parylene were taken to determine the degree of anisotropy of Parylene and obtain some material parameters. Two samples were prepared by Edward Zhang (Photoacoustic Imaging Group, University College London). These consisted of a $40.5 \mu\text{m}$ layer of Parylene deposited on a PMMA substrate in a single run and a $(18.9 + 20.2) \mu\text{m}$ layer of Parylene deposited on a PMMA substrate in two runs. The impedance was measured with a scanning acoustic microscopy setup by Kay Raum and Urszula Zabarylo (Charité, Universitätsmedizin Berlin). The technique estimates the impedance with the reflection coefficient from the sample with a focused 200 MHz transducer in pulse echo-mode [142, 143]. There were two measurements taken. The first measurement was from the top (normal-incidence), which effectively measures the C_{33} coefficient of the stiffness matrix. In the second measurement, the samples were cut and placed on top of one another to give a Parylene layer of $\approx 80 \mu\text{m}$. The samples were polished flat and an impedance measurement was taken from the side, which effectively gives

C_{11} of the stiffness matrix (90° incident). An illustrative diagram can be found in Figure 6.11 (a) and (b).

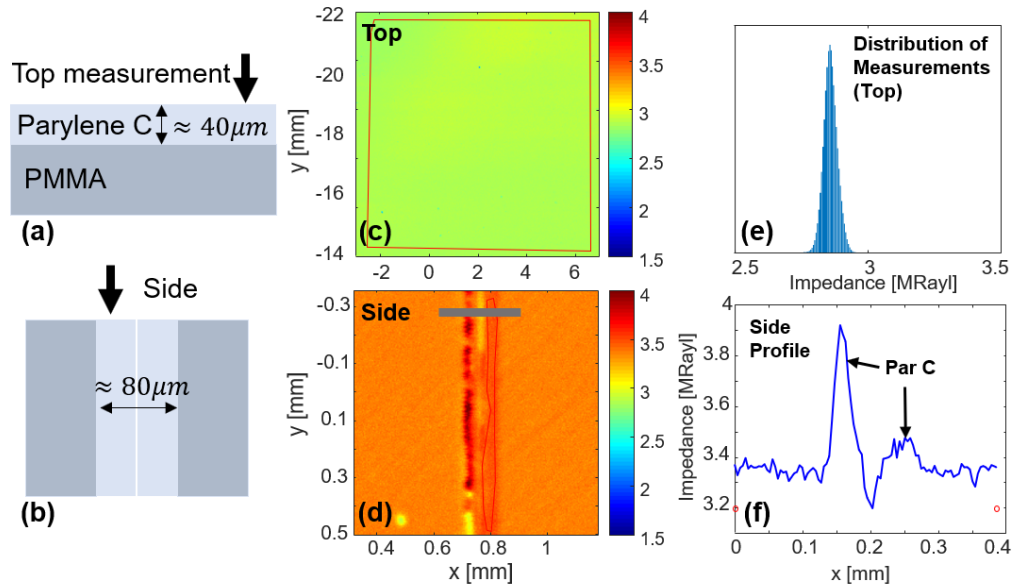


Figure 6.11: Diagram of the top and side measurements for Parylene C. (a) A $40\ \mu\text{m}$ layer of Parylene is deposited on a PMMA substrate and impedance measurements are taken from the top. (b) The sample is cut in two and the two Parylene coatings are put together. An impedance measurement is then taken from the side. (c) The impedance scan from a measurement of the top of the sample, this has a uniform impedance. (e) The distribution of impedance values has been plotted in the top right. (d) The impedance scan from the side of the sample. The impedance scan from the side also captures the PMMA backing, the region of higher impedance in the centre of the image is from Parylene. (f) A profile of the impedance scan indicated as the grey line in (e), which shows two impedance peaks corresponding to Parylene. The measurements were taken by Kay Raum and Urszula Zabarylo (Charité, Universitätsmedizin Berlin).

The top surface measurement of Parylene provided an impedance of approximately 2.85 MRayl. The side measurement of Parylene provided an impedance of > 3.4 MRayl. The results are summarised in Table 6.3. It was not possible to get an accurate side measurement of Parylene in every measurement due to difficulties in preparing a flat measurement surface. When Parylene was visible it appeared to have a much higher impedance than when measured from the top. This indicates strong anisotropy, however, the uncertainty in the measurements was not quantified.

Table 6.3: Table of Parylene C impedance measurements.

Sample Test	Top [MRayl]			Side [MRayl]		
	Mean	Median	std	Mean	Median	std
One - 1	2.868	2.866	0.044	-	-	-
One - 2	2.842	2.843	0.023	> 3.4 ¹	-	-
One - 3	2.840	2.841	0.022	> 3.4 ¹	-	-
Two - 4	2.861	2.860	0.027	-	-	-
Two - 5	2.827	2.829	0.021	-	-	-
Two - 6	2.758 ²	2.759 ²	0.042	> 3.4 ¹	-	-
PMMA				3.355	3.357	0.032

¹Impedance appears higher than PMMA substrate. ²Reduced impedance due to sample tilt. “One” and “two” refers to the 40 μm sample coated in a single or two depositions. It was not possible to fully quantify the uncertainty for all of the measurements. Data collected by Kay Raum and Urszula Zabarylo (Charité, Universitätsmedizin Berlin).

6.4 Directivity with Measured Parameters

6.4.1 Parylene Coated Cover-Slip

The measured properties were used to investigate if the modelled directional response had better agreement with the measured response shown in Figure 6.12. It was assumed that Parylene is transversely-isotropic. This seems like a reasonable assumption as the literature suggests Parylene deposits in column or fibre structures and the TEM images showed Parylene having a layered structure. A transverse-isotropic material is described with five parameters using the method shown in Chapter 3. With the notation from the previous Chapters, these are the density and four stiffness coefficients, $C_{11}, C_{33}, C_{13}, C_{55}$. The impedance measurements can be related to the stiffness coefficients with the following formula

$$C_{11} = \frac{Z_{\text{side}}^2}{\rho}, \quad (6.4)$$

$$C_{33} = \frac{Z_{\text{top}}^2}{\rho}, \quad (6.5)$$

where Z is the measured impedance from the side or the top, and ρ is the density of Parylene. The values used were $Z_{\text{top}} = 2.85$ MRayl, $Z_{\text{side}} = 3.45$ MRayl, with density taken as the average of the values given in literature $\rho = 1229$ kg/m³ (shown

in Table 6.1). The mean side-impedance of the smaller peak of Parylene was chosen as it was believed the height of the taller peak was an artefact. This leaves two unknown parameters, C_{13} and C_{55} . As the impedance measurement of Parylene from the side was measured at > 3.45 MRayl, which is close to PMMA (3.355 MRayl), the values for C_{55} and C_{13} were estimated by taking the average of the literature values of (isotropic) Parylene and PMMA giving $C_{13} = 3.58$ GPa and $C_{55} = 1.73$ GPa.

Firstly these values were assigned to the model and compared with the measurements for the Parylene coated cover-slip. The results can be seen in Figure 6.12 and Figure 6.13. The dispersion curve that has been highlighted with the dashed grey line has much better agreement between the model and the measured data compared with Figure 6.4. This is more clearly demonstrated in Figure 6.14, which has the dispersion curves calculated from the model. The feature that was highlighted previously in Figure 6.4 now has a good fit with the dispersion curve. This belongs to the fundamental anti-symmetric Lamb mode of the glass plate which has different dispersion characteristics from the presence of the Parylene layer. The dispersion curves plotted belong to Lamb-like modes. There is a bright band at 30 MHz in the modelled data which is caused by the normalisation of the model to the normal-incidence frequency response.

6.4.2 Soft-Polymer Sensor

The anisotropic material properties for Parylene were used to model the soft-polymer sensor (previously shown in Figure 6.2). The modelling was performed with and without the strain-optic effect. The results can be seen in Figure 6.15 and Figure 6.16. Similarly to the Parylene coated cover-slip, the dispersion curve highlighted with the dashed grey line has moved. Qualitatively, there appears to be better agreement. However, the strain-optic coefficients make a significant difference to the directional response for this sensor. Without measured values for these it is difficult to model the sensor accurately. The dispersion curves have been calculated and plotted in Figure 6.17.

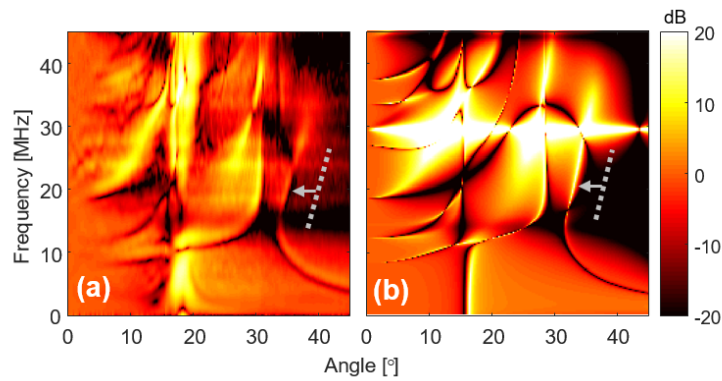


Figure 6.12: (a) Measured directional response of a Parylene coated cover-slip sensor with an air backing. In this sensor only the glass cover-slip is optically interrogated. Note, the banding artifacts which occur between 15° to 20° are caused by clipping of the oscilloscope which did not have sufficient dynamic range. The data has been normalised to the normal-incident frequency response. (b) Modelled directional response using anisotropic values of Parylene but excluding the strain-optic effect in the cover-slip.

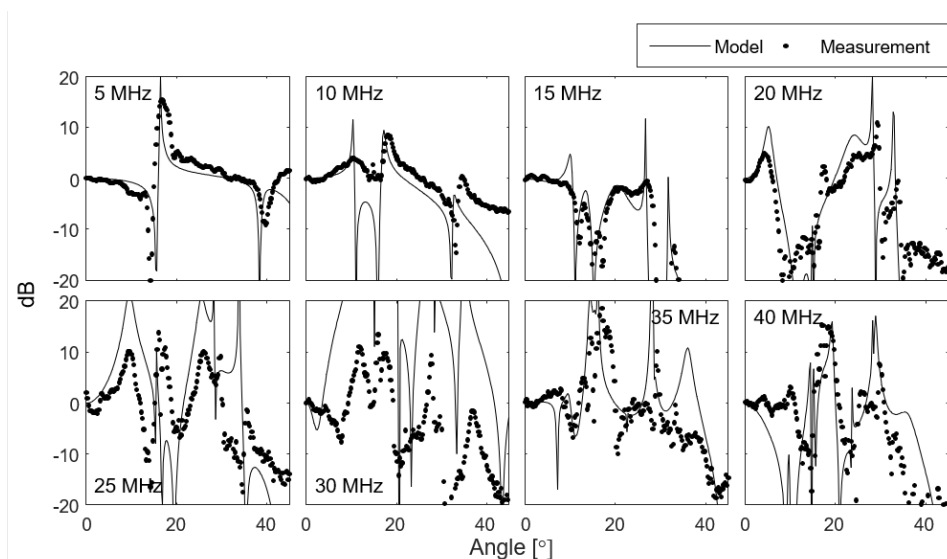


Figure 6.13: Profiles of the directional response of a Parylene coated cover-slip sensor. The data has been normalised to the normal-incident frequency response. The modelled profile at 30 MHz has poor agreement with the measured data as it is normalised by an almost-zero value in the normal-incidence response.

6.4.3 Discussion

Although the anisotropic model had better agreement with the measurements, the result is not as convincing for the Parylene C sensors as is with the glass sensors.

There may be a number of reasons why the agreement is not as good. There is

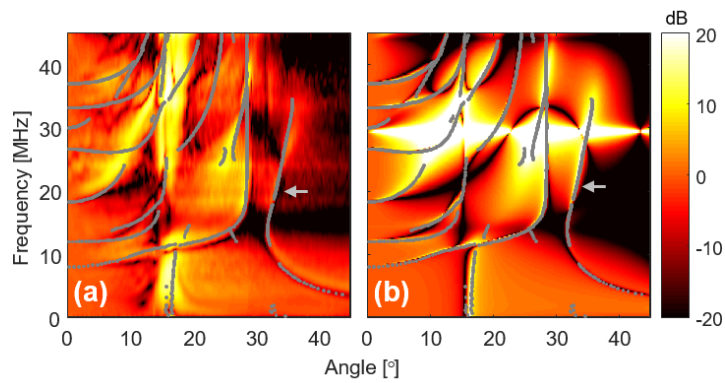


Figure 6.14: This figure is the same as Figure 6.12 with the dispersion curves calculated from the model.

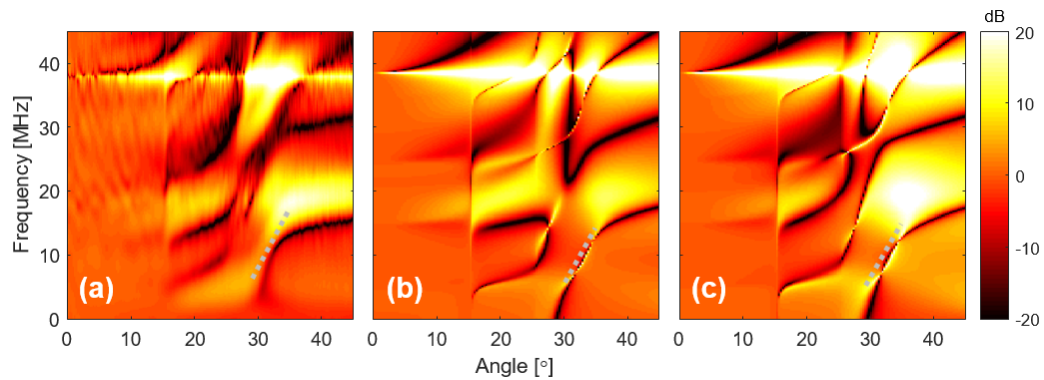


Figure 6.15: (a) Measured directional response of a soft-polymer sensor with a glass backing. The data has been normalised to the normal-incident frequency response. (b) Modelled directional response using anisotropic values of Parylene but excluding the strain-optic effect. (c) Modelled directional response using anisotropic values of Parylene and including the strain-optic effect with the coefficients from PMMA. A grey line has been added to each figure which is representative of the location of a dispersion curve. Qualitatively, there is much better agreement compared to Figure 6.2.

still a lack of certainty in the C_{11} stiffness coefficient as it was not possible to properly prepare the Parylene sample and get multiple measurements from the side. The directional response of the Parylene sensors will be most sensitive to this stiffness parameter as it will change the phase speeds of guided modes, especially at large oblique angles. However, the preliminary impedance measurements are somewhat validated by the improved agreement of the dispersion curves in the Parylene coated cover-slip.

Impedance measurements should be repeated to verify the anisotropy of Pary-

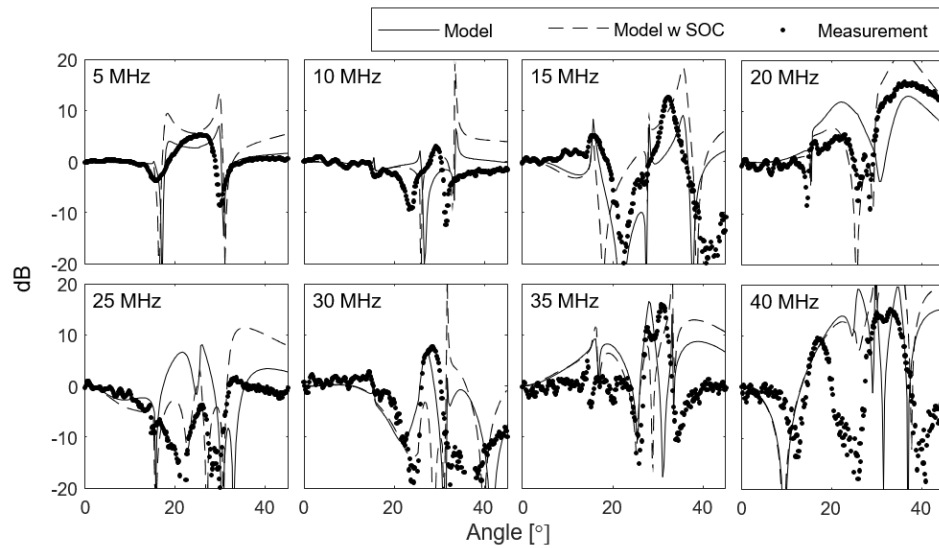


Figure 6.16: Profiles of the directional response of a soft-polymer sensor. The data has been normalised to the normal-incident frequency response. There is better agreement with the modelled and measured data.

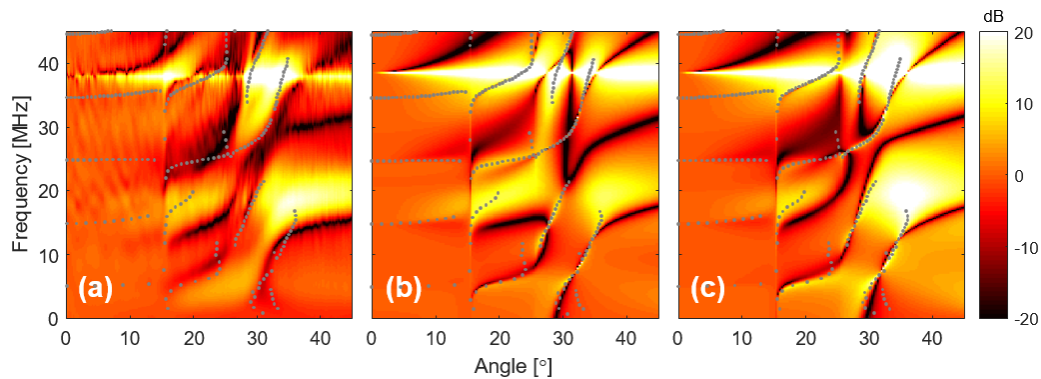


Figure 6.17: Same as Figure 6.15 with the dispersion curves calculate from the model.

lene. Additionally, measurements should be done for Parylene samples of different thicknesses and deposited on different substrates or air-backed measurements. This is because all these different factors have been shown to adjust the crystallinity and material structure of Parylene which will in turn alter the stiffness properties and strain-optic coefficients [140].

To progress further it may be necessary to fully measure the strain-optic parameters of Parylene. One method suggested by Borelli uses a transparent material deposited on a piezoelectric substrate which makes up one arm of a Mach-Zehnder interferometer [124, 144]. The piezoelectric substrate resonates and gives rise to

a time-varying interference pattern in the sample. The strain-optic coefficients can be determined from this by polarising the interferometer light in two perpendicular orientations, measuring the change in refractive indices and then solving for the strain-optic coefficients [124]. One caveat to this method is that the material stiffness-matrix of Parylene must be known first. Additionally, this method was used to solve for the p_{11} and p_{12} coefficients which is sufficient at describing an optically isotropic material. If Parylene is birefringent (which it has been shown to be) [69] it may mean that more strain-optic coefficients are needed to describe the model.

Additionally, there may be other factors to take into consideration, for example, if Parylene has debonding issues and if there is significant material absorption. The change in phase speed of the guided modes (in particular the fundamental anti-symmetric leaky-Lamb mode highlighted previously) occur from the adhesion of Parylene to the substrate and the necessity of the boundary conditions at the interfaces. If there was a significant debonding, the phase-speed of the mode would not be modified so greatly and it would be expected that the fundamental anti-symmetric Lamb mode couples with the fundamental symmetric Lamb mode as was shown in Chapter 5. Material absorption was considered, but only tested in the isotropic case. Adding compressional and shear absorption had no effect on the dispersion characteristics of the guided waves but only reduced their amplitude.

6.5 Summary

This chapter investigated the material properties of Parylene C. Prior to this work it was believed Parylene C had isotropic properties. However, there was little data on the acoustic properties and there was poor agreement with model and measurement when using isotropic properties of Parylene. From impedance measurements it appears as though Parylene is anisotropic and the improvement of the directional response and the improved alignment of the dispersion curves seem to support this. The impedance results were not conclusive and further work needs to be done to accurately determine the material properties such as the strain-optic coefficients.

Chapter 7

General Conclusions

The planar Fabry-Pérot ultrasound sensor offers an alternative to traditional piezoelectric sensors for clinical and metrological applications. It is able to detect ultrasound over a broadband frequency range (tens of MHz) and can be made with small element sizes (tens of microns) [28]. This sensor is frequently used in photoacoustic imaging, as a reference sensor for hydrophone calibration, and can also be used for general ultrasound field characterisation [59, 49, 60, 7, 28, 61, 50, 62, 19].

For a planar Fabry-Pérot sensor interrogated by a sufficiently small spot size, the directional response is dominated by the complex wave-field within the sensor caused by the interaction of elastic waves with the multilayered structure of the sensor. This is different to piezoelectric sensors which are mostly affected by spatial averaging. In this thesis, a model of the frequency-dependent directional response was developed based on the partial-wave method, treating the sensor as a multilayered elastic structure.

The directional response of the Fabry-Pérot sensor is dependent on both a change in displacement of the mirrors and a change in refractive index of the spacer. The change in displacement and change in refractive index was found by modelling the propagation of elastic-waves via the partial-wave method. This was explained in Chapter 3. The partial-wave method description in this thesis can describe elastic wave propagation in isotropic, transverse-isotropic and orthotropic media. The matrix formulation allows the partial-wave amplitudes of the first layer to be related to the last. The wave amplitudes can be used to calculate the stresses and displace-

ments at any coordinate within the sensor and consequently calculate the directional response.

The partial-wave method was developed into an open-source MATLAB toolbox called `ElasticMatrix`. These types of methods have had a significant impact on different areas of acoustics, such as non-destructive evaluation and geophysics. Though these methods are still relevant today, there is no open-source or easily accessible implementation. `ElasticMatrix` fills this gap and is implemented with an object-oriented framework. This makes the toolbox easy to use, develop and expand. It allows students and scholars to easily develop new algorithms and to take advantage of the features of MATLAB. The toolbox is capable of calculating and plotting reflection and transmission coefficients, slowness profiles, dispersion curves and displacement and stress fields. An additional MATLAB class is included to model the frequency-dependent directional response of planar Fabry-Pérot ultrasound sensors. A description of the MATLAB toolbox, the implementation and validation examples were given in Chapter 4.

In Chapter 5, the model was validated, tested and compared with directional response measurements made on two glass-etalon sensors: an air-backed cover-slip sensor with well-known acoustic properties and an all-hard-dielectric sensor. The main features in the directivity were described as effects of physical wave phenomena such as compressional and shear critical angles, Lamb modes and Rayleigh modes. The model had good agreement with measured data both with and without the inclusion of the strain-optic coefficients. This suggests that the strain-optic effect is not significant in describing the directivity for glass cover-slip sensors. This is because one term in the strain optic coefficient is the same as the difference in displacement of the the mirrors. However, this may not be true for all types of Fabry-Pérot sensors.

In Chapter 6, Parylene C, a spacer material commonly used in soft-polymer sensors, was found to exhibit anisotropic acoustic properties. Using measured anisotropic properties of Parylene for the model gave better agreement to measurements compared with isotropic properties. However, the uncertainty in the

impedance measurements was not quantified and determining the exact stiffness-matrix coefficients should be the subject of future work. This chapter also revealed potential problems with Parylene C as a spacer material for Fabry-Pérot sensors. For example, it has problems with self-adhesion and delamination. This is not only useful information for Fabry-Pérot sensors, but Parylene is used in MEMS devices and many other industries.

Knowledge of the physical mechanisms affecting the frequency-dependent directional response of the planar Fabry-Pérot sensor can be used to inform the design of future sensors (e.g., see [7, 50]). For example, to increase the measurable bandwidth, the thickness of the spacer layer can be reduced. By ensuring the spacer thickness is much less than the shortest wavelength to be measured, the sensor will have a relatively flat frequency response. The trade-off to this is a reduction in sensitivity, as the displacement difference will be smaller for a thinner spacer compared to a thicker spacer of the same material. However, the reduction in sensitivity could be improved by increasing the finesse of the Fabry-Pérot sensor [19]. Reducing the spacer thickness will also move the guided wave features to higher frequencies. Another change that can be made to ameliorate the effect of guided wave features is to make the compressional and shear sound speeds of the sensor materials closer to the compressional wave speed of the coupling fluid. This will move critical angle features further from normal incidence. Indeed, when the sound speed of the sensor is less than that of the fluid there will be no critical angle, giving the sensor a more omnidirectional response. For example, Fabry-Pérot sensors consisting of a thin polymer spacer on a polymer backing material exhibit a flat frequency-response with few significant features in the directivity [31]. The trade-off is that these sensors are less robust to high intensity ultrasound.

The investigations in this thesis were focused on planar Fabry-Pérot sensors that are deposited on large flat substrates or are free standing. There are different configurations of Fabry-Pérot sensors discussed in Section 1.3.3.3. The elastic model presented in this thesis is applicable for describing large planar sensors and plano-concave sensors deposited on a planar substrate. The plano-concave sensors

can be modelled because the domes are encased to give an acoustically flat structure. For these types of sensors, if the material properties are well known, it is possible to perform detailed analysis based on the tools presented in this thesis such as tracing dispersion curves and reflection and transmission coefficients. Sensors which are deposited on optical fibers and other geometries may need different modelling approaches such as the finite-difference or finite element method. This is because the interaction of the acoustic wave with the finite structure becomes important, for example, vibrations of the tip in fibre-optic hydrophones. Additionally, sensors which are thin compared to the smallest acoustic wavelength may not require modelling of the complex elastic behaviour as the strain over the spacer and mirror materials can be considered constant.

There are a number of assumptions about the optical mechanism which may need further consideration. For example, the interrogation beam is assumed to have a Gaussian or collimated profile and assumed to be normally incident to the sensor. For beams which are not normally incident or have different profiles, the directivity mechanism will be different. This comes from a different impact of the strain-optic coefficients [60, 61]. In this thesis, the mirrors of the Fabry-Pérot sensors were modelled using the “two effective interfaces” technique, [60]. To properly account for the effect of the dielectric mirrors a rigorous multi-layered optical model is needed. However, the main limitation in modelling the directional response of Fabry-Pérot sensors is difficulties in measuring the acoustic and optical material properties of thin films.

To take the results from this thesis further and apply it to finite sensors such as fibre-optic hydrophones, rigorous optical modelling combined with more sophisticated elastic models, such as finite-element will be necessary.

Appendix A

Derivation of Beam Profiles

A.1 ‘Top-hat’ Beam Profile

For a ‘top-hat’ profile of radius a the spot is [7]

$$S = 1 \quad \text{for } -a \leq x < a \quad (\text{A.1})$$

$$= 0 \quad \text{elsewhere.} \quad (\text{A.2})$$

Omitting the time-dependent factor $e^{-i\omega t}$, for a ‘top-hat’ becomes

$$S = \frac{1}{2a} \int_{-a}^a e^{i\zeta x} dx = \frac{\sin(\zeta a)}{\zeta a}, \quad (\text{A.3})$$

where ζ is the horizontal wavenumber. Conversion into polar coordinates with $x = r \cos \phi$ and $dx = r dr$

$$S = \frac{1}{\pi a^2} \int_0^a \int_0^{2\pi} e^{i\zeta r \cos \phi} r d\phi dr. \quad (\text{A.4})$$

Here, the integral is between 0 and a as it is from the centre of the beam. The normalising factor is $1/\pi a^2$ as this is the area of a spot. Evaluating this function using Hankel transform pairs [145]

$$S = \frac{2}{a^2} \int_0^a J_0(\zeta r) r dr = \frac{2J_1(\zeta a)}{\zeta a}. \quad (\text{A.5})$$

A.2 Gaussian Beam

The spot $S(x)$ is defined as a Gaussian function with a maximum of 1

$$S(x) = e^{-x^2/(2\sigma^2)}, \quad (\text{A.6})$$

where σ is the standard deviation of the distribution. Setting the value of t to zero, neglecting the $\exp\{-i\omega t\}$ term leaves the function as

$$S = \frac{\int_{-\infty}^{\infty} e^{i\xi x} e^{-x^2/(2\sigma^2)} dx}{\int_{-\infty}^{\infty} e^{-x^2/(2\sigma^2)} dx}. \quad (\text{A.7})$$

Conversion into cylindrical coordinates can be seen below, see [7] for justification

$$S = \frac{\int_0^{\infty} \int_0^{2\pi} e^{i\xi r \cos \phi} e^{-r^2/(2\pi\sigma^2)} r d\phi dr}{\int_0^{\infty} \int_0^{2\pi} e^{-r^2/(2\pi\sigma^2)} r d\phi dr}. \quad (\text{A.8})$$

Evaluation of the bottom integral (the normalization factor) can be found using a standard result

$$\int_0^{\infty} \int_0^{2\pi} e^{-ar^2} r d\phi dr = \frac{\pi}{a}, \quad (\text{A.9})$$

hence if $a^{-1} = 2\pi\sigma^2$ this leads to

$$\int_0^{\infty} \int_0^{2\pi} e^{-r^2/(2\pi\sigma^2)} r d\phi dr = 2\pi^2\sigma^2. \quad (\text{A.10})$$

Eq. (A.8) now becomes

$$S = \frac{1}{2\pi^2\sigma^2} \int_0^{\infty} \int_0^{2\pi} e^{i\xi r \cos \phi} e^{-r^2/(2\pi\sigma^2)} r d\phi dr. \quad (\text{A.11})$$

Eq. (A.11) can be evaluated over ϕ by rearranging

$$S = \frac{1}{2\pi^2\sigma^2} \int_0^{\infty} \left(e^{-r^2/(2\pi\sigma^2)} r \left(\int_0^{2\pi} e^{i\xi r \cos \phi} d\phi \right) \right) dr. \quad (\text{A.12})$$

Integrating the parameters depending on ϕ gives a Bessel function of zero order, where J_0 is the Bessel function

$$\int_0^{2\pi} e^{i\zeta r \cos \phi} d\phi = 2\pi J_0(\zeta r), \quad (\text{A.13})$$

Eq. (A.12) now becomes

$$S = \frac{2\pi}{2\pi^2\sigma^2} \int_0^\infty e^{-r^2/(2\pi\sigma^2)} J_0(\zeta r) r dr. \quad (\text{A.14})$$

The following integral can be determined using Hankel transformation pairs. The Hankel transformation can be written as

$$F_0(\zeta) = \int_0^\infty F(r) J_0(\zeta r) r dr, \quad (\text{A.15})$$

using the Hankel transform pair

$$f(r) \Rightarrow F_0(\zeta) \quad (\text{A.16})$$

$$e^{-\frac{1}{2}a^2 r^2} \Rightarrow \frac{1}{a^2} e^{-\frac{\zeta^2}{2a^2}}, \quad (\text{A.17})$$

$$a^2 = \frac{1}{\pi\sigma^2}, \quad (\text{A.18})$$

$$e^{-\frac{1}{2}\frac{1}{\pi\sigma^2}r^2} \Rightarrow \pi\sigma^2 e^{-\frac{1}{2}\pi\sigma^2\zeta^2}, \quad (\text{A.19})$$

substitution of this result into A.14 gives

$$S = \frac{2\pi \cdot \pi\sigma^2}{2\pi^2\sigma^2} e^{-\frac{1}{2}\pi\sigma^2\zeta^2}, \quad (\text{A.20})$$

the coefficients cancel leaving

$$S = e^{-\pi\sigma^2\zeta^2/2}. \quad (\text{A.21})$$

For a plane wave at zero incidence $\zeta = 0$ and $S = 1$, however at any other incidence angle, ζ becomes non-zero and S decreases exponentially. For a small spot size the effect of spatial averaging is negligible.

Appendix B

Publications, software and awards

B.1 Publications

B.1.1 Journal

1. Ramasawmy, Danny R., et al. “ElasticMatrix a MATLAB toolbox for anisotropic elastic wave propagation in layered media.” Accepted with minor revision (2019).
2. Ramasawmy, Danny R., et al. “Analysis of the Directivity of Glass Etalon Fabry-Pérot Ultrasound Sensors.” IEEE transactions on ultrasonics, ferro-electrics, and frequency control, IEEE, (2019).

B.1.2 Conference

1. Ramasawmy, Danny R., et al. “The influence of strain-optic coefficients on the transduction mechanism of glass etalon Fabry-Pérot sensors” 2019 IEEE International Ultrasonics Symposium. IEEE, (2019).
2. Ramasawmy, Danny R., et al. “ElasticMatrix - An open-source partial-wave model for evaluating elastic-wave propagation in transverse-isotropic layered media” 2019 IEEE International Ultrasonics Symposium. IEEE, (2019).
3. Ramasawmy, Danny R., et al. “Directivity of a planar hard-dielectric Fabry-Pérot optical ultrasound sensor.” 2017 IEEE International Ultrasonics Symposium. IEEE, (2017).

B.2 Software

1. `ElasticMatrix`

Repository link - github.com/dannyramasawmy/ElasticMatrix

B.3 Awards

1. **2019** - Best presentation style, UCL Medical Physics PhD showcase.
2. **2017** - Best poster prize at CDT Summer School in Medical Imaging, London.
3. **2017** - Best student paper prize winner in the Sensors and NDE category at the IEEE International Ultrasonics Symposium, Washington DC.
4. **2017** - Travel award to International Ultrasonics Symposium, Washington DC.

Bibliography

- [1] J.D.N. Cheeke. *Fundamentals and applications of ultrasonic waves*. CRC Press, 2010.
- [2] K. S. Suslick. Sonochemistry. *science*, 247(4949):1439–1446, 1990.
- [3] K. Wear, C. Baker, and P. Miloro. Directivity and frequency-dependent effective sensitive element size of needle hydrophones: Predictions from four theoretical forms compared with measurements. *IEEE Trans. Ultrason. Ferroelect. Freq. Contr.*, 65(10):1781–1788, 2018.
- [4] J.A. Guggenheim, J. Li, T. J. Allen, R. J. Colchester, S. Noimark, O. Ogunlade, I. P. Parkin, I. Papakonstantinou, A. E. Desjardins, E. Z. Zhang, et al. Ultrasensitive plano-concave optical microresonators for ultrasound sensing. *Nat. Photonics*, 11(11):714, 2017.
- [5] E. Martin, E. Z. Zhang, J. A. Guggenheim, P. C. Beard, and B. E. Treeby. Rapid spatial mapping of focused ultrasound fields using a planar fabry–pérot sensor. *IEEE Trans. Ultrason. Ferroelect. Freq. Contr.*, 64(11):1711–1722, 2017.
- [6] B. Zeqiri, W. Scholl, and S. P. Robinson. Measurement and testing of the acoustic properties of materials: a review. *Metrologia*, 47(2):S156, 2010.
- [7] B. T. Cox and P. C. Beard. The frequency-dependent directivity of a planar Fabry–Pérot polymer film ultrasound sensor. *IEEE Trans. Ultrason. Ferroelect. Freq. Contr.*, 54(2), 2007.

- [8] A. Hurrell and S. Rajagopal. The practicalities of obtaining and using hydrophone calibration data to derive pressure waveforms. *IEEE Trans. Ultrason. Ferroelect. Freq. Contr.*, 64(1):126–140, 2017.
- [9] V. Wilkens, S. Sonntag, and O. Georg. Robust spot-poled membrane hydrophones for measurement of large amplitude pressure waveforms generated by high intensity therapeutic ultrasonic transducers. *J. Acoust. Soc. Am.*, 139(3):1319–1332, 2016.
- [10] P. M. Morse. Ku ingard, theoretical acoustics. *Princeton University Press*, 949p, 4:150, 1968.
- [11] A. R. Selfridge, G. S. Kino, and B. T. Khuri-Yakub. A theory for the radiation pattern of a narrow-strip acoustic transducer. *Appl. Phys. Lett.*, 37(1):35–36, 1980.
- [12] B. Delannoy, H. Lasota, C. Bruneel, R. Torguet, and E. Bridoux. The infinite planar baffles problem in acoustic radiation and its experimental verification. *J. Appl. Phys.*, 50(8):5189–5195, 1979.
- [13] K. Wear and S. Howard. Directivity and frequency-dependent effective sensitive element size of a reflectance-based fiber-optic hydrophone: Predictions from theoretical models compared with measurements. *IEEE Trans. Ultrason. Ferroelect. Freq. Contr.*, 65(12):2343–2348, 2018.
- [14] K. Wear, C. Baker, and P. Miloro. Directivity and frequency-dependent effective sensitive element size of membrane hydrophones: Theory vs. experiment. *IEEE Trans. Ultrason. Ferroelect. Freq. Contr.*, 2019.
- [15] IEC. Ultrasonics-hydrophones-part 3: Properties of hydrophones for ultrasonic fields up-to 40 MHz. *Standard IEC 62127-3*, 2013.
- [16] P. C. Beard, A. M. Hurrell, and T. N. Mills. Characterization of a polymer film optical fiber hydrophone for use in the range 1 to 20 MHz: A compar-

- ison with pvdF needle and membrane hydrophones. *IEEE Trans. Ultrason. Ferroelect. Freq. Contr.*, 47:256–264, 2000.
- [17] J. F. Krücker, A. Eisenberg, M. Krix, R. Lötsch, M. Pessel, and H. Trier. Rigid piston approximation for computing the transfer function and angular response of a fiber-optic hydrophone. *J. Acoust. Soc. Am.*, 107(4):1994–2003, 2000.
- [18] D. R. Bacon. Characteristics of a pvdF membrane hydrophone for use in the range 1-100 MHz. *IEEE Trans. Ultrason. Ferroelect. Freq. Contr.*, 29(1):18–25, 1982.
- [19] K. Nakamura. *Ultrasonic transducers: Materials and design for sensors, actuators and medical applications*. Elsevier, 2012.
- [20] V. Wilkens and W. Molkenstruck. Broadband pvdF membrane hydrophone for comparisons of hydrophone calibration methods up to 140 MHz. *IEEE Trans. Ultrason. Ferroelect. Freq. Contr.*, 54(9):1784–1791, 2007.
- [21] P. Garland, A. Bezanson, R. Adamson, and J. Brown. Experimental and finite element model directivity comparison between PZT and PMN-PT kerfless arrays. In *Ultrason.*, pages 365–368. IEEE, 2011.
- [22] R. Preston. *Output measurements for medical ultrasound*. Springer Science & Business Media, 2012.
- [23] A. Hurrell. Voltage to pressure conversion: are you getting phased’ by the problem? In *J. Phys. Conf. Ser.*, volume 1, page 57. IOP Publishing, 2004.
- [24] E. Martin and B. Treeby. Investigation of the repeatability and reproducibility of hydrophone measurements of medical ultrasound fields. *J. Acoust. Soc. Am.*, 145(3):1270–1282, 2019.
- [25] I. O. Wygant, N. S. Jamal, H. J. Lee, A. Nikoozadeh, Ö. Oralkan, M. Karaman, and B. T. Khuri-Yakub. An integrated circuit with transmit beamform-

- ing flip-chip bonded to a 2-d cmut array for 3-d ultrasound imaging. *IEEE Trans. Ultrason. Ferroelect. Freq. Contr.*, 56(10):2145–2156, 2009.
- [26] G. Gurun, P. Hasler, and F. L. Degertekin. Front-end receiver electronics for high-frequency monolithic cmut-on-cmos imaging arrays. *IEEE Trans. Ultrason. Ferroelect. Freq. Contr.*, 58(8):1658–1668, 2011.
- [27] J. Staudenraus and W. Eisenmenger. Fibre-optic probe hydrophone for ultrasonic and shock-wave measurements in water. *Ultrasonics*, 31(4):267–273, 1993.
- [28] E. Z. Zhang, J. Laufer, and P. Beard. Backward-mode multiwavelength photoacoustic scanner using a planar Fabry–Pérot polymer film ultrasound sensor for high-resolution three-dimensional imaging of biological tissues. *Appl. Optics*, 47(4):561–577, 2008.
- [29] M. Klann and C. Koch. Measurement of spatial cross sections of ultrasound pressure fields by optical scanning means. *IEEE Trans. Ultrason. Ferroelect. Freq. Contr.*, 52(9):1546–1554, 2005.
- [30] J. Buchmann. Private communication. 21/11/2016.
- [31] J. A. Guggenheim, E. Z. Zhang, and P. C. Beard. A method for measuring the directional response of ultrasound receivers in the range 0.3–80 MHz using a laser-generated ultrasound source. *IEEE Trans. Ultrason. Ferroelect. Freq. Contr.*, 64(12):1857–1863, 2017.
- [32] B. Fay, P. A. Lewin, G. Ludwig, G. M. Sessler, and G. Yang. The influence of spatial polarization distribution on spot poled pvdf membrane hydrophone performance. *Ultrasound. Med. bio.*, 18(6-7):625–635, 1992.
- [33] R. A. Smith and D. R. Bacon. A multiple-frequency hydrophone calibration technique. *J. Acoust. Soc. Am.*, 87(5):2231–2243, 1990.

- [34] R. Preston, D. Bacon, and R. Smith. Calibration of medical ultrasonic equipment-procedures and accuracy assessment. *IEEE Trans. Ultrason. Ferroelect. Freq. Contr.*, 35(2):110–121, 1988.
- [35] J. Chan, Z. Zheng, K. Bell, M. Le, P. H. Reza, and J. T. W. Yeow. Photoacoustic imaging with capacitive micromachined ultrasound transducers: Principles and developments. *Sensors*, 19(16):3617, 2019.
- [36] O. Oralkan, A. S. Ergun, J. A. Johnson, M. Karaman, U. Demirci, K. Kaviani, T. H. Lee, and B. T. Khuri-Yakub. Capacitive micromachined ultrasonic transducers: Next-generation arrays for acoustic imaging? *IEEE Trans. Ultrason. Ferroelect. Freq. Contr.*, 49(11):1596–1610, 2002.
- [37] O. Oralkan, B. Bayram, G. G. Yaralioglu, A. S. Ergun, M. Kupnik, D. T. Yeh, I. O. W., and B. T. Khuri-Yakub. Experimental characterization of collapse-mode cmut operation. *IEEE Trans. Ultrason. Ferroelect. Freq. Contr.*, 53(8):1513–1523, 2006.
- [38] S. Michau, P. Mauchamp, and R. Dufait. Piezocomposite 30 MHz linear array for medical imaging: design challenges and performances evaluation of a 128 elements array. In *2004 IEEE Ultrason.*, volume 2, pages 898–901. IEEE, 2004.
- [39] R. Zhang, W. Zhang, C. He, J. Song, L. Mu, J. Cui, Y. Zhang, and C. Xue. Design of capacitive micromachined ultrasonic transducer (cmut) linear array for underwater imaging. *Sensor Rev.*, 36(1):77–85, 2016.
- [40] J. Rebling, O. Warshavski, C. Meynier, and D. Razansky. Optoacoustic characterization of broadband directivity patterns of capacitive micromachined ultrasonic transducers. *J. Biomed. Opt.*, 22(4):041005, 2016.
- [41] F. V. Hunt. The analysis of transduction, and its historical background. *Electroacoustics (Harvard University Press, Cambridge, Mass., 1954)*, 45, 1982.
- [42] Butterfly Network Inc. Butterfly iq. Last visited on 20/09/2019.

- [43] D. M. Mills. Medical imaging with capacitive micromachined ultrasound transducer (cmut) arrays. In *2004 IEEE Ultrason.*, volume 1, pages 384–390. IEEE, 2004.
- [44] N. A. Hall, R. Guldiken, J. McLean, and F. L. Degertekin. Modeling and design of cmuts using higher order vibration modes [capacitive micromachined ultrasonic transducers]. In *2004 IEEE Ultrason.*, volume 1, pages 260–263. IEEE, 2004.
- [45] S. Zhou and J. Hossack. Reducing inter-element acoustic crosstalk in capacitive micromachined ultrasound transducers. *IEEE Trans. Ultrason. Ferroelect. Freq. Contr.*, 54(6), 2007.
- [46] X. Chen, J. and Cheng, C. Chen, P. Li, J. Liu, and Y. Cheng. A capacitive micromachined ultrasonic transducer array for minimally invasive medical diagnosis. *J. Microelectromech S.*, 17(3):599–610, 2008.
- [47] O. Warshavski, C. Meynier, N. Sénégon, P. Chatain, J. Rebling, D. Razansky, N. Felix, and A. Nguyen-Dinh. Experimental evaluation of cmut and pzt transducers in receive only mode for photoacoustic imaging. In *P. Soc. Photo-opt. Ins.*, volume 9708, page 970830. International Society for Optics and Photonics, 2016.
- [48] M. Vallet, F. Varray, J. Boutet, J. Dinten, G. Caliano, A. S. Savoia, and D. Vray. Quantitative comparison of pzt and cmut probes for photoacoustic imaging: Experimental validation. *Photoacoustics*, 8:48–58, 2017.
- [49] P. C. Beard, F. Perennes, and T. N. Mills. Transduction mechanisms of the Fabry–Pérot polymer film sensing concept for wideband ultrasound detection. *IEEE Trans. Ultrason. Ferroelect. Freq. Contr.*, 46(6):1575–1582, 1999.
- [50] V. Wilkens and C. Koch. Fiber-optic multilayer hydrophone for ultrasonic measurement. *Ultrasonics*, 37(1):45–49, Jan 1999.

- [51] W. Weise, V. Wilkens, and C. Koch. Frequency response of fiber-optic multi-layer hydrophones: experimental investigation and finite element simulation. *IEEE Trans. Ultrason. Ferroelect. Freq. Contr.*, 49(7):937–946, 2002.
- [52] O. V. Bessonova and V. Wilkens. Membrane hydrophone measurement and numerical simulation of hifu fields up to developed shock regimes. *IEEE Trans. Ultrason. Ferroelect. Freq. Contr.*, 60(2):290–300, 2013.
- [53] Samuel M Howard and Claudio I Zanelli. P1b-4 characterization of a hifu field at high intensity. In *2007 IEEE Ultrason.*, pages 1301–1304. IEEE, 2007.
- [54] J. Haller, K. Jenderka, G. Durando, and A. Shaw. A comparative evaluation of three hydrophones and a numerical model in high intensity focused ultrasound fields. *J. Acoust. Soc. Am.*, 131(2):1121–1130, 2012.
- [55] L. Brillouin. Diffusion de la lumière et des rayons x par un corps transparent homogène-influence de l’agitation thermique. In *Annales de physique*, volume 9, pages 88–122. EDP Sciences, 1922.
- [56] P. Morris, A. Hurrell, A. Shaw, E. Zhang, and P. Beard. A fabry–pérot fiber-optic ultrasonic hydrophone for the simultaneous measurement of temperature and acoustic pressure. *J. Acoust. Soc. Am.*, 125(6):3611–3622, 2009.
- [57] J. Buchmann, J. Guggenheim, E. Zhang, C. Scharfenorth, B. Spannekrebs, C. Villringer, and J. Laufer. Characterization and modeling of fabry–perot ultrasound sensors with hard dielectric mirrors for photoacoustic imaging. *Appl. Optics.*, 56(17):5039–5046, 2017.
- [58] E. Z. Zhang and P. C. Beard. Characteristics of optimized fibre-optic ultrasound receivers for minimally invasive photoacoustic detection. In *P. Soc. Photo-opt. Ins.*, volume 9323, page 932311. International Society for Optics and Photonics, 2015.

- [59] P. C. Beard and T. N. Mills. Extrinsic optical-fiber ultrasound sensor using a thin polymer film as a low-finesse Fabry–Pérot interferometer. *Appl. Optics*, 35(4):663–675, 1996.
- [60] V. Wilkens. Characterization of an optical multilayer hydrophone with constant frequency response in the range from 1 to 75 MHz. *J. Acoust. Soc. Am.*, 113(3):1431–1438, 2003.
- [61] P. C. Beard. Two-dimensional ultrasound receive array using an angle-tuned Fabry–Pérot polymer film sensor for transducer field characterization and transmission ultrasound imaging. *IEEE Trans. Ultrason. Ferroelect. Freq. Contr.*, 52(6):1002–1012, 2005.
- [62] V. Wilkens and C. Koch. Amplitude and phase calibration of hydrophones up to 70 MHz using broadband pulse excitation and an optical reference hydrophone. *J. Acoust. Soc. Am.*, 115(6):2892–2903, 2004.
- [63] A. Perot and C. Fabry. On the application of interference phenomena to the solution of various problems of spectroscopy and metrology. *The Astrophysical Journal*, 9:87, 1899.
- [64] C. Fabry and A. Perot. Theorie et applications d’une nouvelle methode de spectroscopie interferentielle. *Ann. Chim. Phys*, 16(7):115, 1899.
- [65] P. C. Beard. Optical fiber sensor for the detection of laser-generated ultrasound in arterial tissues. *Proc. SPIE.*, 2331:112–122, 1995.
- [66] P. Morris, A. Hurrell, A. Shaw, E. Zhang, and P. Beard. A Fabry-Perot fiber-optic ultrasonic hydrophone for the simultaneous measurement of temperature and acoustic pressure. *J. Acoust. Soc. Am.*, 125(6):3611–3622, jun 2009.
- [67] D. R. Ramasawmy, E. Martin, J. A. Guggenheim, E. Z. Zhang, P. C. Beard, B. E. Treeby, and B. T. Cox. Analysis of the directivity of glass-etalon fabry–pérot ultrasound sensors. *IEEE Trans. Ultrason. Ferroelect. Freq. Contr.*, 66(9):1504–1513, 2019.

- [68] B. T. Cox, E. Z. Zhang, J. G. Laufer, and P. C. Beard. Fabry Perot polymer film fibre-optic hydrophones and arrays for ultrasound field characterisation. *J. Phys.*, 1:32–37, jan 2004.
- [69] J. B. Fortin and T. M. Lu. *Chemical vapor deposition polymerization: the growth and properties of parylene thin films*. Springer Science & Business Media, 2003.
- [70] A. Acquafresca, E. Biagi, L. Masotti, and D. Menichelli. Toward virtual biopsy through an all fiber optic ultrasonic miniaturized transducer: a proposal. *IEEE Trans. Ultrason. Ferroelect. Freq. Contr.*, 50(10):1325–1335, 2003.
- [71] S. Ashkenazi, R. Witte, and M. O’Donnell. High frequency ultrasound imaging using fabry-perot optical etalon. In *Medical Imaging*, pages 289–297. International Society for Optics and Photonics, 2005.
- [72] D. M. Marques, J. A. Guggenheim, R. Ansari, E. Z. Zhang, P. C. Beard, and P. Munro. On the intuitive understanding of interrogating fabry-perot etalon with a focused beam. In *Photons Plus Ultrasound: Imaging and Sensing 2019*, volume 10878, page 108780Q. International Society for Optics and Photonics, 2019.
- [73] T. A. Pitts and J. F. Greenleaf. Three-dimensional optical measurement of instantaneous pressure. *J. Acoust. Soc. Am.*, 108(6):2873–2883, 2000.
- [74] A. K. Ghatak and K. Thyagarajan. *Optical Electronics*. Cambridge University Press, 1989.
- [75] G. B. Hocker. Fiber-optic sensing of pressure and temperature. *Appl. optics*, 18(9):1445–1448, 1979.
- [76] H. A. Macleod. *Thin-film optical filters*. CRC press, 2017.
- [77] A. H. Nayfeh. The general problem of elastic wave propagation in multilayered anisotropic media. *J. Acoust. Soc. Am.*, 89(4):1521–1531, 1991.

- [78] A. H. Nayfeh. *Wave propagation in layered anisotropic media: With application to composites*, volume 39. Elsevier, 1995.
- [79] J.L. Rose. *Ultrasonic guided waves in solid media*. Cambridge University Press, 2014.
- [80] L. Brekhovskikh and Oleg A Godin. *Acoustics of layered media I: Plane and quasi-plane waves*, volume 5. Springer Science & Business Media, 2012.
- [81] L.M. Brekhovskikh. *Waves in Layered Media*. SAcademic Press, 1960, 1960.
- [82] D. R. Ramasawmy, B. T. Cox, and B. E. Treeby. Elasticmatrix: A matlab toolbox for anisotropic elastic wave propagation in layered media. *SoftwareX*, 11:100397, 2020.
- [83] G. E. Backus. Long-wave elastic anisotropy produced by horizontal layering. *J. Geophys. Res.*, 67(11):4427–4440, 1962.
- [84] M. Lowe. Matrix techniques for modeling ultrasonic waves in multilayered media. *IEEE Trans. Ultrason. Ferroelect. Freq. Contr.*, 42(4):525–542, Jul 1995.
- [85] W. T Thomson. Transmission of elastic waves through a stratified solid medium. *J. Appl. Phys.*, 21(2):89–93, 1950.
- [86] L. P. Solie and B. A. Auld. Elastic waves in free anisotropic plates. *J. Acoust. Soc. Am.*, 54(1):50–65, 1973.
- [87] N. A. Haskell. The dispersion of surface waves on multilayered media. *B. Seismol. Soc. Am.*, 43(1):17–34, 1953.
- [88] L. Brekhovskikh. *Waves in layered media*, volume 16. Elsevier, 2012.
- [89] L. E. Malvern. *Introduction to the Mechanics of a Continuous Medium*. Prentice-Hall, Inc, 1969.
- [90] L. E. Alsop. The leaky-mode period equation a plane-wave approach. *B. Seismol. Soc. Am.*, 60(6):1989–1998, 1970.

- [91] M. J. S. Lowe. *Plate waves for the NDT of diffusion bonded titanium*. PhD thesis, University of London, 1992.
- [92] A. Demcenko and L. Mazeika. Calculation of Lamb waves dispersion curves in multi-layered planar structures. *Ultragarsas*, 3(3):15–17, 2002.
- [93] Wenhao Z. and J. L. Rose. Lamb wave generation and reception with time-delay periodic linear arrays: a BEM simulation and experimental study. *IEEE Trans. Ultrason. Ferroelect. Freq. Contr.*, 46(3):654–664, may 1999.
- [94] J. Fong, M. J. S. Lowe, D. Gridin, and R. V. Craster. Fast techniques for calculating dispersion relations of circumferential waves in annular structures. In *AIP Conf. Proc.*, volume 657, pages 213–220. AIP, 2003.
- [95] K. F. Graff. *Wave Motion in Elastic Solids*. Dover Books on Physics Series. Dover Publications, 1975.
- [96] L. Rayleigh. On Waves Propagated along the Plane Surface of an Elastic Solid. *P. Lond. Math. Soc.*, s1-17(1):4–11, nov 1885.
- [97] H. Lamb. On waves in an elastic plate. In *P. Roy. Soc. A-Math. Phy.*, volume 93, pages 114–128. The Royal Society, 1917.
- [98] R. Stoneley. Elastic Waves at the Surface of Separation of Two Solids. *P. Roy. Soc. A-Math. Phy.*, 106(738):416–428, oct 1924.
- [99] C. Willberg, S. Duczek, J.M. Vivar-Perez, and Z.A.B. Ahmad. Simulation methods for guided wave-based structural health monitoring: a review. *Appl. Mech. Rev.*, 67(1):010803, 2015.
- [100] H. Song and J. Popovics. Characterization of steel-concrete interface bonding conditions using attenuation characteristics of guided waves. *Cement. Concrete. Comp.*, 83:111–124, 2017.
- [101] M. Rucka, E. Wojtczak, and J. Lachowicz. Detection of debonding in adhesive joints using lamb wave propagation. In *MATEC. Web. Conf.*, volume 262, page 10012. EDP Sciences, 2019.

- [102] C. Hakoda and C. J. Lissenden. Using the partial wave method for mode-sorting of elastodynamic guided waves. In *AIP Conf. Proc.*, volume 2102, page 020014. AIP Publishing, 2019.
- [103] C. Hakoda and C. Lissenden. Using the partial wave method for wave structure calculation and the conceptual interpretation of elastodynamic guided waves. *Appl. Sci.*, 8(6):966, 2018.
- [104] M. Backus. Amplitude versus offset: a review. In *SEG Technical Program Expanded Abstracts 1987*, pages 359–364. Society of Exploration Geophysicists, 1987.
- [105] J. Chen, J. Guo, and E. Pan. Reflection and transmission of plane wave in multilayered nonlocal magneto-electro-elastic plates immersed in liquid. *Compos. Struct.*, 162:401–410, 2017.
- [106] G. Li, Y. Zheng, Y. Jiang, Z. Zhang, and Y. Cao. Guided wave elastography of layered soft tissues. *Acta. Biomater.*, 84:293–304, 2019.
- [107] S. Shoja, V. Berbyuk, and A. Boström. Investigating the application of guided wave propagation for ice detection on composite materials. In *In Proc. Int. Conf. Eng. Vib.*, pages 152–161, 2015.
- [108] B. Pavlakovic, M. Lowe, D. Alleyne, and P. Cawley. Disperse: a general purpose program for creating dispersion curves. In *Review of progress in quantitative nondestructive evaluation*, pages 185–192. Springer, 1997.
- [109] F. H. Quintanilla, M. Lowe, and R. V. Craster. Full 3d dispersion curve solutions for guided waves in generally anisotropic media. *J. Sound. Vib.*, 363:545–559, 2016.
- [110] F. H. Quintanilla, Z. Fan, M. Lowe, and R. V. Craster. Guided waves’ dispersion curves in anisotropic viscoelastic single-and multi-layered media. *P. Roy. Soc. A-Math. Phys.*, 471(2183):20150268, 2015.

- [111] F. H. Quintanilla, M. Lowe, and R. V. Craster. Modeling guided elastic waves in generally anisotropic media using a spectral collocation method. *J. Acoust. Soc. Am.*, 137(3):1180–1194, 2015.
- [112] A. T. Adamou and R. V. Craster. Spectral methods for modelling guided waves in elastic media. *J. Acoust. Soc. Am.*, 116(3):1524–1535, 2004.
- [113] J. L. Prego Borges. *Lamb: a simulation tool for air-coupled Lamb wave based ultrasonic NDE systems*. PhD thesis, Universitat Politècnica de Catalunya, 2010.
- [114] S. Mallick and L. N. Frazer. Computation of synthetic seismograms for stratified azimuthally anisotropic media. *J. Geophys. Res. - Sol. Ea.*, 95(B6):8513–8526, 1990.
- [115] B. E. Treeby and B. T Cox. k-wave: Matlab toolbox for the simulation and reconstruction of photoacoustic wave fields. *J. Biomed. Opt.*, 15(2):021314, 2010.
- [116] R. C. Payton. *Elastic wave propagation in transversely isotropic media*, volume 4. Springer Science & Business Media, 2012.
- [117] S. P. Kelly, G. Hayward, and T. E. Gómez Alvarez-Arenas. Characterization and assessment of an integrated matching layer for air-coupled ultrasonic applications. *IEEE Trans. Ultrason. Ferroelect. Freq. Contr.*, 51(10):1314–1323, 2004.
- [118] E. Lamkanfi, N. F. Declercq, W. Van Paepegem, and J. Degrieck. Finite element analysis of transmission of leaky rayleigh waves at the extremity of a fluid-loaded thick plate. *J. Appl. Phys.*, 101(11):114907, 2007.
- [119] R. Cobbold. *Foundations of biomedical ultrasound*. Oxford university press, 2006.

- [120] Ş. Sorohan, N. Constantin, M. Găvan, and V. Anghel. Extraction of dispersion curves for waves propagating in free complex waveguides by standard finite element codes. *Ultrasonics*, 51(4):503–515, 2011.
- [121] D. R. Ramasawmy, E. Martin, J. A. Guggenheim, B. T. Cox, and B. E. Treeby. Directivity of a planar hard-dielectric fabry-pérot optical ultrasound sensor. In *2017 IEEE Ultrason.*, pages 1–4. IEEE, 2017.
- [122] D. R. Ramasawmy, B. T. Cox, and B. E. Treeby. The influence of strain-optic coefficients on the transduction mechanism of planar glass etalon fabry-pérot ultrasound sensors. In *2019 IEEE Ultrason.*, pages 2523–2526. IEEE, 2019.
- [123] R.G. Munro. Elastic moduli data for polycrystalline oxide ceramics. Technical Report NISTIR6853, Natl. Inst. Stand. Techno., 2002.
- [124] N. F. Borrelli and R. A. Miller. Determination of the individual strain-optic coefficients of glass by an ultrasonic technique. *Appl. Optics*, 7(5):745–750, 1968.
- [125] R. Waxler, D. Horowitz, and A. Feldman. Optical and physical parameters of plexiglas 55 and lexan. *Appl. Optics*, 18(1):101–104, 1979.
- [126] M. K. Szczurowski, T. Martynkien, G. Statkiewicz-Barabach, L. Khan, D. J. Webb, C. Ye, J. Dulieu-Barton, and W. Urbanczyk. Measurements of stress-optic coefficient and young’s modulus in pmma fibers drawn under different conditions. In *P. Soc. Photo-Opt. Ins. IV. SPIE*, 2010.
- [127] D. G. Shombert, S. W. Smith, and G. R. Harris. Angular response of miniature ultrasonic hydrophones. *Med. Phys.*, 9(4):484–492, 1982.
- [128] G. D. Harris and D. G. Shombert. A pulsed near-field technique for measuring the directional characteristics of acoustic receivers. *IEEE Trans. Ultrason. Ferroelect. Freq. Contr.*, 32(6):802–808, 1985.
- [129] A. Conjusteau, S. A. Ermilov, R. Su, H. Brecht, M. P. Fronheiser, and A. A. Oraevsky. Measurement of the spectral directivity of optoacoustic

- and ultrasonic transducers with a laser ultrasonic source. *Rev. Sci. Instrum.*, 80(9):093708, 2009.
- [130] L. Freund. *Dynamic fracture mechanics*. Cambridge university press, 1998.
- [131] G.W. Farnell and E.L. Adler. Elastic wave propagation in thin layers. In W. P. Mason and R. N. Thurston, editors, *Physical Acoustics*, chapter 2, pages 35–127. Academic Press, 2012.
- [132] D. B. Bogy and S. M. Gracewski. On the plane wave reflection coefficient and nonspecular reflection of bounded beams for layered half spaces underwater. *J. Acoust. Soc. Am.*, 74(2):591–599, 1983.
- [133] S. Moten. Modeling of an ultrasonic transducer for cardiac imaging. Technical report, Tech. Rep. D&C 2010.049, Dynamics and Control Group, 2010.
- [134] C. Daraio and V. F. Nesterenko. Strongly nonlinear wave dynamics in a chain of polymer coated beads. *Phys. Rev. E.*, 73(2):026612, 2006.
- [135] F. Levassort, L. P. Tran-Huu-Hue, P. Marechal, E. Ringgaard, and M. Lethiecq. Characterisation of thin layers of parylene at high frequency using pzt thick film resonators. *J. Eur. Ceram. Soc.*, 25(12):2985–2989, 2005.
- [136] C. Fei, J. Ma, C. T. Chiu, J. A. Williams, W. Fong, Z. Chen, B. Zhu, R. Xiong, J. Shi, and T. K. Hsiai. Design of matching layers for high-frequency ultrasonic transducers. *Appl. Phys. Lett.*, 107(12):123505, 2015.
- [137] N. Jackson, F. Stam, J. O’Brien, L. Kailas, A. Mathewson, and C. O’Murchu. Crystallinity and mechanical effects from annealing parylene thin films. *Thin Solid Films*, 603:371–376, 2016.
- [138] B. Bholra, H. Song, H. Tazawa, and W. Steier. Polymer microresonator strain sensors. *IEEE Photonics Technology Letters*, 17(4):867–869, 2005.
- [139] Speciality Coating Systems. Parylene deposition process. <https://scscoatings.com/parylene-coatings/>

- parylene-expertise/parylene-deposition, 2019. [Online; accessed 30-November-2019].
- [140] K. Tan, H. Zhang, M. Wen, and Z. Du. Effects of the film thickness on the morphology, structure, and crystal orientation behavior of poly (chloro-p-xylylene) films. *J. Appl. Polym. Sci.*, 132(5), 2015.
- [141] J. Ortigoza-Diaz, K. Scholten, C. Larson, A. Cobo, T. Hudson, J. Yoo, A. Baldwin, A Weltman-Hirschberg, and E Meng. Techniques and considerations in the microfabrication of parylene c microelectromechanical systems. *Micromachines*, 9(9):422, 2018.
- [142] K. Raum. Microelastic imaging of bone. *IEEE Trans. Ultrason. Ferroelect. Freq. Contr.*, 55(7):1417–1431, 2008.
- [143] D. Rohrbach, S. Lakshmanan, F. Peyrin, M. Langer, A. Gerisch, Q. Grimal, P. Laugier, and K. Raum. Spatial distribution of tissue level properties in a human femoral cortical bone. *J. Biomech.*, 45(13):2264–2270, 2012.
- [144] A. Bertholds and R. Dandliker. Determination of the individual strain-optic coefficients in single-mode optical fibres. *J. Lightwave Technol.*, 6(1):17–20, 1988.
- [145] E. W. Weisstein. Tree. From MathWorld—A Wolfram Web Resource. Last visited on 11/8/2016.